UNIVERSITÉ DE SHERBROOKE
Faculté de génie
Département de génie mécanique

EXPÉRIENCES ET MODÉLISATION NUMÉRIQUE D'ÉCOULEMENTS ISOTHERMES DE COULIS DE GLACE

EXPERIMENTS AND NUMERICAL MODELLING OF ISOTHERMAL ICE SLURRY FLOWS

Thèse de doctorat
Spécialité: génie mécanique

Aurélien BORDET

Jury: Pr. Sébastien PONCET (director)
Pr. Nicolas GALANIS (co-director)
Dr. Michel POIRIER (co-director)
Dr. Laurence FOURNAISON (examiner)
Pr. Fellouah HACHIMI (examiner)
Pr. Michael KAUFFELD (examiner)

Sherbrooke (Québec) Canada

May 2018

RÉSUMÉ

Le projet actuel de doctorat comporte différents travaux dont l'objectif commun est d'apporter une meilleure compréhension de la dynamique des écoulements de coulis de glace dans un tube isotherme. Les recherches sont réparties selon deux axes : un volet expérimental et un volet numérique.

La partie expérimentale se concentre principalement sur l'analyse des régimes d'écoulement de coulis de glace (constitués initialement d'une solution de propylène glycol à 9.5% en masse) en fonction de trois paramètres d'opération : la concentration en glace, la vitesse débitante de l'écoulement et les pertes de charge. L'intérêt ici provient de la visualisation directe de l'écoulement à travers une portion transparente de la conduite, donnant une idée exacte des structures en écoulement à un certain débit et une certaine concentration en glace. Il en découle la possibilité d'étudier et de relier les régimes d'écoulement, ainsi que leur évolution, aux paramètres quantitatifs susmentionnés. De nouveaux régimes d'écoulement ont été identifiés et une classification originale a été établie. Par ailleurs, des pertes de charge ont aussi été recueillies pour des écoulements au travers de géométries plus complexes telles que des coudes et des jonctions en T.

La partie numérique est consacrée au développement d'un modèle numérique pour l'étude du comportement dynamique des écoulements de coulis de glace en conditions isothermes. L'équation de transport proposée par [Phillips *et al.*, 1992] pour modéliser les suspensions particulaires concentrées est utilisée comme base pour décrire l'évolution de la fraction volumique de particules au sein de l'écoulement. Deux nouveaux termes y sont introduits pour tenir compte de la dispersion turbulente et de la flottabilité des particules. En premier lieu, le modèle se montre apte à reproduire des données expérimentales extraites de la littérature, pour différents écoulements de suspensions particulaires, et il parvient à de meilleurs résultats que d'autres modélisations diphasiques plus complexes. De plus, l'équation de transport pour la fraction volumique de particules est numériquement analysée terme à terme afin de mettre en lumière chaque phénomène physique influant la répartition des particules au sein de l'écoulement.
La validation étant effectuée, le modèle est utilisé pour l'analyse d'écoulements de coulis de glace. Quatre modèles de turbulence ont été testés et comparés. Les résultats obtenus avec le modèle $k-\omega$ SST sont ensuite rapprochés de ceux du modèle analytique de [Kitanovski and Poredoš, 2002], pour différentes conditions en entrée d'écoulement. Le modèle actuel semble capable de reproduire certains aspects hydrodynamiques complexes : les écoulements secondaires, la couche limite en proche paroi, ou des régimes d'écoulements propres aux coulis de glace.

Mots-clés : coulis de glace, suspensions particulaires, modélisation numérique, mécanique des fluides expérimentale

ABSTRACT

The present PhD project gathers several works whose common goal is to give a better insight into the dynamics of ice slurry flows in a straight pipe under isothermal conditions. The research combines experiments and numerical modelling.

The experimental part focuses on the analysis of the ice slurry flow patterns, made from an initial solution of 9.5%-mass propylene glycol, in function of three operating parameters: ice concentration, flow velocity, pressure drop. The specificity remains in the fact that the flow is visualised through a transparent portion of the pipe, giving a precise idea of its pattern at certain flow velocity and ice fraction level, and thus yielding the possibility to study the flow patterns and to correlate them to the aforementioned quantitative parameters. New complex flow patterns appear through the experiments and an original classification is established. Besides, pressure drop data are also collected for more complex geometries such as elbows and T-junctions.

The numerical part aims at developing and assessing an advanced numerical model in order to investigate the dynamic behaviour of ice slurry flows under isothermal conditions. The transport equation proposed by [Phillips *et al.*, 1992] for solid suspension flows is used as a basis to describe the evolution of the particle volume fraction within the flow. For turbulent flows and buoyant particles, two original terms are introduced to account for the turbulent dispersion and sedimentation of the particles. The model first favourably compares to experimental data available in the literature for three types of solid suspensions. It provides more accurate predictions than more complex two-phase models. Moreover, the transport equation for the particle volume fraction has been numerically analysed term by term in order to exhibit each individual physical/numerical phenomenon influencing the particle distribution within the mixture flow.
The numerical model is then used confidently to investigate ice slurry flows. Four turbulence closures are compared in a numerical benchmark. For discussion, the results obtained by the SST $k-\omega$ model are also compared to the analytical model of [Kitanovski and Poredoš, 2002] for eight sets of inlet flow conditions (U_m,Φ_m). The present model is able to capture more complex flow features, especially the secondary flow, the near-wall boundary layers or some regimes specific to slurry flows.

Keywords: ice slurries, solid suspension flows, numerical modelling, experimental fluid mechanics

À Sherbrooke et à l'Estrie.
Québec, septembre 2014 à décembre 2017.

ACKNOWLEDGEMENTS

À Sébastien, mon directeur, qui m'aura accordé sa confiance tout au long de ce projet de recherche, ainsi qu'une grande disponibilité et un réel soutien sur la révision de mes écrits scientifiques. À Michel et Nicolas, mes co-directeurs, et à l'aide apportée à travers leurs précieux conseils. À Michel encore, pour m'avoir admis à de nombreuses reprises au sein de son laboratoire, CanmetÉNERGIE (Varennes), afin d'y mener les expériences.

À la chaire de recherche en efficacité énergétique (CRSNG), et à ses partenaires : Hydro-Québec, CanmetÉNERGIE et Rio Tinto Alcan, sans lesquels le projet n'aurait pu avoir lieu.

Aux Professeurs Hachimi Fellouah, Michael Kauffeld et au Docteur Laurence Fournaison, pour avoir gentiment accepté d'être membres du jury et ainsi évaluer mes travaux de recherche.

Au Québec et au québécois : la découverte d'une culture, de paysages, d'un style de vie, de l'hiver, du patin à glace. À la ville de Sherbrooke et son accueil. À Kayan, Antoine et Melly, qui m'ont intégré dans cette vie québécoise et sherbrookoise avec beaucoup de spontanéité et de gentillesse, et avec lesquels j'ai énormément partagé.

À la troupe des Mille Feux, vraie petite famille outre Atlantique.

Aux étudiants des équipes de recherche en efficacité énergétique et en aéroacoustique. Par ordre d'apparition : Sergio le vénézuelien, Prateek l'indien, Chaofan le chinois, Francis un autre matméca, Maud la parisienne, Ibai le basque, James l'écossais, Philippe le ch'ti, Sylvain le marseillais, Dipali la marathi, Miguel le portugais, Safouane le tunisien et Emmanuel le bourguignon. Bastien le cauchois et Régis l'alsacien, in extremis. Puisse le monde être un jour à l'image de ce groupe.

À Alice, colocataire et post-doctorante, fervent soutien et présence chaleureuse par beau temps comme par mauvais temps.

À Micha, compagnon de bureau, co-thésard, co-acteur, co-metteur en scène, partenaire de badminton, colocataire à ses heures, dont la présence m'aura accompagné et marqué durant plus de trois ans.

À Marlène, pour ses précieux coups de main en informatique, toujours très efficaces.

À Lisa, pour ses corrections de langue anglaise sur ce mémoire.

À mes parents et à ma sœur, phare lointain posé sur le roc, que rien ne perturbe.

TABLE OF CONTENTS

LIST OF FIGURES

LIST OF TABLES

LIST OF SYMBOLS

Latin letters

A	pipe cross-section area (m^2)
A_k	advection of turbulence kinetic energy $(m^2.s^{-3})$
a	particle radius (m)
C_0	Langevin-model constant $(-)$
C_D	drag coefficient $(-)$
Cf	friction factor $(-)$
C_i	ice concentration $(kg.kg^{-1})$
C_s	additive concentration $(kg.kg^{-1})$
D	pipe diameter (m)
D_k	term of ϕ-equation representing a shear diffusion with particle collision (s^{-1})
D_k^T	diffusion of k due to turbulent transport $(m^2.s^{-3})$
D_k^ν	diffusion of k due to molecular transport $(m^2.s^{-3})$
D_T	term of ϕ-equation representing turbulent dispersion (s^{-1})
D_μ	term of ϕ-equation representing a shear diffusion with viscosity variation (s^{-1})
d	particle diameter (m)
d_*	dimensionless particle diameter $(-)$
Fr	Froude number $(-)$
F_c	term of ϕ-equation representing convective flux (s^{-1})
F_b	term of ϕ-equation representing sedimentation (s^{-1})
F_{sl}	interfacial forces between solid and liquid faces (N)
f	damping function for particle settling $(-)$
g	gravitational acceleration $(9.81 m.s^{-2})$
He	Hedström number $(-)$
$\mathbf{I}$	identity matrix $(-)$
k	consistency coefficient $(Pa.s^n)$, turbulence kinetic energy $(m^2.s^{-2})$
L	pipe length (m)
m	Cross model constant $(-)$
$\dot{m}$	mass transfer rate between phases $(kg.s^{-1})$
N	diffusion terms in Philipps' equation $(kg.m^{-1}.s^{-1})$
n	flow index $(-)$
P_{atm}	atmospheric pressure (Pa)
P_k	production of turbulence kinetic energy $(m^2.s^{-3})$
p	local pressure (Pa)
p_s	solid pressure (Pa)
ΔP	pressure drop (Pa)
$\Delta P/L$	pressure drop per unit of length $(Pa.m^{-1})$
Q	volumetric flow rate $(m^3.s^{-1})$ or thermal flux $(W.m^{-2})$

Re	Reynolds number $(-)$
Re_c	critical Reynolds number after [Swamee and Aggarwal, 2011] $(-)$
Re_s	particle Reynolds number $(-)$
Re_t	transition Reynolds number $(-)$
(r, θ, z)	cylindrical coordinates (m or rad)
S	stratification parameter after [Darbouret, 2005] $(-)$
s	density ratio ρ_i/ρ_l $(-)$
T	temperature (K or $°C$)
T_L	Lagrangian integral time scale (s)
Tk	thickness of the rectangular channel cross-section (m)
U	mean flow velocity $(m.s^{-1})$
U_m	mean mixture velocity $(m.s^{-1})$
u	local streamwise velocity $(m.s^{-1})$
u^+	dimensionless velocity $(-)$
u^τ	shear velocity $(m.s^{-1})$
u'	fluctuating velocity $(m.s^{-1})$
$\overline{u'_i u'_j}$	Reynolds stress tensor components $(m^2.s^{-2})$
(x, y, z)	Cartesian coordinates (m)
x_i	ith spatial coordinate (m)
y^+	dimensionless wall distance $\sim r^+$ $(-)$

Greek letters

α	exponent in the [Richardson and Zaki, 1954]'s hindered function $(-)$
α_i	volume fraction of the ith phase $(m^3.m^{-3})$
Γ_T	particle turbulent diffusion $(m^2.s^{-1})$
$\dot{\gamma}$	shear rate (s^{-1})
$\dot{\gamma}_w$	wall shear rate (s^{-1})
δ	Kronecker symbol $(-)$
ϵ	local diffusion coefficient $(m^2.s^{-1})$, pressure loss coefficient $(-)$
ε or ε_k	turbulence kinetic energy dissipation $(m^2.s^{-3})$
θ	angular measure (rad)
θ_s	granular temperature $(m^2.s^{-2})$
λ	Cross model constant $(-)$
μ	dynamic viscosity $(Pa.s)$
μ_0	zero-shear viscosity $(Pa.s)$
μ_∞	infinite viscosity $(Pa.s)$
μ_B	Bingham viscosity $\sim \mu_\infty$ $(Pa.s)$
ν, ν_m	(molecular) kinematic viscosity $(m^2.s^{-1})$
ν_τ	turbulent viscosity $(m^2.s^{-1})$
ρ	density $(kg.m^{-3})$
σ_k	constant of the SST k-ω model $(-)$

τ	shear stress (Pa)
$\bar{\bar{\tau}}$	shear stress tensor (Pa)
τ_w	wall shear stress (Pa)
τ_0	yield stress stress (Pa)
Φ_m	mean inlet ice volume fraction $(m^3.m^{-3})$
ϕ	local ice volume fraction $(m^3.m^{-3})$
ω	specific rate of dissipation (s^{-1})
ω_s	hindered particle settling velocity $(m.s^{-1})$
ω_{s0}	terminal particle settling velocity $(m.s^{-1})$
ω_z	axial component of the vorticity (s^{-1})

Subscripts

i	ice, ith spatial component, phase index
is	ice slurry mixture
l	liquid phase
m	mixture, mean
r	relative
s	solid phase
w	wall

Abbreviations & acronyms

An	annular flow
CPU	central processing unit
D-Ho	degraded homogeneous flow
IPF	ice packing factor ($\sim \Phi_m$)
MPG	monopropylene glycol
P-Ho	pure homogeneous flow
RNG	re-normalisation group
RSM	Reynolds stress model
SST	shear stress transport
St	stratified flow

CHAPTER 1

INTRODUCTION

1.1 Industrial context

Over the last decades, a new class of refrigerant has progressively emerged: ice slurries. Briefly, they could be defined as all mixtures made of an aqueous solution and small ice particles (Figure 1.1). Despite the fact that similar objects were long known to save perishables, such as piled ice, industrial companies considered ice slurries only recently as a serious replacement solution to conventional single-phase refrigerants. Their very specific and rather complex properties grant them a high energy potential, but yield to numerous hydrodynamic issues as well.

However, ice slurries are already applied in various domains, such as industrial cooling, building cooling, food conditioning, surgery, fishing industry, etc. Several well documented reviews dedicated to ice slurry applications have already been released, see [Bellas and Tassou, 2005; Davies, 2005; Egolf and Kauffeld, 2005; Kauffeld *et al.*, 2010]. From these, the interested reader will find detailed information about the scientific and economical challenges at stake, the installations on which ice slurries can be integrated or the improvements they brought to refrigeration systems.

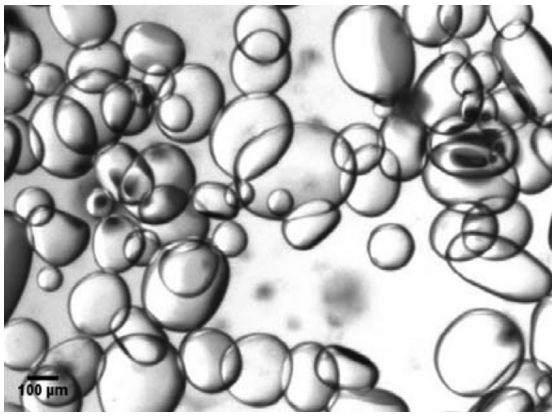

Figure 1.1 Microscopic photograph of an ice slurry made from $4wt.\%$-ethanol solution, with a mean ice particle diameter $d = 234.6\mu m$, after [Kawaji, 2012].

As a concrete example, ice slurries are currently used to cool buildings in Japan and Korea. In these countries, a pioneer program [Kauffeld *et al.*, 2010], as a test and reference case for future installations, was launched to enlarge the ice slurry cooling process to entire habitation areas: *a large-scale demonstration of district cooling.*

Two methods for building cooling were considered (Figure 1.2). For the building on the left, which illustrates the refitting of older installations, the ice slurry does not properly

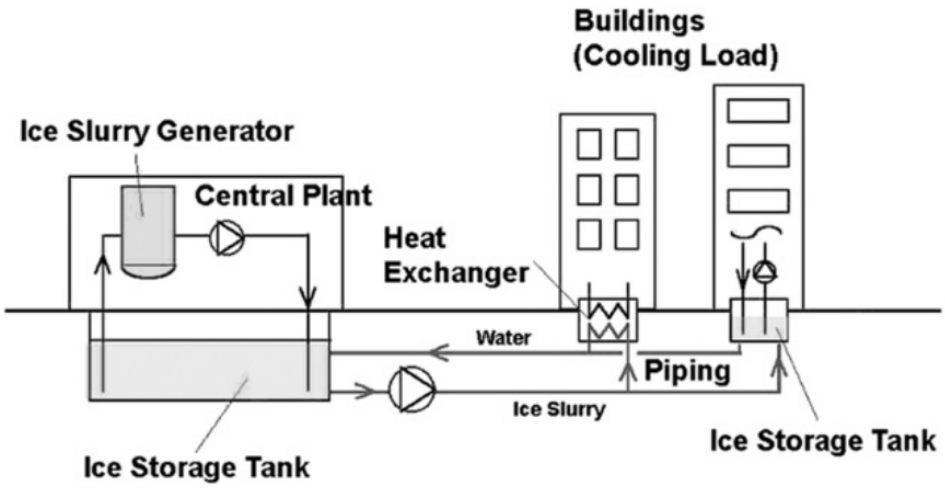

Figure 1.2 System involving ice slurries for the cooling of buildings, from the review of [Kauffeld *et al.*, 2010].

flow inside the building but cools it through an external heat exchanger that acts as an interface with the pre-existing cooling system installed within the building. For the building on the right, being a recent construction that fully incorporates ice slurries, a big tank located under the building is used as an ice slurry storage. A refrigeration loop is connected to the tank and allows the two-phase mixture to flow through the building, especially via its ventilation system, maintaining comfortable indoor temperatures. Both methods rely on a central plant that produces and stores ice slurry at large scales. Such an application is to yield major progresses ! Among which: an improved energy efficiency with large-scale cooling systems, cost reductions (for cooling installations and their operation) as well as a high potential for energy load shifting (since ice slurry is a very powerful means to store energy).

1.2 Ice slurries: a true replacement solution in refrigeration systems?

To explain the ability of ice slurries to replace conventional refrigerants in secondary refrigeration loop, one must refer to their physical nature. This type of complex fluids comprises a mixture of liquid water and ice particles, plus an additive (ethanol, glycol, propylene, etc.) that decreases the fusion temperature of water. At the same flow rates, a much bigger amount of heat can be extracted and transported than in the case of single-phase liquid water: this is due to the latent heat of fusion. [Egolf and Kauffeld,

2005] observed that "the heat capacity of ice slurries is eight times higher than the heat capacity of traditional single-phase secondary refrigerants". Thus, for a given amount of transported energy, much smaller equipment can be used compared to single-phase refrigeration systems. Moreover, using the latent heat permits to obtain a quasi-isothermal mixture flow, so that cooling may occur with little temperature change (increasing the cold quality). Finally, ice slurries contain a small quantity of non-polluting additives, which makes them an efficient refrigeration technology with low environmental impact.

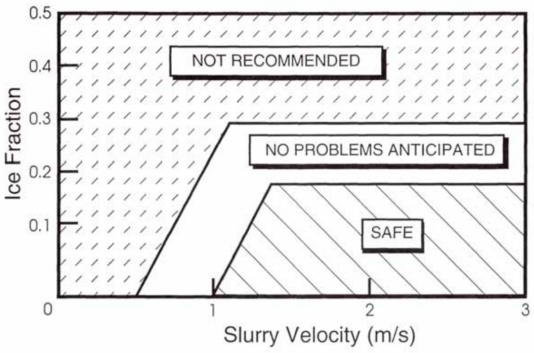

Figure 1.3 Recommended ice slurry transport conditions according to [Snoek, 1993].

Albeit, the two-phase character which makes ice slurries thermodynamically powerful, also increases its level of complexity from a hydrodynamic point of view − especially when the particle concentration becomes high: stratification issues, non-Newtonian effects or turbulence modulation are likely to appear. For instance, beyond a certain particle fraction level C_i, they may show a non-Newtonian behaviour. According to [Christensen and Kauffeld, 1997], this appears for $C_i > 15wt.\%$, to [Jensen *et al.*, 2001] for $C_i > 0.15wt.\%$ and to [Doetsch, 2001] for $C_i > 10wt.\%$. Despite some discrepancies between these last values, it implies in the case of a viscoplastic behaviour that a certain yield stress could be required to trigger the fluid motion, even at very low ice concentrations. Thus, depending on the ice fraction, the ice particle shape, the flow rate and the heat exchanger geometry, blockages are likely to occur or even, without reaching a blockage situation, pressure drops may become very large. [Snoek, 1993] established a stability diagram (Figure 1.3), coarsely showing the operating ranges of ice slurries in terms of flow velocity and ice concentration. Above a certain ice fraction level or below a certain flow rate, one can see that ice slurry use is not recommended. So far, the main argument to limit the *safe* transport remains the lack of scientific knowledge: notably the incapacity to correctly predict the hydrodynamic behaviour and the flowing structure of such solid-liquid flows. Unfortunately, this incapacity also slows down the design of any new reliable thermal system based on ice slurries.

Thus, a more rigorous and complete knowledge of ice slurry flows must be achieved. For this, a coupled approach − experimental/numerical − seems efficient, as the experimental

and the numerical tools complement well each other presently. The first one brings a direct insight of the flow structure from both direct visualizations and pressure data measurements, on which one may confidently rely (for model validations among others). If right modelling is assumed, the second one allows to capture the physical phenomena over precise inner locations that experiments could hardly provide, and to rapidly analyse these phenomena from numerous physical variables, that considerably reduces the research costs.

1.3 Experimental research

Ice slurries belong to the category of particulate suspensions. By their nature, they do not have a predefined aspect. According to the flow velocity, ice particle fraction and ice particle size, among other parameters, their macroscopic structure varies a lot and directly impacts the flow dynamics.

So far, direct observations of the flow patterns have been quite rare. Three to four main flow patterns are recurrently exhibited in horizontal straight pipe, but, most of the time, the usual classification seems too inaccurate. In addition, the transition mechanisms are still poorly understood. Yet in the general context of slurry flows, [Doron and Barnea, 1996] indicated that the pattern transitions are blurry and rather cover a range of flow rates. Furthermore, difficulties related to clear visualizations of ice slurry flows and their qualitative features remain large: [Kitanovski *et al.*, 2005] explicitly mentioned the great uncertainties when it comes to designate the flow pattern through transparent walls for dispersed flows. Albeit, the issue is crucial in order to quantify the ice stratification for instance, and then to anticipate possible blocking effects and drastic increase of the pumping power.

Moreover, the impact of the flow patterns and their transition processes on quantitative flow data is little known. The coupling of the flow patterns with the quantitative data would yield a smarter understanding of each. Even in simple cases, such as horizontal straight pipe flows, the flow data may then become a suitable indicator of the ice slurry flow state. Besides, few studies proceed of ice slurry flows through more technical or complex geometries (compared to the straight pipe), that would bring for them the usual flow data (ΔP, ϕ, u_i) or the flow patterns. This second point is important, since ice slurries are integrated into complex thermal systems, involving many singularities or fittings along them.

Thus, a closer look will be taken at two main features in chapter 3:
1. the accurate description of ice slurry flow patterns and the way they evolve in terms of flow velocity and ice concentration, with the outcome of a new pattern characterisation;
2. the direct correlations that may exist between the flow pattern variation and the principal flow data (pressure drop, friction factor, flow velocity or ice concentration) in a straight horizontal pipe under isothermal conditions. This is done for ice slurry flows made of a 9.5 $wt.\%-$mono-propylene glycol solution. Eventually, pressure drops are measured and discussed for flows crossing duct singularities (an ensemble of elbows and T-junctions).

1.4 Numerical research

Numerical developments are still required to obtain simple, accurate and reliable numerical models to describe the flow dynamics of ice slurries, even in simple geometries like straight pipes. [Phillips *et al.*, 1992]'s model has been chosen as a basis to describe the ice particle distribution within ice slurry flows since it was successfully applied to various suspension flows of small non-buoyant particles [Phillips *et al.*, 1992] and to ice slurry flows [Onokoko *et al.*, 2018]. Moreover, its simple formalism and its low calculation cost (compared to multiphase approaches) make such a model very practical. Some additional features must be integrated though.

In Chapter 4, [Phillips *et al.*, 1992]'s original model is extended to turbulent solid-liquid suspension flows with particle density different from that of the carrier fluid. For this, the model is combined to the SST $k-\omega$ turbulence model and a new term, derived from stochastic Lagrangian models, is added to [Phillips *et al.*, 1992]'s constitutive equation that accounts for the turbulent dispersion of the solid particles. Eventually, a second term is added to the equation in order to capture the particle stratification accurately. The whole modelling is validated against a set of experimental data from the literature for transitional and turbulent flows in horizontal straight pipes (see section 4.2).

Then, the different phenomena determining the particle distribution (over a pipe cross-section) and their transport still remain to be properly understood. This knowledge will notably permit to improve the modelling and to achieve efficient applications afterwards. The phenomena, *a priori* modelled by the different terms of the particle transport equation, vary remarkably from one to the other. They are due to velocity gradient variation, particle buoyancy or turbulent agitation − to quote some of them − which the mechanics is not obvious. In section 4.3, the transport equation of the particle volume fraction is analysed term by term; the experimental cases of [Kaushal *et al.*, 2005] are re-employed

as a simulation basis. These cases went over a large range of flowing conditions and thus provide numerous data for solid suspension flows (ice slurry flows being comprised in such kind of flows). From the experiments, several flow velocities U_m and particle concentrations Φ_m are numerically tested to exhibit the contribution of each model component, that is to say, each term of the particle volume fraction transport equation. Two particle diameters are considered, forming a third parameter of influence.

By analogy with solid suspension flows, the model can be extended to ice slurry flows, and used as an efficient tool to reproduce such flows and to unravel their hydrodynamic secrets. Thus, in chapter 5, the new validated model is applied to isothermal ice slurry flows in a horizontal straight pipe. With the help of the numerical simulations, it is attempted to give a deep insight into the dynamics of such flows for different operating conditions. Eight combinations of (U_m,Φ_m) are investigated. Four principal points are studied in detail: the turbulence, the ice concentration, the flow velocity and the pressure drops. The analytical model of [Kitanovski and Poredoš, 2002] is used to enrich the discussion.

The manuscript will end with a summary of the main results gained from the present work and some interesting perspectives concerning the experimental and numerical study of ice slurry flows (Chapter 6).

CHAPTER 2

STATE OF THE ART

This chapter reviews some relevant bibliographical elements which are closely related to the different parts of the research work that follows. The aim is to present the actual state of the ice slurry knowledge. *All presented studies considered slurry flows in horizontal straight pipes.*

First section (2.1) concerns the various flow patterns and their transition modes observed with ice slurries flowing in straight pipes. Generally, the pattern classification are derived from previous studies done with particulate suspension flows.
Second section (2.2) focuses on the different ways to model ice slurry viscosity. This is a crucial issue for solid suspension modelling since viscosity of such mixtures is a very complex variable (i.e. correlated to many elements, such as viscosity of the carrier, fluid, particle size and shape, volume fraction of particles, etc.). Two principal ways exist: 1. the one considering the mixture viscosity as strictly dependent on the local particle volume fraction and 2. the one considering ice slurries as a Non-Newtonian material.
Third section (2.3) is dedicated to comprehensive modelling approaches − where viscosity is no longer the only parameter modified by addition of the particles. These modellings are divided in two categories: 1. multiphase hydrodynamic models (Eulerian, mixture, etc.) and 2. analytical models specifically developed for ice slurries.

2.1 Flow patterns of ice slurries

2.1.1 Denomination of the flow regimes

The usual way to characterize flow patterns for slurry flows is very well described in [Brennen, 2005]. It comprises four principal categories displayed on Figure 2.1 hereafter. Some vocabulary variations and/or specifications exist between the different authors interested in the subject, see [Darby, 1986; Doron and Barnea, 1996; Turian and Yuan, 1977]. Nevertheless these authors never introduced major changes in the pattern description.

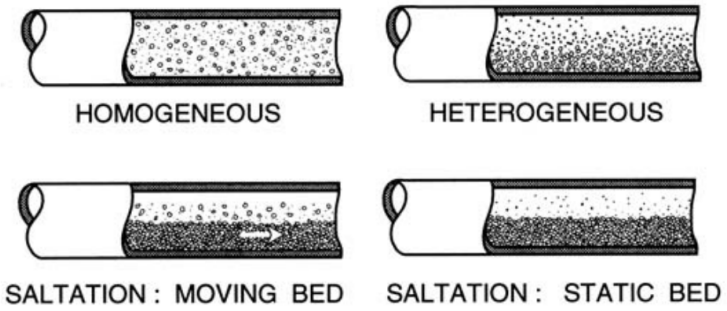

Figure 2.1 Flow regimes for slurry flows in a horizontal pipe exhibited by [Brennen, 2005] for particles heavier than the carrier fluid.

1. *Homogeneous*: the solid particles are distributed nearly uniformly across the pipe cross-section.
2. *Heterogeneous*: there is a concentration gradient in the direction perpendicular to the pipe axis, with more particles transported in the lower part of the pipe cross-section.
3. *Moving bed* (saltation): solid particles accumulate at the bottom of the pipe. Thus they form a packed bed layer, which moves along the pipe bottom. The concentration of this layer corresponds to maximal packing, or nearly so. The upper part of the pipe cross-section is occupied by a heterogeneous mixture.
4. *Static bed* (saltation): a stationary deposit is observed at the bottom of the pipe. On top of this deposit, particles are transported as a separate moving layer. The rest of the pipe is still occupied by a heterogeneous mixture, though its concentration profile is much steeper than in the other flow patterns.

This classification has been introduced by [Doron and Barnea, 1996], for particles heavier than the carrier fluid.

Such a characterization (originally made for all type of particulate suspensions or slurries) is re-employed in most of the research works on ice slurry flows, see [Kitanovski *et al.*, 2002; Reghem, 2002; Stutz *et al.*, 2001; Wang *et al.*, 2017]. For [Turian and Yuan, 1977], *saltation* only concerns *moving bed* contrarily to [Brennen, 2005; Darby, 1986]. *Moving bed* or *static bed* may also be classified as *stratified* by [Reghem, 2002] and *static bed* is rather named *stationary bed* by ice slurry searchers such as [Kitanovski *et al.*, 2002]. Finally, [Tian *et al.*, 2014] classified homogeneous and heterogeneous flows together into one single category: suspension flow.

Nevertheless, a couple of researchers introduced other categories for the flow pattern characterization of ice slurries:

• [Reghem, 2002] added a new pattern category to the previous description (without rad-

ically changing it). *Annular flow* occurs when the liquid-solid mixture forms a compact moving block that fills a large area of the pipe cross-section. The author specifies that a tiny water layer remains between the pipe wall and the iced block, since the wall friction makes the ice crystals melt at this location.

• Eventually, [Hirochi *et al.*, 2004] introduced their own characterization. According to their experimental observations, only three categories appear:

1. *Dispersed-particle flow*: ice particles do not coalesce, moving separately. This is equivalent to the homogeneous flow described in the previous classification.
2. *Cluster flow*: ice particles coalesce to form clusters and flow through a pipe, keeping their shapes not deformed.
3. *Column flow*: The clusters coalesce to form an axially continuous column. In the case of high fraction, this flow becomes a cylindrical rigid body filling the pipe. This may be equivalent to annular flow.

The real particularism of this last characterization is the absence of stratified flows (no stationary nor moving beds appeared through the experiments). Only column and cluster flows were observed at lower flow velocities. [Hirochi *et al.*, 2004]'s experiments were conducted with various size and shape of ice crystals.

2.1.2 Influencing flow parameters

The existence and transition of the flow patterns depend on various parameters (i.e. flow velocity, particle concentration, particle size, etc.) for which it is important to get a general idea.

Flow pattern maps

Such maps allow to show the transition from one pattern to another with the variation of the aforementioned flow parameters. They offer a significant insight into pattern behaviour.

I. Concerning slurry flows in general.

[Doron and Barnea, 1996] is a rich reference on the subject. From their three-layer model [Doron and Barnea, 1993], they could establish two kinds of map: i. in terms of both phase velocities U_s ($\Leftrightarrow U_{SS}$) and U_l ($\Leftrightarrow U_{LS}$) (Figure 2.2), and ii. in terms of mixture velocity U_m ($\Leftrightarrow U_S$) and volumetric solid concentration ϕ ($\Leftrightarrow C_S$). On each map, one sees the existence of the aforementioned patterns, with the addition of "blockage" denoting situations of stopped flow by excess of particles. Even for specific flow parameters, the maps exhibit relevant tendencies of slurry flow patterns that can be found in other research

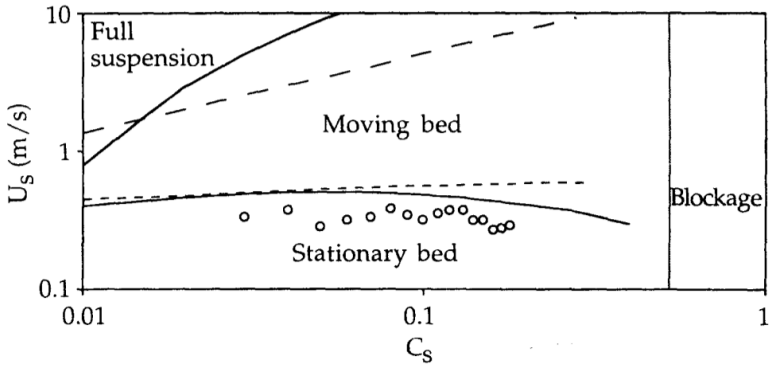

Figure 2.2 According to [Doron and Barnea, 1996]: mixture velocity U_S/delivered concentration C_S flow pattern map. Mixture of acetal particles and water for $\rho_s = 1240\ kg/m^3$, $D = 50$ mm, $d = 3$ mm. Full lines: results according to their three-layer model, dash lines: correlations from [Turian *et al.*, 1987; Turian and Yuan, 1977], points: experimental data from [Doron and Barnea, 1995].

studies [Kitanovski *et al.*, 2002; Reghem, 2002; Turian and Yuan, 1977]. Figure 2.2 shows that the emergence of a stationary bed is mainly conditioned by the mixture velocity whereas blockage situations only appear beyond a certain particle concentration level. Full suspension is reached for lower concentration levels and higher mixture velocities.

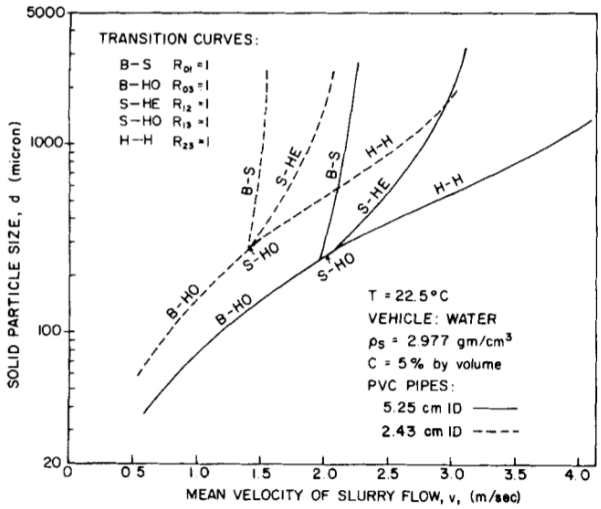

Figure 2.3 Pattern transitions for slurry flow plotted by [Turian and Yuan, 1977], for glass particles. B-HO: stationary bed to homogeneous, B-S: stationary to moving bed (saltation), S-HO: moving bed to homogeneous, S-HE: moving bed to heterogeneous, H-H: heterogeneous to homogeneous.

[Turian and Yuan, 1977] also provided several maps of interest as they exhibited the pattern evolution in terms of the solid particle size d and the mean flow velocity v_s (Figure 2.3). The authors developed a series of semi-empirical correlations from which they could draw

the transition curves. They also reported the effect of the pipe diameter on the flow transitions: the increase of the pipe section seems to delay the transitions towards higher velocities without really affecting it along the particle size axis. From other maps, the general pattern scheme seems unchanged: below a certain particle size, only moving bed and homogeneous flows exist. Moreover, transition from stationary to moving bed flows essentially depends on the velocity variation.

It is worth noticing that, in both maps (Figures 2.2 and 2.3), the pattern transition with the velocity increase seems to follow a precise order, that is to say: stationary → bed moving → heterogeneous → homogeneous.

II. Concerning ice slurries specifically.
Several maps have been compiled in [Kitanovski *et al.*, 2002] and expressed in terms of flow velocity U_m ($\Leftrightarrow$ v) and particle concentration Φ_m ($\Leftrightarrow$ C_v). It seems that only stratified flows (i.e. stationary or moving beds) remain at low velocity and that essentially an increase of flow velocity can yield a transition towards heterogeneous flow. This last remark may also be done for the map on Figure 2.4a elaborated from the theoretical model of [Kitanovski *et al.*, 2002], even if this last is said to "over predict the transition from the heterogeneous to homogeneous flow at larger ice-particle sizes". [Reghem, 2002]

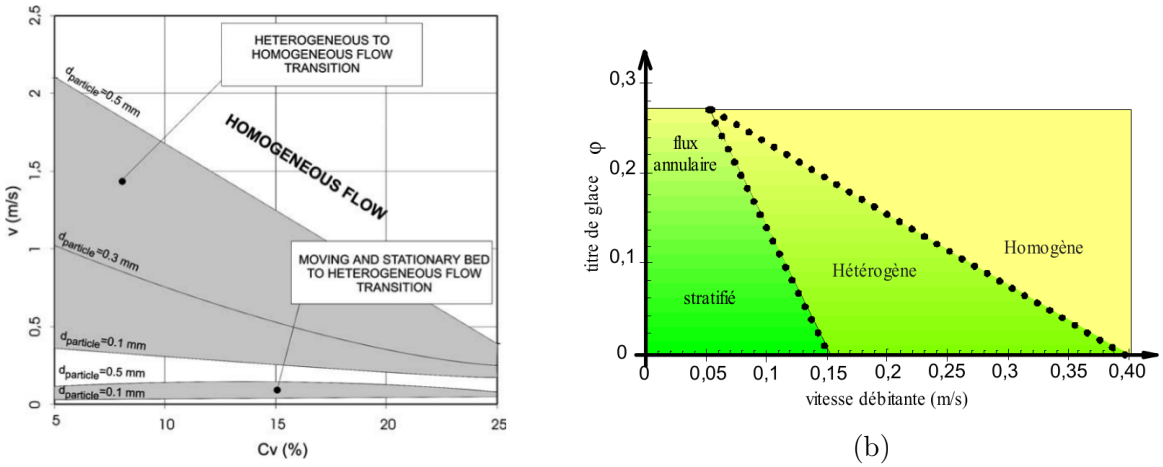

(a) (b)

Figure 2.4 (a) Pattern transitions for ice slurry flows plotted by [Kitanovski *et al.*, 2002], for a 10 wt.% water-ethanol solution and $D = 50$ mm. (b) Pattern map for ice slurry flows established by [Reghem, 2002], for a 10 wt.% water-ethanol solution and $D = 44.6$ mm. "titre de glace" $\Leftrightarrow$ ice volume fraction ϕ, "vitesse débitante" $\Leftrightarrow$ flow velocity U_m.

also built a synthetic map in terms of flow velocity and ice concentration, from various experimental data collection, where the annular flow ("flux annulaire") appears for low

flow velocities and high ice contents (Figure 2.4b). It then shows that beyond a certain ice concentration level ($\phi = 27\%$), the heterogeneous flow does not exist any more ; only annular and homogeneous flows coexist, so that the transition between them is directly done (as flow velocity varies).

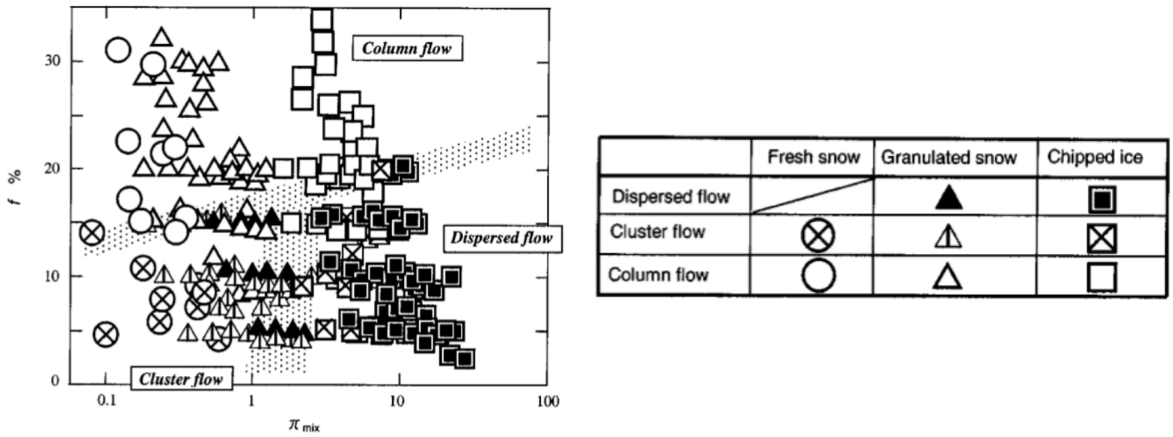

Figure 2.5 Pattern map for slurry flows established by [Hirochi *et al.*, 2004] for three particle types. Results obtained for a pipe diameter $D = 26 - 80$ mm, a particle diameter $d = 1 - 10$ mm, and flow velocity $U_m = 1 - 3\ m.s^{-1}$.

From their own classification, [Hirochi *et al.*, 2004] built an original pattern map (see Figure 2.5). This time, the flow patterns are expressed in terms of the ice volume fraction f and π_{mix}, the ratio between the agitating energy and the energy required to disperse the particles over the pipe cross-section. One remarks that beyond a certain ice concentration level ($\sim 15 - 20\ vol.\%$), only column flow seems to exist. Below, dispersed flow emerges for higher agitating energies (related to higher flow velocities), contrarily to cluster flow. This is similar to previous observations: a velocity increase yields an homogeneous flow.

Correlation between flow patterns and pressure drops

[Ayel *et al.*, 2003] quoted [Darby, 1986] who plotted pressure gradient $\Delta P/L$ as a function of the flow velocity V_m for slurry flows at a given particle concentration. On Figure 2.6a, the evolution of the flow patterns are also informed over several velocity ranges. Two main remarks can be formulated: (i) there is a pressure minimum at the transition between the saltation (stationary or moving bed, according to [Darby, 1986]'s definition) and the heterogeneous (V_{m1}) regimes; (ii) slurry pressure drop remains always higher than that of the carrier fluid for a certain mean solid content (see x_{s1}). [Turian and Yuan, 1977] have also shown the pressure drop evolution of a flowing slurry as a function of its velocity. The plot is quite similar (see Figure. 2.6b), albeit the pressure drop minimum occurs when transitioning from the stationary bed to the saltation (only moving bed, according to the

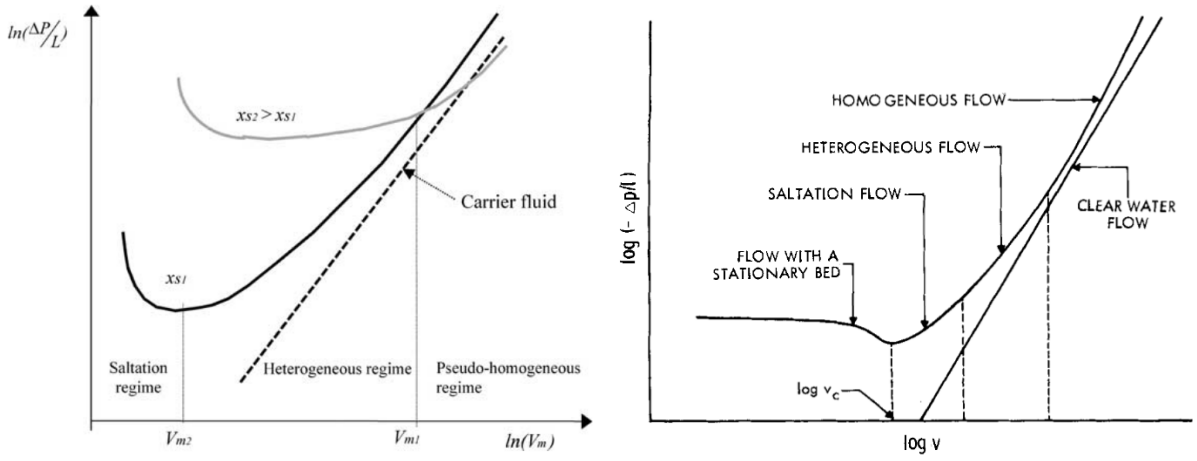

(a) (b)

Figure 2.6 (a) Pressure gradient as a function of the mean velocity for the various flow regimes, after [Darby, 1986]. (b) Pressure gradient $\Delta p/l$ as a function of the flow velocity v with the pattern evolution, after [Turian and Yuan, 1977].

present definition) flow regimes. However, [Turian and Yuan, 1977] remarked that "the boundaries between regimes are not well defined".

Finally, [Hirochi *et al.*, 2004] kept their own definitions, and plotted pressure drop/pattern evolution as a function of the flow velocity on Figure 2.7. Interestingly, no more pressure drop minimum shows up, it evolves smoothly with increasing velocity and with passing from one pattern to another.

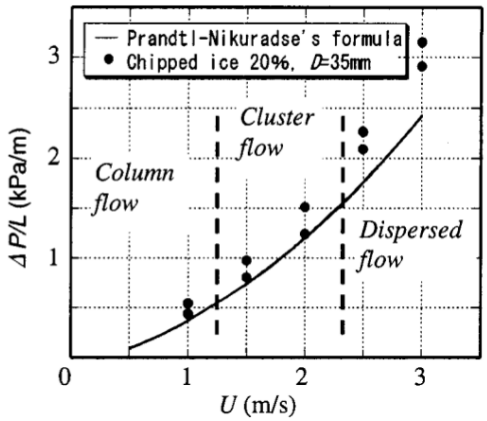

Figure 2.7 Pressure gradient $\Delta P/L$ as a function of the flow velocity U with the flow pattern, after [Hirochi *et al.*, 2004].

2.2 Viscosity modelling

2.2.1 Newtonian behaviour: viscosity expressions for solid suspensions

The viscosity of ice slurries may be characterized with the correlations usually applied to solid suspensions. This normally assumes spherical particles. Such a viscosity is generally superior to the one of the single liquid phase (μ_l). Several models have been designed to assess the apparent viscosity of suspensions when the flow is supposed homogeneous. However, most of them essentially are derived from the Einstein's equation recalled by [Barnes *et al.*, 1989b]:

$$\mu_m = \mu_l(1 + 2.5\phi) \tag{2.1}$$

Here, the mixture viscosity μ_m depends only on the viscosity of the liquid μ_l and the volume fraction of the solid phase ϕ in the mixture. This equation is defined for $\phi < 0.01$. It does not take into account the particle size, neither the effects of particle-particle interactions. Apparently, no restriction is given concerning the particle size, which may be questionable.

[Thomas, 1965] introduced another relation which takes the particle-particle interactions into consideration. The model is valid for $\phi < 0.625$, the maximum random packing factor for spherical particles, and particle sizes going from 0.1 μm to 435 μm:

$$\mu_m = \mu_l(1 + 2.5\phi + 10.05\phi^2 + 0.00273e^{16.6\phi}) \tag{2.2}$$

This model is probably still the most commonly used, see [Kitanovski and Poredoš, 2002; Onokoko *et al.*, 2018; Wang *et al.*, 2013b]. It gives a superior order of precision than the previous equation (2.1). However, [Hansen and Kauffeld, 2000] found that the correlation over predicts the viscosity of ice slurry for $\phi > 15\%$.

Other existing correlations for the viscosity of Newtonian slurries are reviewed in the works of [Kauffeld *et al.*, 2005; Kitanovski and Poredoš, 2002], allowing to have a larger scope. Albeit, these correlations do not seem to be used in the context of ice slurry. From a general perspective, the work of [Blazejewski, 2012] is of great interest. It brings a very good and complete review of the viscosity correlations for suspensions of rigid mono-sized spheres.

2.2.2 Non-Newtonian behaviour: rheological characterization

Above certain ice concentration levels, ice slurries are often considered as non-Newtonian materials. Three principal ways may be used to characterize their rheological behaviour: i. *pseudoplastic* (or shear-thinning), ii. dilatant (shear-thickening), and iii. *viscoplastic* (with a yield stress τ_0). These different behaviours, each of them time-independent, depend on several factors such as the ice packing factor ($\Leftrightarrow \phi$) or the additive type and concentration. It is next attempted to see how both of them approach ice slurry flow behaviour and in which contexts they can be used. [Kitanovski *et al.*, 2005; Monteiro and Bansal, 2010] gave a large insight into ice slurry rheology through two detailed reviews.

Pseudoplastic and dilatant behaviours

[Chhabra and Richardson, 2008] recalled that *pseudoplastic fluids* are characterized by an apparent viscosity which decreases with increasing shear rate and *dilatant fluids* are similar to pseudoplastic systems in that they show no yield stress but their apparent viscosity increases with increasing shear rate. Both of them can be described through the **Ostwald-de-Waele model** (or power-law model):

$$\tau = k(\dot{\gamma})^n, \qquad \begin{array}{l} n < 1 \Rightarrow \text{shear-thinning behaviour} \\ n > 1 \Rightarrow \text{shear-thickening behaviour} \end{array} \tag{2.3}$$

where τ is the shear stress (Pa), $\dot{\gamma}$ the shear rate (s^{-1}), n the flow index and k the power-law consistency coefficient ($Pa.s^n$). The value of k can be viewed as the value of the apparent viscosity at a shear rate equal to unity.

[Kumano *et al.*, 2010] showed in an experimental study that the rheological behaviour of ice slurries is rather shear-thinning (flow index $n < 1$). They considered ice slurry flows in several horizontal pipes of various diameters D. Data of pressure drop and pipe friction coefficient were collected for different ice concentrations. It appeared that, for each value of mean ice concentration Φ_m, done with an initial solution of 5 $wt.\%$ ethanol, the power-law index n represented by the slopes on Figure 2.8 was below 1. This index n is deduced from global pressure drop and mass flow rate measurements according to the Rabinowitsch's law (see in [Metzner and Reed, 1955; Rabinowitsch, 1929]):

$$n = \frac{d\left(ln\frac{D\Delta P}{4L}\right)}{d\left(ln\frac{8U}{D}\right)} \tag{2.4}$$

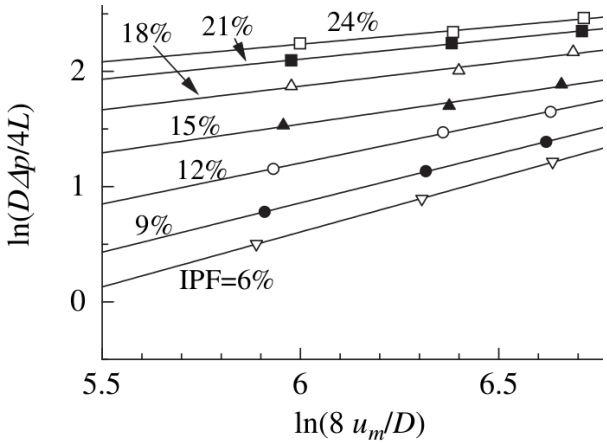

Figure 2.8 Relation between the shear stress at the pipe wall and the apparent shear rate for $D = 7.5\ mm$, after [Kumano *et al.*, 2010].

At first glance, the shear-thinning character of ice slurries is quite intuitive: the ice structures present in the fluid at rest tend to be destroyed or reduced when submitted to increasing constraints. The ductility of such material is thus augmented with increasing shear stress. Interestingly, their experiments exhibited a diminution of the flow index n with increasing mean ice concentration up to $\Phi_m = 25\ vol.\%$ (Figure 2.8). Otherwise, no clear rheological tendency showed up concerning the influence of pipe diameter ($D = 4.3$, 7.5, 10.2 mm).

[Mellari *et al.*, 2012] conducted a very similar study about the influence of the ice slurry initial composition – i.e. additive concentration C_s and ice mass fraction (IPF $\Leftrightarrow C_i$) – on its rheological behaviour. Their experimental cases considered isothermal flows of MPG (monopropylene-glycol)-based ice slurries through a straight horizontal pipe. Shear-thinning and -thickening behaviours appeared and the Ostwald-de-Waele rheological model was used. For all initial solute concentrations $C_s \leq 14\ wt.\%$, again the flow index n

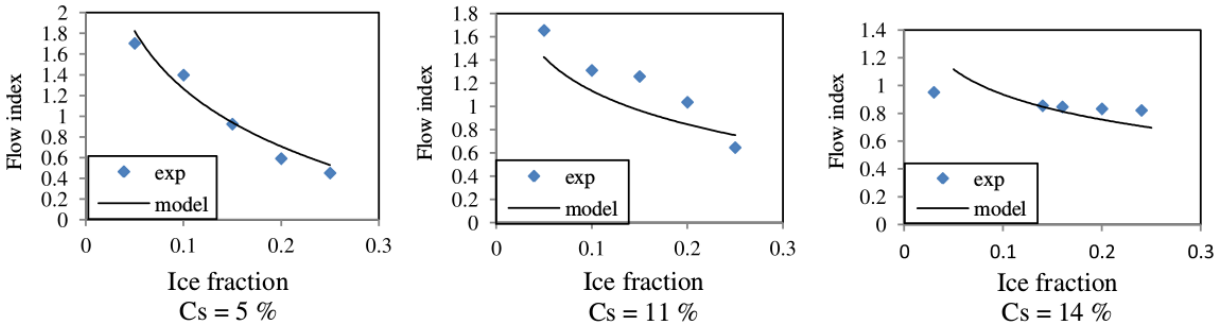

Figure 2.9 Variations of the flow index n obtained by experimental data and a rheological model, after [Mellari *et al.*, 2012] for a pipe diameter $D = 2.54$ cm.

diminishes with increasing C_i (Figure 2.9), and passing from shear-thickening to shear-thinning behaviour between $C_i = 10\%$ and 15% for $C_s = 5\%$ and 11%. For the highest assessed C_s ($= 24$ $wt.\%$), the fluid seems to only show a shear-thickening behaviour $n > 1$, whereas for $C_s = 14$ $wt.\%$, the contrary occurs: $n < 1$ at all C_i. Surprisingly, for $C_i > 10$ $wt.\%$, the flow index n increases with the ice concentration. This observation seems in contradiction with the previous ones. An explanation would be the influence of the solute concentration on the particle size: as it augments, the particle size d diminishes, especially at 24 $wt.\%$. This diminution of d would modify colloidal inter-particle forces, bringing a shear-thickening behaviour at high ice concentrations.
Eventually, the authors explicitly established two relationships linking k and n with both ice and initial solute mass concentrations, respectively C_i and C_s:

$$\begin{aligned} n(C_i, C_s) &= ln\left(C_i^{(6.881C_s - 1.174)} \cdot C_s^{1.062}\right) + 2.519 \\ k(C_i, C_s) &= 2.10^{-6} e^{\left\{39.32C_s + \left(6.85C_s^{-0.65}\right)\cdot C_i\right\}} \end{aligned} \tag{2.5}$$

From rheological measurements, [Stokes *et al.*, 2005] assessed the **Cross model** (Equation 2.6) for ice slurries made from a sucrose solution and showed that it can be applied to such suspensions. Measurements were conducted in a rheometer, not in a pipe. Initial additive mass fraction varied from 52% to 66.3%, which is very elevated compared to the usual values, the ice volume fraction varied from 0% to 30% (in each case, the temperature was maintained at $T = -18°C$), and the particle diameter was fixed to $d = 100$ μm. For this model, the apparent viscosity of the mixture (stress dependent) is expressed as follows:

$$\mu_m = \mu_\infty + \frac{\mu_0 - \mu_\infty}{1 + (\lambda\dot{\gamma})^m} \tag{2.6}$$

where μ_∞ is the infinite shear viscosity (viscosity at high shear rate) and μ_0 the zero-shear viscosity (viscosity with no shear). λ and m are two model constants that depend on the fluid mixture (on ϕ basically).

At low shear stress, the Cross model appeared very efficient to reproduce the rheological behaviour (finite viscosity) and the transition towards higher shear stress. Then, the Herschel-Bulkley model tended to be more accurate, although the Cross model remained close to the experimental data. In this experimental work, the authors clearly exhibited the shear-thinning character of the ice slurries they used. Moreover, very high μ_0 values were found (> 10000 $Pa.s$).

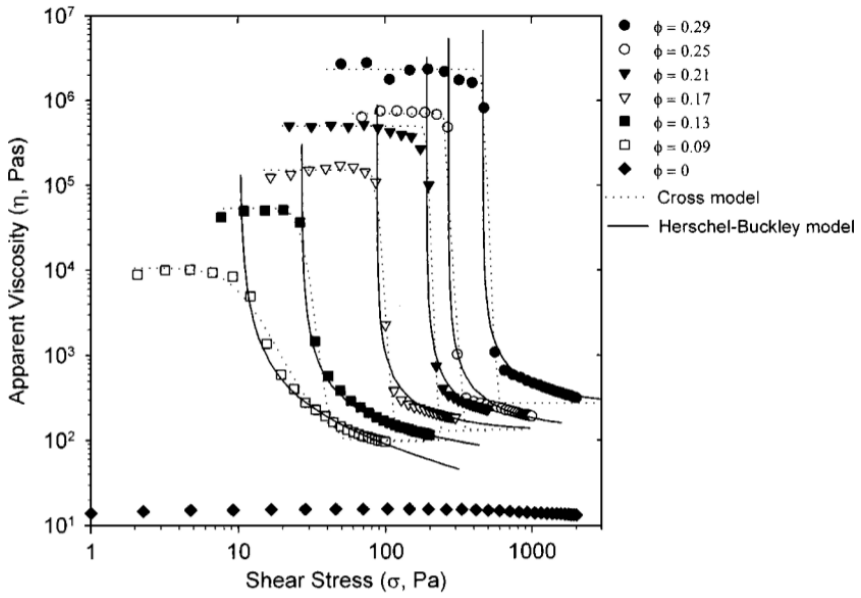

Figure 2.10 Mixture apparent viscosity η ($\sim \mu$) as a function of the shear stress σ ($\sim \tau$). Rheological measurements (points) of variously concentrated ice slurries according to [Stokes *et al.*, 2005]'s experiments. Comparison with the Cross and Herschel-Bulkley models (curves).

However, pseudoplastic or dilatant models do not account for any yield stress. This is essential to model solid structures forming in ice slurry flows, especially when ice concentration reaches high levels and the flow velocity is low.

Viscoplastic behaviours

The three next models − i.e. Bingham, Herschel-Bulkley and Casson − are designed for fluids with a viscoplastic behaviour. Such fluids are characterized by the existence of a yield stress (τ_0) which must be exceeded so that the fluid can deform or flow. By their structure, ice slurries are often included in this kind of complex fluid behaviour. Mainly, it is remarkable when the ice particles have a dendritic shape and then form stable or solid structures at very low shear rates. This is also the principal cause of pipe blocking: the rearrangement of the ice particles at low velocities, due to melting and re-freezing effects, creates rigid blocks of non-negligible size. The apparent viscosity is effectively infinite at the instant immediately before the substance yields and begins to flow.

[Ayel *et al.*, 2003] remarked that the models presented hereafter could be satisfactory on a restricted range of shear rates but completely inappropriate on a wider range. The

Bingham fluid model follows the next equation:

$$\tau = \tau_0 + \mu_\infty \dot{\gamma}, \quad \text{with} \quad \dot{\gamma} = 0 \quad \text{when} \quad |\tau| < |\tau_0| \tag{2.7}$$

Often, the two model parameters, τ_0 and μ_∞, are treated as curve fitting constants irrespective of whether or not the fluid possesses a real yield stress. This model has been used by [Egolf *et al.*, 2005] and [Niezgoda-Żelasko, 2006] for non-isothermal ice slurries in a heated duct. Otherwise, it seems quite rare that the *pure* Bingham model is used for ice slurry flow modelling.

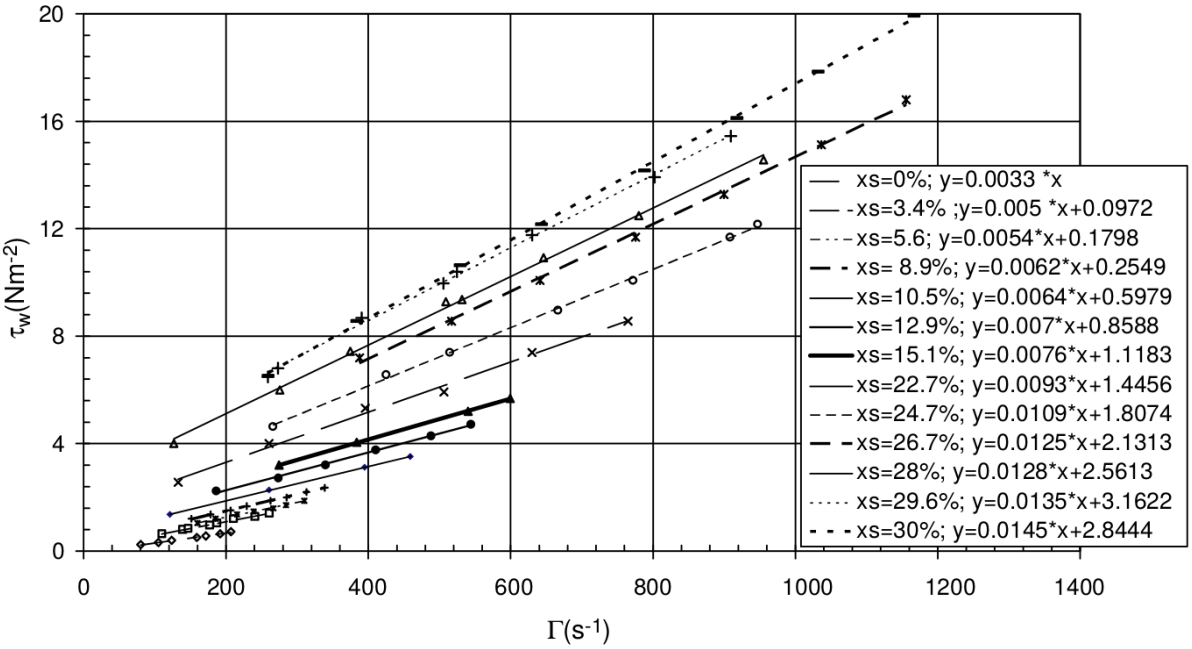

Figure 2.11 Rheograms for a pipe diameter $D = 0.016$ m [Niezgoda-Żelasko and Zalewski, 2006a]. Note that xs presently corresponds to the ice fraction and $\Gamma \Leftrightarrow \dot{\gamma}_w$.

[Niezgoda-Żelasko and Zalewski, 2006a] showed that the single-phase Bingham model makes thermal and flow phenomena modelling easier from a numerical point of view by reducing the calculation costs. Beside, the condition of gathering reliable data to get τ_0 and μ_∞ is required. These last parameters depend on the size and shape of the solid particles as well as the geometry of the resulting structures. Eventually, they justified the use of the Bingham rheological model by demonstrating that their experimental results (Figure 2.11) fit the equation (2.7) with the studied refrigerant (being ethyl alcohol) and for combinations of τ_0 and μ_∞ depending on the mean ice concentration (noted xs). Otherwise, [Ayel *et al.*, 2003] noticed that the Bingham model can lead to an inaccurate

estimation of the yield stress if not properly used, whereas the Herschel-Bulkley model can tackle this issue with its non-linear structure.

A simple generalization of the Bingham plastic model to embrace the non-linear flow curve (for $|\tau| > |\tau_0|$) is the three constant **Herschel-Bulkley fluid model** given by:

$$\tau = \tau_0 + k\dot{\gamma}^n, \quad \text{with} \quad \dot{\gamma} = 0 \quad \text{when} \quad |\tau| < |\tau_0| \tag{2.8}$$

The physical meaning of k and n (< 1) in equation (2.8) is similar to that in equation (2.3).

[Niezgoda-Želasko and Zalewski, 2006b] proposed to focus on this type of model in order to determine the relevance of the single-phase model (considering a Bingham fluid) against two multi-phase ones (Mixture and Eulerian models). The stress-strain tensor τ is defined for plastic-viscous fluid of *Herschel-Bulkley* type for $\tau > \tau_0$. However, the authors took the consistency coefficient $k = \mu_\infty$ and the flow index $n = 1$ which remains to consider the simple Bingham model. When $\tau > \tau_0$, the liquid behaves like a very viscous fluid with a viscosity μ_0. Eventually, their formulation led to an overestimation of the pressure drops as compared to experimental results, the relative difference did not exceed 16% though.

Recently, [Trabelsi *et al.*, 2017] characterized the rheological behavior of ice slurries composed of ethylene- and propylene-glycol at three initial concentrations 5, 14 and 24 *vol.*% using a hybrid rheometer. For ice fractions between 5 and 65%, they proposed different Herschel–Bulkley models, one for each additive concentration and type. The yield stress was found to remain very low whatever the operating conditions. Their experimental results were validated against an Artificial Neural Network model.

[Mika, 2012] focused on pressure drops for isothermal laminar flows through sudden contractions and expansions. A modified Herschel-Buckley rheological model is introduced to account for low and high shear rate regions as follows:

- *yield stress, behaviour close to the Bingham model for low shear rates*:

$$\tau_w = \tau_0 + k^{1/n}\dot{\gamma}_w \tag{2.9}$$

- *power law with a shear-thickening behaviour for high shear rates*:

$$\tau_w = k\dot{\gamma}_w^n \tag{2.10}$$

where τ_w and $\dot{\gamma}_w$ correspond respectively to the shear stress and the shear rate at the wall. With generalised correlations for the yield stress τ_0, flow index n and consistency coefficient k in the Hershel-Bulkley model, it is possible to determine the correlation $\dot{\gamma}_{crit}$ as a function of d, D and C_i to describe the critical shear rate for which the flow behaviour switches from a Bingham to a power law fluid (Figure 2.12).

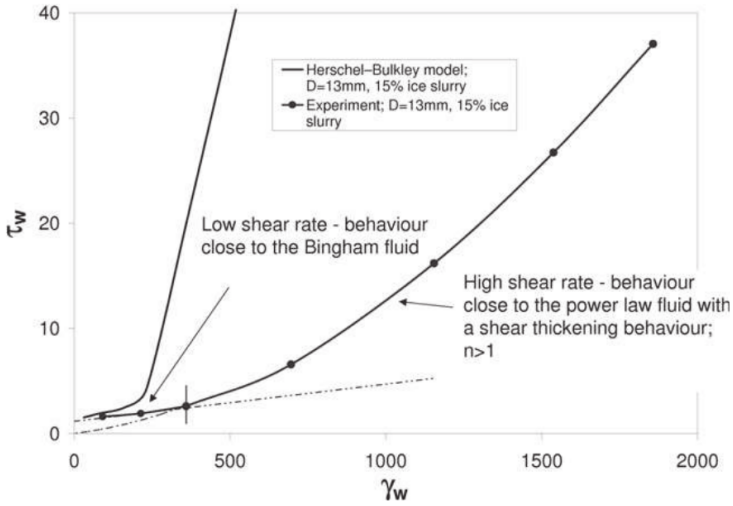

Figure 2.12 Rheograms after [Mika, 2012].

Eventually, the **Casson fluid model** is another variant of the models seen previously, expressed as follows:

$$(|\tau|)^{1/2} = (|\tau_0|)^{1/2} + (\mu|\dot{\gamma}|)^{1/2}, \quad \text{with} \quad \dot{\gamma} = 0 \quad \text{when} \quad |\tau| < |\tau_0| \tag{2.11}$$

However, this model is not much employed when it comes to take it as a basis for pressure drop or heat transfer studies. It is presented very briefly in the review of [Kitanovski *et al.*, 2005], and more in details in the comparative analysis focusing on pressure drops done by [Monteiro and Bansal, 2010]. Figure 2.13 shows the pressure drops as a function of the velocity given by several rheological models for ice slurry flows through a horizontal pipe.

In both cases, the Casson model overestimates the experimental data up to a threshold limit − see the slope rupture on Figure 2.13− from which it becomes in very good conformity with the experiments. The sudden *fall/rise* with the Casson curve is due to the influence of the critical Reynolds number, marking the beginning of turbulent flow according to the model. Originally, [Doetsch, 2002] applied the Casson model to ice slurry flows and developed a friction factor correlation from this model. It gave highly accurate results in terms of pressure drops for turbulent ice slurry flows. Albeit, [Kitanovski

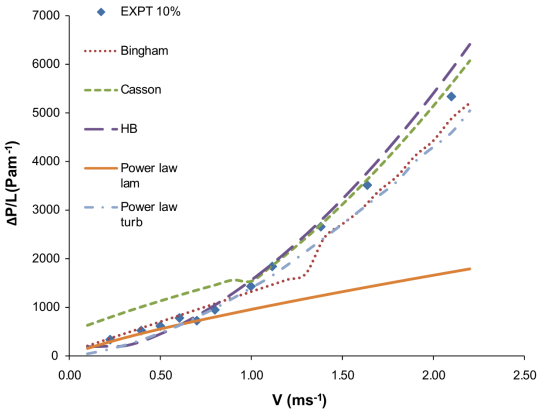

(a) Volume ice fraction $C_{I,vol} = 10$ %.

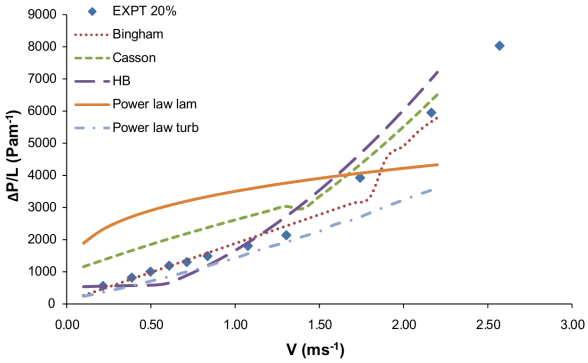

(b) Volume ice fraction $C_{I,vol} = 20$ %.

Figure 2.13 Experimental data from [Grozdek *et al.*, 2009] for a pipe diameter $D = 15$ mm and a particle diameter $d = 0.1$ mm.

et al., 2005] remarked that [Doetsch, 2002]'s modelling is limited to ice particle size such as $0.1 < d < 0.5$ mm and to isothermal homogeneous flows.

So far, the modelling quality has relied on a good knowledge of the experimental investigation domain, where one may accurately determine the rheological parameters according to the model used. Moreover, beyond 20 $wt.\%$ of ice concentration − highly favourable condition to the emergence of moving beds in pipe flows −, the use of a single-phase flow rheological model could appear inappropriate. In fact, the rheological approach alone does not allow to represent ice concentration variation within the mixture flow and, thus, would only assume homogeneous flows to work well. The positive aspect remains the relative simplicity of the calculation method leading to low computational costs, compared to two-phase flow modelling.

2.3 Comprehensive modelling approaches

Ice slurry flow modelling cannot be limited to viscosity modelling, since such flows are rarely homogeneous. This is the reason why more comprehensive modelling strategies must be employed. Two main classes are to be distinguished among the next models: multiphase and analytical. In both types, the inhomogeneous character of ice slurry flows is taken into account. Nevertheless, the previous viscosity models remain often used to predict the local viscosity.

Multiphase approaches, instead of considering the flow as a whole, decompose the system and focus on each phase's dynamics (solid and liquid) and their interactions to solve the dynamics of the ensemble. This method appears more rigorous, but it also costs much

more numerically.
Finally, the analytical models are based on slurry flow observations, notably the pattern observation. Heterogeneous flows concern a majority of ice slurry flows, which would require a specific modelling [Kitanovski and Poredoš, 2002]. Furthermore, ice slurry flows can be stratified, when they exhibit several "flowing layers" in certain flow conditions. Most of the time, two layers are considered, as with moving bed flows (a compact structure on the top and a free flow on the bottom of the pipe cross-section), but three layers are noticed as well (for instance: moving bed + heterogeneous + free flow, on the same pipe cross-section). Thus, two- [Stutz *et al.*, 2001] and three-layer [Doron and Barnea, 1993] models were developed to account for the stratification phenomena in order to describe slurry flow dynamics − pressure drop notably.

2.3.1 Multiphase flow modelling

The Eulerian model is a very complex multiphase model. It solves a set of n momentum and continuity equations for each phase. Coupling is achieved through the pressure and interphase exchange coefficients, which depends on the mixture type being modelled; granular (fluid-solid) flows are handled differently than non-granular (fluid-fluid) flows. For granular flows, the properties can be obtained from the application of the kinetic theory [Wang *et al.*, 2013a; Zhang and Shi, 2015]. Momentum exchange between the phases also varies according to the mixture type being modelled. The Eulerian multiphase model remains adapted for bubble columns, risers, particle suspensions − ice slurries for example − and fluidized beds.

This model allows to easily determine the physical properties of an entire medium since it is only required to supply the properties of the liquid carrier and the density and geometrical dimension of the "spherical" particles, which remains a great advantage over the mixture model described later on. It has been applied by [Niezgoda-Želasko and Zalewski, 2006b] in the context of ice slurry flows.

Here is the continuity equation for each phase:

$$\frac{\partial}{\partial t}(\alpha_i \rho_i) + \nabla \cdot (\alpha_i \rho_i \vec{u}_i) = \dot{m}_{qi} \tag{2.12}$$

where α is the volume fraction and the subscript i denotes liquid or solid phases. When $i = l$ or s, the subscripts q denotes the opposite phase. $\dot{m}_{qi}$ represents the mass transfer rate between the liquid and solid phases caused by the melting of the ice particles in the case of non-adiabatic flows.

The momentum balance for the liquid phase is formulated as:

$$\frac{\partial}{\partial t}(\alpha_l \rho_l \vec{u}_l) + \nabla \cdot (\alpha_l \rho_l \vec{u}_l \vec{u}_l) = -\alpha_l \nabla p + \nabla \cdot \bar{\bar{\tau}}_l + \alpha_l \rho_l \mathbf{g} + \mathbf{F}_{sl} + (\dot{m}_{sl}\vec{u}_s - \dot{m}_{ls}\vec{u}_l) \tag{2.13}$$

where $(\dot{m}_{sl}\vec{u}_s - \dot{m}_{ls}\vec{u}_l)$ represents the interphase momentum transfer caused by mass transfer and $\mathbf{F}_{sl}$ is the sum of the interfacial forces, that always includes the drag force $\mathbf{F_{D,l}}$ and some others (lift force, virtual mass force, turbulent dispersion force, etc.).

For the solid phase, the previous equation remains unchanged. Nevertheless, if the granular kinetic theory is adopted, a new term is added: $-\nabla p_s$ and the expression of the solid phase stress is written as follows:

$$\bar{\bar{\tau}}_s = \zeta_s \left(\nabla \vec{u}_s\right) \mathbf{I} + \alpha_s \mu_s \left[\nabla \vec{u}_s + \left(\nabla \vec{u}_s\right)^T - \frac{2\left(\nabla \vec{u}_s\right)\mathbf{I}}{3}\right] \tag{2.14}$$

where ζ_s is the bulk viscosity accounting for the resistance of the solid particles to compression and expansion [Lun *et al.*, 1984] and μ_s is the shear viscosity of the solid particles which is essentially decomposed into two terms: the collisional viscosity $\mu_{s,col}$ suited to any model and to which it is possible to add the kinetic viscosity $\mu_{s,kin}$ [Gidaspow, 1994; Syamlal and O'Brien, 1989]. Otherwise, p_s denotes the solid pressure derived by kinetic theory of granular flow. This theory [Gidaspow, 1994] states that the solid particle motion arising from particle-particle collisions is assumed as the thermal motion of gas molecules, taking the inelasticity of the granular phase into account.

Concerning the interphase forces, the drag force $\mathbf{F_{D,l}}$ is the one playing a leading role in the momentum exchange between solid and liquid phases. Therefore, only this interphase force is presented:

$$\mathbf{F_{D,l}} = K_{sl}(\vec{u}_s - \vec{u}_l) \tag{2.15}$$

where K_{sl} is the liquid-solid momentum exchange coefficient. Three manners to model this coefficient are described here.

I. For spherical particles, the coefficient K_{sl} may be derived analytically, thus its simplest formulation is expressed as follows:

$$K_{sl} = \frac{3}{4}\rho_l \alpha_l \alpha_s \frac{C_D}{d}\left|\vec{u}_s - \vec{u}_l\right| \tag{2.16}$$

where C_D is the drag coefficient and d is the diameter. The drag coefficient is modelled using an empirical correlation which was developed for laminar flows by [Schiller and

Nauman, 1935]:

$$C_D = \begin{cases} \frac{24(1+0.15Re^{0.687})}{Re} & \text{if } Re \leq 1000 \\ 0.44 & \text{if } Re > 1000 \end{cases} \tag{2.17}$$

where Re is here the relative Reynolds number for the continuous phase l and the dispersed phase s:

$$Re = \frac{\rho_l \left|\vec{u}_s - \vec{u}_l\right| d}{\mu_l} \tag{2.18}$$

II. [Niezgoda-Želasko and Zalewski, 2006b] used the Syamlal-O'Brien model (see [Syamlal and O'Brien, 1989]) for K_{sl}:

$$K_{sl} = \frac{3\alpha_s\alpha_l\rho_l}{4\omega_s^2 d}\left(0.63 + \frac{4.8}{\sqrt{\frac{Re_s}{\omega_s}}}\right)^2 \left(\frac{\rho_l d|\vec{u}_s - \vec{u}_l|}{\mu_l\omega_s}\right)|\vec{u}_s - \vec{u}_l| \tag{2.19}$$

where the settling velocity of the particles ω_s is given by [Garside and R. Al-Dibouni, 1977]. In the laminar regime, this model seems to underestimate the pressure drop comparatively to experimental results.

III. [Gidaspow, 1994]'s formulation of the liquid-solid momentum coefficient is employed by [Wang *et al.*, 2013a] as well as [Zhang and Shi, 2015], who both apply the kinetic theory of granular flows.

$$K_{sl} = \begin{cases} \frac{3C_D\alpha_s\alpha_l\rho_l|\vec{u}_s - \vec{u}_l|\alpha_l^{-2.65}}{4d} & \text{if } \alpha_s < 0.2 \\ \frac{150\alpha_s^2\mu_l}{\alpha_l d^2} + \frac{1.75\rho_l\alpha_s|\vec{u}_s - \vec{u}_l|}{d} & \text{if } \alpha_s \geq 0.2 \end{cases} \tag{2.20}$$

To the short description of the kinetic theory made previously, one can add that, in such a model, the fluctuating solid particle motion is described by the granular temperature θ_s which is proportional to the mean square particle fluctuating velocity: $\theta_s = \frac{1}{3}\overline{u_s' u_s'}$, where u_s' is the particle fluctuating velocity. The granular temperature is determined by a particular fluctuating energy transport equation [Wang *et al.*, 2013a; Zhang and Shi, 2015]. Qualitative considerations on the Euler multiphase approach based on the kinetic theory tend to say that it is appropriate for modelling the flow of ice slurry in horizontal pipes.

[Zhang and Shi, 2015] applied the Eulerian model for ice slurry flows in a horizontal pipe of $D = 9$ mm and for ice particles of $d = 0.27$ mm. Numerical results for the pressure drops agree well with the experimental data (Figure 2.14). This indicates that for simple geometries at least the multiphase Eulerian model with this specific formulation can de-

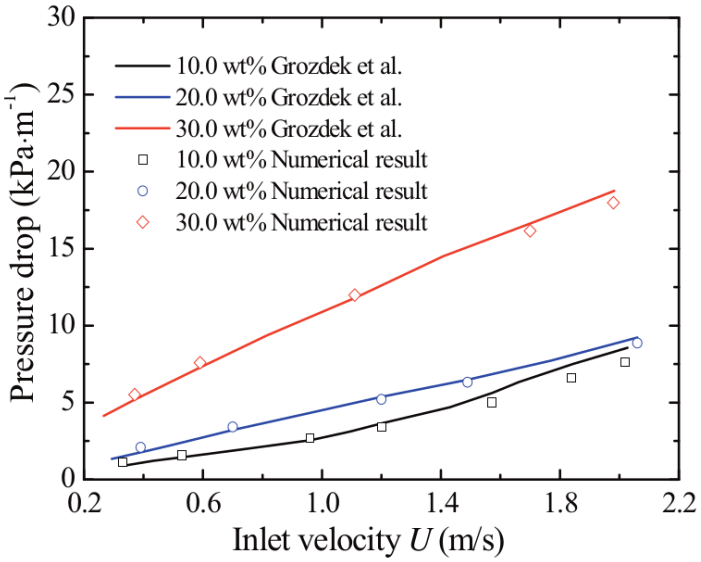

Figure 2.14 Comparison of the numerical pressure drop with experimental data, after [Zhang and Shi, 2015].

scribe accurately the pressure drops.

The mixture model is designed for two or more phases. As in the Eulerian model, the phases are treated as inter-penetrating continua. The mixture model resolves a mixture momentum equation and specifies relative velocities to describe the dispersed phases. Supplementary momentum equations may also be solved for the secondary phases. Applications of the mixture model include particle-laden flows with low loading, bubbly flows or sedimentation (see an interest for slurry stratification). The mixture model can also be used without relative velocities for the dispersed phases to model homogeneous multiphase flows, which seems rather adapted to ice slurry flows.

The mixture model presented by [Wang *et al.*, 2013b] is applied to capture the isothermal flow characteristics of ice slurry in horizontal pipes. Here are the continuity and momentum equations:

$$\frac{\partial}{\partial t}(\rho_m) + \nabla \cdot (\rho_m \vec{u}_m) = \dot{m} \tag{2.21}$$

where the subscript m represents the mixture phase.

$$\frac{\partial}{\partial t}(\rho_m \vec{u}_m) + \nabla \cdot (\rho_m \vec{u}_m \vec{u}_m) = -\nabla p + \nabla \bar{\bar{\tau}}_m + \rho_m \vec{g} + \nabla \cdot \left(\sum_{i=1}^{2} \alpha_i \rho_i \vec{u}_{Di} \vec{u}_{Di} \right) \tag{2.22}$$

where the subscript i represents the phase (solid s or liquid l). u_{Di} represents the drift velocity which is defined as the ith phase velocity relative to the mixture phase velocity. In the model of [Wang *et al.*, 2013b], the drift velocity for each phase is described according to the expression given by [Lin and Ebadian, 2008], who also gave their slip formulation for the slip velocity − a particular u_{ls} used in the last expression. In their ice slurry flow study, [Niezgoda-Želasko and Zalewski, 2006b] used a simpler formulation for the slip velocity, proposed by [Manninen *et al.*, 1996]. Though this last formulation does not take into account turbulence.

The volume fraction equation for the particle phase is presented below:

$$\frac{\partial}{\partial t}(\alpha_s \rho_s) + \nabla \cdot (\alpha_s \rho_s \vec{u}_m) = -\nabla \cdot (\alpha_s \rho_s \vec{u}_{Ds}) \tag{2.23}$$

For the Mixture model, the dynamic viscosity of particulate solids may have to be known, which is absolutely not trivial. For instance, [Niezgoda-Želasko and Zalewski, 2006b] used a formulation of their mixture viscosity defined according to the volume fractions and viscosities of each phase. [Wang *et al.*, 2013b] re-used the Thomas equation for a part of their research and the Bingham model for another part. This choice may have a non-negligible impact on the results. [Niezgoda-Želasko and Zalewski, 2006b] found that the numerical results were in good conformity with the experimental ones, from a dynamical point of view though. [Wang *et al.*, 2013b] probably conducted the most detailed study including the Mixture model. They took back their previous work [Wang *et al.*, 2013a] and, this time, they tried a mixture CFD model for ice slurry flows, then validated it with three different experiments. The flow is isothermal and the rheological behaviour is taken into account by a Bingham model. One interesting observation remains that, when the mean flow velocity is high, the Thomas equation seems sufficient to describe the ice slurry viscosity, whereas when the velocity decreases, the Bingham rheological model is required. Such a model would be effective for describing *heterogeneous* ice slurry flows with ±15% relative error and would supply plentiful flow information.

The main problems to solve remain the wall shear stress and the stratification. The authors noticed that the accuracy of the Mixture model declines when applied to sand slurry near the pipe wall (Figure 2.15). One can imagine the same issue for ice slurries. The phase slip becomes significant near the pipe wall whereas the algebraic slip formulation is not accurate enough to describe the phase slip. Therefore the particle repelling phenomenon could not be captured by this model. It seems of interest to notice the good compliance

between the results in the middle part of the flow, contrarily to the bottom and top of the pipe where remarkable differences appear.

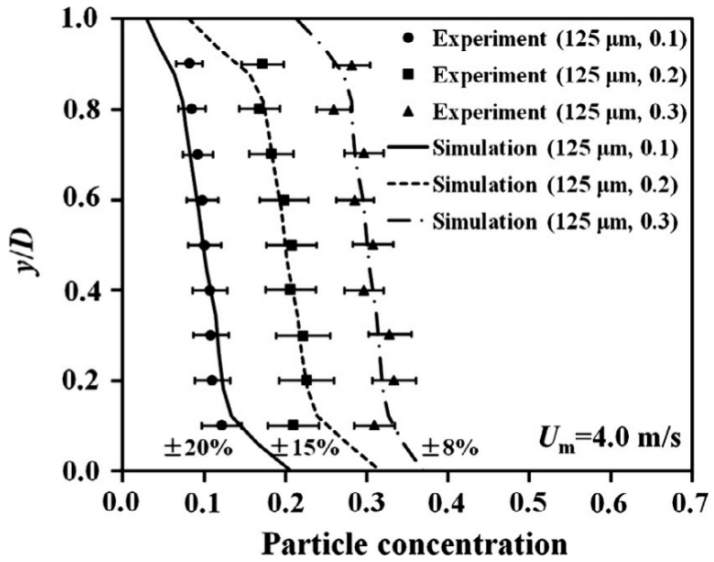

Figure 2.15 Concentration profiles in a horizontal liquid–solid (sand) slurry flow, after [Wang *et al.*, 2013b].

Thus, the future axes of research are orientated towards the development of a model characterizing heterogeneous ice slurry flow and concentration distribution, simultaneously. Here, the algebraic slip formulation given by [Lin and Ebadian, 2008] allows to describe phase interpenetration. So, the main amelioration brought in this last study [Wang *et al.*, 2013b], compared to [Niezgoda-Želasko and Zalewski, 2006b], is the concentration distribution supply, which brings further information than the velocity profiles only. Moreover, ice slurry rheological behaviour is now coupled with flow and concentration distribution.

The *Eulerian model* tends to predict good values for the dynamic variables when applied to simple pipe ice slurry flows. Now, it is important to see if such good results would appear with thermal variables as well. With the *mixture model*, the main problems occur in the near-wall region, where the repelling effect on solid particles remains badly captured. Otherwise, numerical results are in rather good conformity with experimental values. Eventually, it would seem interesting to compare the numerical costs of the different models and to apply them to various kinds of flows (winding, elbowed, etc).

2.3.2 Specific analytical models

They are based on phenomenological/empirical approaches of slurry flows. As mentioned, such flows are not only homogeneous, since stratification phenomena are often observed, especially for higher ice concentration levels and lower flow velocities. From these observations, several models have been designed to directly account for the inhomogeneity or even the several layers likely to appear in ice slurry flows.

The two-layer model used by [Stutz and Reghem, 2001; Stutz *et al.*, 2001] has been proposed first by [Takahashi *et al.*, 1991]. This model allows to calculate the pressure drop within a permanent ice slurry flow for which a solid particle layer forms on the upper region of the pipe and a heterogeneous layer developed in the lower region (Figure 2.16). The

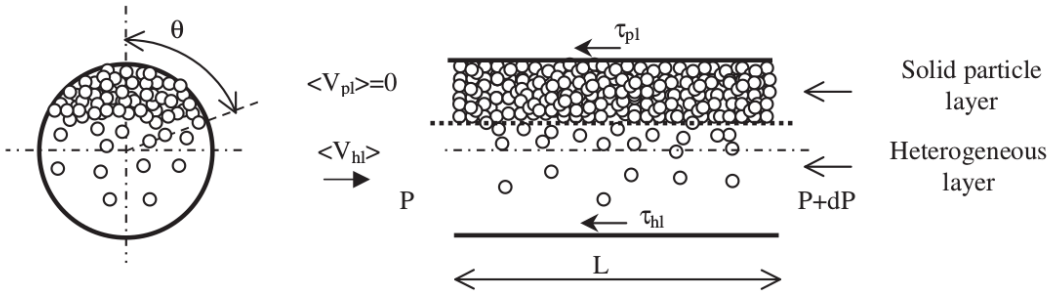

Figure 2.16 Schematic diagram of the two-layer model, after [Stutz *et al.*, 2001].

modelling lays on several assumptions: i. heterogeneous layer is very little concentrated, ii. particle density is close to that of water, iii. velocity of the particle layer V_{pl} is negligible compared to heterogeneous layer's one V_{hl}. Thus, the equation for the heterogeneous layer velocity can be written as:

$$< V_{hl} >= \frac{\pi}{(\pi - \theta + sin\theta cos\theta)^2} \frac{Q(1-\phi)}{A} \tag{2.24}$$

where A is the pipe cross-section area, Q the volumetric flow rate and θ, as shown on Figure 2.16, is calculated from the empirical equation $\theta = \alpha(0.059Fr^{-1} - 0.09)$ for $Fr < 38$ and $\theta = 0$ for $Fr \geq 38$. α is a kinetic energy correction factor. The Froude number, defined as $Fr = U_m^2/Dg(1 - \rho_i/\rho_l)$, normally allows to determine the pattern behaviour.
From the velocity equation (2.24), the different wall shear stresses (τ_{pl} for the particle layer and τ_{hl} for the heterogeneous layer) can be deduced and thus the pressure drop dP/dz. Anyway, [Stutz *et al.*, 2001] found that the hypothesis of the modelling was wrong: the liquid flow rate in the particle bed is not negligible, otherwise it annihilates the global mass

and momentum balances. Then, this lead to incorrect results compared to experimental data.

Earlier, [Doron *et al.*, 1987] also developed a two-layer model which allows to account for various flow patterns: stationary bed, moving bed and fully suspended (only one layer). The model considers also a heterogeneous layer and a bed layer for slurry flows. But this time, the velocity of the bed layer and the concentration of the solids within the heterogeneous layer are not considered negligible. Moreover, in the heterogeneous layer, a diffusion equation is analytically solved − this one balances turbulent dispersion with particle sedimentation, see equation 2.25 − giving a non-constant concentration profile of the solid particles in the layer. Compared to experimental data, the model gave good estimations of pressure drops for straight pipe flows ($D = 50$ mm) of water with black acetal particles ($d = 3$ mm, $\rho_s = 1240\ kg.m^{-3}$), especially in the turbulent flow regime.

The three-layer model was originally developed by [Doron and Barnea, 1993] to improve their previous two-layer model [Doron *et al.*, 1987]. A brief review is done in [Doron and Barnea, 1996]. The principal elements are here quoted.

At low mixture velocities, the flow consists of three layers: a stationary deposit at the bottom of the pipe, a moving bed layer above it and an upper layer which contains a heterogeneous suspended mixture as the authors considered solids heavier than the carrier fluid.

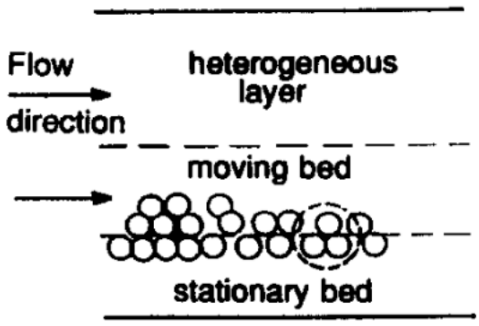

Figure 2.17 Schematic representation of a slurry flow, after [Doron and Barnea, 1993].

The height of the stationary bed is postulated to be such that the velocity of the moving bed above is at a certain minimal value. When the moving bed velocity assumes this value, the particles at the interface between the two bed layers are at the verge of rolling. For this condition, the driving torque acting on a particle at the lowermost stratum of the moving layer (i.e. right at the interface between the stationary layer and the moving layer,

see the circled area on Figure 2.17) should be equal to the opposing torque acting on that particle. The torque balance yields the required minimal bed velocity (1 equation).
Continuity equations (2 equations) and force balance equations (2 equations) are respectively written for the two phases (liquid and solid) and for the two flowing layers (moving bed layer and heterogeneous layer). The force balance over the stationary bed is not part of the solution process, as it only yields an inequality ([Doron and Barnea, 1996]), which serves as verification for the existence of this layer.
The dispersion of the solid particles in the upper layer is represented by the diffusion equation (Equation (2.25)).

The resolution of the six-equation system allows to determine the mean velocity of the upper layer, the mean velocity of the moving bed, the mean concentration of the upper layer, the height of the moving bed, the height of the stationary bed and the pressure gradient. The existence of the flow patterns are found from the height of the layers. For instance: when stationary bed height reaches 0 m, the layer has disappeared, and then the calculation is done for the moving bed. The model results showed good conformity with experimental data [Doron and Barnea, 1995] (flow conditions similar to [Doron *et al.*, 1987]), improving the previous two-layer model [Doron *et al.*, 1987].

The heterogeneous flow modelling of [Kitanovski and Poredoš, 2002] for ice slurry flows derives from previous two- and three-layer models [Doron and Barnea, 1993; Doron *et al.*, 1987]. It assumes fully suspended ice slurry flows − without particle bed − and the particle homogeneity in each tiny mixture volume. Eventually, the model yields a concentration profile along the vertical pipe diameter $0 < y/D < 1$.

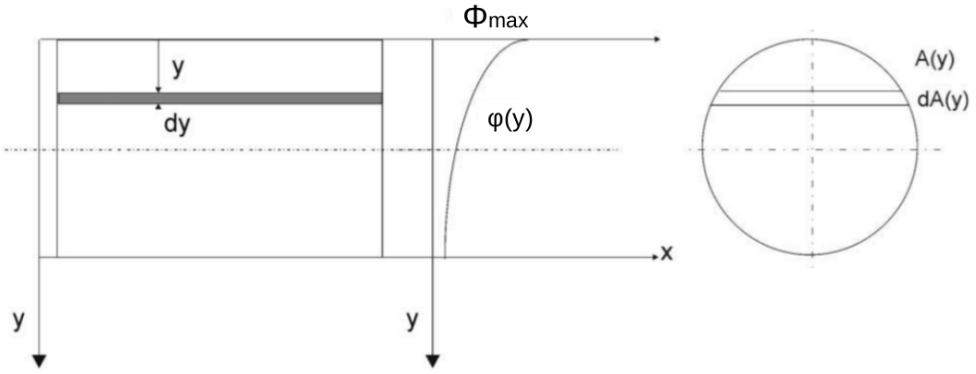

Figure 2.18 Concentration profiles for ice slurry flows, after the analytical model of [Kitanovski and Poredoš, 2002].

The main elements of this model are recalled hereafter:

$$\epsilon \frac{d^2\phi}{dy^2} + \omega \frac{d\phi}{dy} = 0 \tag{2.25}$$

The analytical result of equation (2.25) is written below:

$$\phi(y) = \Phi_{max} e^{-\frac{\omega}{\epsilon}} \tag{2.26}$$

Integrating the previous equation (2.26) on the whole pipe cross-section area A (see Figure 2.18) allows to find the maximum ice concentration Φ_{max} at the top of the pipe, as expressed hereafter:

$$\Phi_{max} = \Phi_m A \left(\int_A e^{-\frac{\omega}{\epsilon}} \, \mathrm{d}A(y) \right)^{-1} \tag{2.27}$$

The terminal settling velocity of the particle ω is calculated from [Richardson and Zaki, 1954]. The local diffusion coefficient ϵ accounts for the dispersion effects of turbulence. It is calculated through equation (2.28):

$$\epsilon = 0.052 \nu^* r_h \tag{2.28}$$

where r_h is the hydraulic radius ($= D/2$ in the present case) and ν^* is the shear velocity given by [Doron and Barnea, 1993]. Anyhow, one recalls that this variable is a function of the Reynolds number Re, the pipe and particle diameters D and d, the mean flow velocity U_m. Concentration profiles are plotted for ice slurry flows in horizontal pipe of diameter $D = 27.2$ mm. Particle diameter is $d = 1$ mm, the slurry is made from an initial solution of 10 $wt.\%$-ethanol. Flow velocity U_m varies from 0.5 $m.s^{-1}$ to 2 $m.s^{-1}$ and mean ice fraction $\Phi_m = 0.1$ and 0.2. Presently, the profiles were not compared to experimental data. Albeit, used in the two- and three-layer models [Doron and Barnea, 1993; Doron *et al.*, 1987], the heterogeneous modelling contributed to lead to good conformity with experimental data for particle concentration profiles and pressure drops.

2.4 Brief summary

Through the analysis of the state of the art, for both experimental and numerical works, few research requirements were established. Concerning the experimental part, the lack of accurate and specific data for the characterisation of the flow patterns and their transition modes reinforces the necessity to carry on further investigation in this way. Moreover, only one study inquired the correlations that might exist between the flow patterns and

the pressure drop evolution. Thus, it also appears of prime importance to see the possible impacts of the flow patterns on some hydrodynamic quantities (such as the pressure drop or the friction factor). Concerning the numerical part, and the ice slurry flow modelling particularly, three principal ways are considered. The first one is the single-phase modelling that consists in the classical Navier-Stokes equations with the addition of a modified viscosity. In order to do so, either a suspension viscosity correlation can be employed or a non-Newtonian viscosity law. This type of modelling assumes a homogeneous fluid mixture, which is a very strong assumption, since it is rarely the case for ice slurries. To tackle this issue, the two-phase modelling reveals quite efficient. With ice slurry flows specifically, either the Eulerian model was employed or the mixture model. The former is known to be more complete in terms of the suspension flow phenomenology account, but much also more expensive in terms of computational costs. Then, with both single-phase and two-phase modellings, a turbulence model can be coupled. In the context of ice slurries, mainly k-ε models were employed but without any clear justification. Other turbulence models have then to be assessed. According to these previous observations, an accurate, reliable, low-cost and comprehensive model remains to be built for better ice slurry flow prediction and understanding.

CHAPTER 3

EXPERIMENTAL CHARACTERISATION OF ISOTHERMAL ICE SLURRY FLOWS

The experimental part of the research work examines the flow regimes encountered within ice slurry as well as their dependency on quantitative flow parameters such as the ice concentration, the flow rate and the pressure drops. Section (3.1) introduces the methodology, with a presentation of the test bench and of the tools enabling the data collection. Section (3.2) is dedicated to the description of the flow patterns, their evolution and the conditions of their emergence. Sections (3.3 and 3.4) then seek the relations between the qualitative observations and the various measured data. Pressure drops are notably investigated for flows through horizontal straight pipe but also through piping involving singularities.

3.1 Experimental methodology

3.1.1 Set up and apparatus

Globally, the set up comprises 3 principal parts. A global view is shown in Figure 3.1.

The first part is the ice generation loop along which an ice slurry generator (MuellerMaximICE, Model ORE-3) − nominal cooling capacity of 11 kW − is set (referred as **gen.** in Fig. 3.2a). The aqueous solution incorporates a freezing-point depressant, being here mono-propylene glycol with an initial concentration of 9.5% in mass. According to the manufacturer of the slurry generator, the size of the produced ice crystals ranges from about 150 to 350 μm with an average size of about $200 - 250$ μm. The loop starts at the very bottom of a mixing tank (in order to drain a maximum of less concentrated mixture) and goes back on the upper part of this last with the two-phase mixture produced upward.

The second part is the **mixing tank** equipped with a rotary mixer to ensure uniform distribution of the ice particles and to store it isothermally. Its volume capacity is 0.8 m^3. Note that, as the mixing tank, all the piping and devices are thermally insulated.

The third part includes the **test area**, where the flow measurements are done. Before this, the loop starts from the tank, with the exit being placed at half height. This tackles the stratification phenomenon − as ice particles always tend to go up in the tank, even

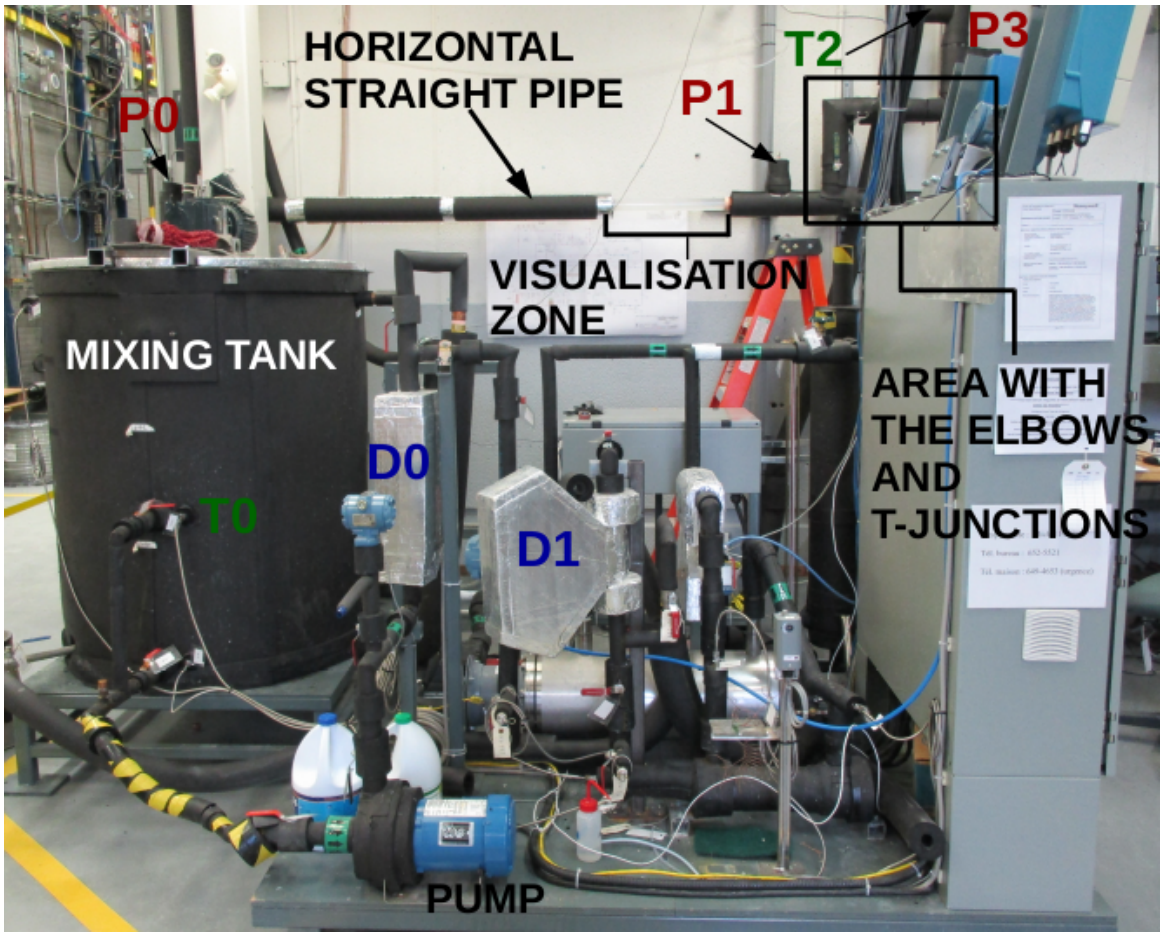

Figure 3.1 Photograph of the test bench available at CanmetEnergy in Varennes.

when the mixing power is elevated, and to be more concentrated at the surface and less at the bottom − and an average ice content is always drawn out. Downward, a **pump** is set on the conduct: its power allows to reach a mass flow rate of 40 $kg.min^{-1}$ ($\Leftrightarrow$ a mean flow velocity of 0.58 $m.s^{-1}$). The flow then enters the test area: a long straight pipe of diameter $D = 0.03823\ m$ which is terminated by a 0.5-meter portion of transparent pipe (referred as the **visualisation zone** in Fig. 3.2a), enabling the observation of the different flow patterns. The long straight pipe is framed by two pressure sensors − **P0** and **P1**, for which four holes of 1 mm are drilled in the pipe wall every 90° − separated by a length $L = 2.33$ m and linked to an Endress+Hauser Deltabar S PMD75 platform to get differential pressure measurements. The measurement range is comprised between 0 and 1000 Pa with an accuracy of ±0.9 Pa.

The second element of the test area, just following the long straight pipe, is composed of elbows and T-junctions (Fig 3.2b). Another pressure sensor **P2** is set right after this

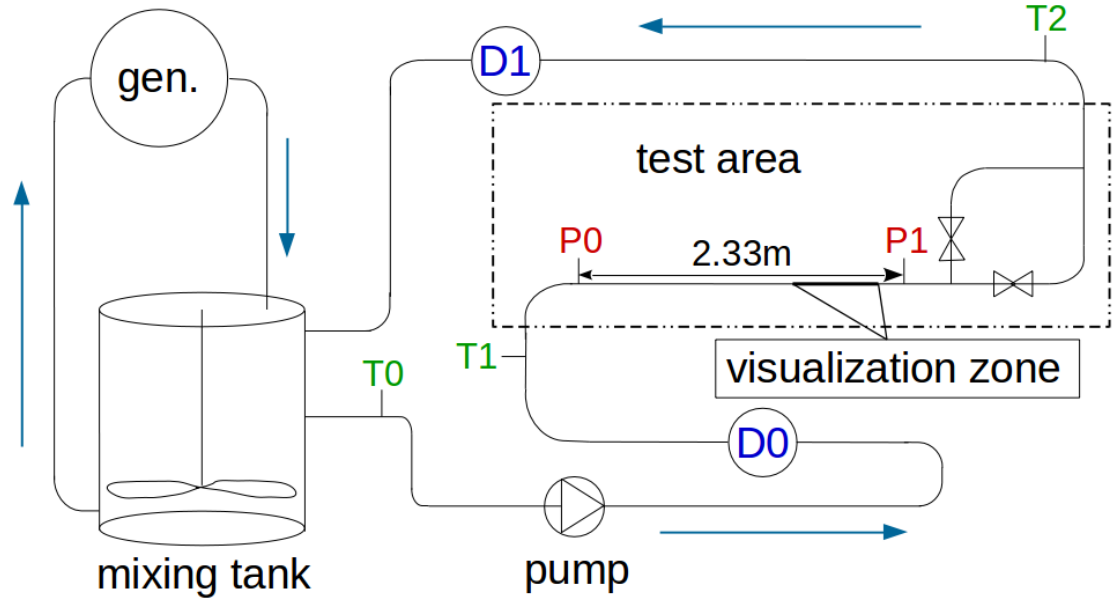

(a)

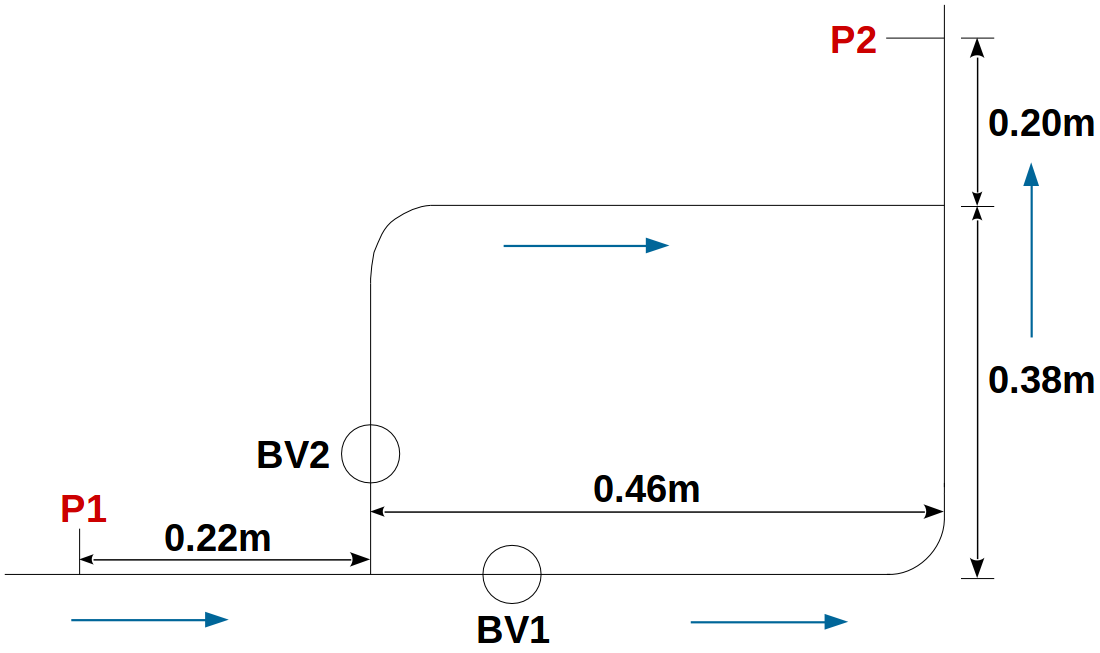

(b)

Figure 3.2 (a) Schematic view of the experimental set-up with (b) a zoom on the elbowed part. Blue arrows symbolize the flow direction.

part (connected to the aforementioned platform) in order to get the pressure drop there

(i.e. between P1 and P2). Two ball valves **BV1** and **BV2** are installed on each branch in order to study three different configurations.

Three main thermocouples (RTD Pt 100) are included in the set up (referred as **T0**, **T1** and **T2** in Fig. 3.2a): one at the exit of the mixing tank and two others at the beginning and exit of the test area. They all range from -20 to $20°C$ with an accuracy of $\pm 0.05°C$. As well, two densitometers (referred as **D0** and **D1** in Fig. 3.2a) are positioned upward and downward the test area. The first one is an Endress+Hauser Promass 83F15 and the second one is an Emerson Micro Motion Elite CMF050M. According to the manufacturer, both range from 975 to 1030 $kg.m^{-3}$, the first one has an accuracy of $\pm 0.5 kg.m^{-3}$ and the second one of $\pm 0.2 kg.m^{-3}$.

3.1.2 Elements of methodology

The greatest issue of this experimental study was to determine the most accurately possible the ice content flowing through the test area. The initial liquid solution is made of water with 9.5% mass fraction propylene glycol. To obtain the properties of such a solution, the Handbook [Ashrae *et al.*, 2013] is used. When the mixture flows, the temperature does not vary from a thermocouple to another. The maximum absolute difference is $0.05°C$, observed between T0 to T2 at low flow rates. The maximum absolute difference for the density 0.4 $kg.m^{-3}$ obtained between D0 and D1 remains very weak too. Firstly, this correlates the fact that the entire system is well insulated. Secondly, supposing the thermal equilibrium of the system at a given time, the temperature data is sufficient to give a *global* estimation of the mean ice fraction. The term "global" is employed because it had been noticed that, most of the time, a contradiction remains between the calculated ice fraction at a certain mixture temperature (given by the correlation of [Ashrae *et al.*, 2013]) and the density of the mixture itself (directly measured). Even with quite high stirring velocities in the mixing tank, the ice slurry mixture never seems to reach a perfect particulate vertical homogeneity so that the pumped mixture may comprise ice fractions lower than the one the entire system really has. It may be explained by the buoyancy force, which always tends to accumulate the particles towards the surface. Thus, supposing that the density of the liquid phase remains unchanged anywhere in the system at a certain temperature, it is preferable to evaluate the ice fraction using the density parameter. The densitometers provide a measure of the mixture density ρ_{is}. The ice density ρ_s and the liquid density ρ_l are already known as a function of the mixture temperature T_{is} according

to existing correlations [Ashrae *et al.*, 2013]. The inlet volume ice fraction Φ_m is then deduced from:

$$\Phi_m = \frac{\rho_{is} - \rho_l}{\rho_s - \rho_l} \tag{3.1}$$

Visual inspections are done − through the **visualisation zone**. It remains the best way to determine the flow patterns as one can have a 3D-moving vision around the pipe. Despite the fact that the observations have been treated with very particular care, it may have been hard to distinguish the exact flow patterns (position, relative movement, motion of the flow elements) due to the opacity of ice particles, especially at higher concentrations or higher flow rates, and to the condensation sometimes forming on the outer wall of the pipe. However, schemes and photographs of the flowing ice slurry mixture are shown later on, always attempting to reproduce the patterns with the highest accuracy and likelihood. Photographs and films were taken from a camera Canon EOS 70D with an objective lens EFS 18-200mm.

Different experiments have been carried out by varying the ice slurry flow rate and the ice mass fraction. At the beginning of each experiment, the slurry generator and the data acquisition system are turned on. The rotary mixer and the test section pump are run continuously to ensure uniform dispersion of ice particles in the tank and to circulate the slurry through the test section where the pressure difference, the temperature, the density and the flow rate are measured. The ice mass fraction in the circuit and in the tank increase gradually until it reaches the desired value at which point the generator is turned off. It may take more than 2 hours depending on the operating parameters. Then, the ice mass fraction decreases very slowly due to heat gains from the environment [Renaud-Boivin *et al.*, 2012]. At a fixed flow rate, the temperature, density, ice fraction and pressure drop remain constant over a certain time period, during which the measurements are done.

3.2 Flow patterns in a horizontal straight pipe

3.2.1 Description and classification

Presently, the flow patterns and their evolutions seem quite different from what has been currently reported in [Kauffeld *et al.*, 2005]. Although one may recognize some common features, more clarification is required. Hereafter, 6 principal flow regimes distributed through 3 different families may be distinguished. Their evolution is given as a function

of the mean flow velocity U_m. The first flow regime corresponds to the highest applied velocities ($U_m \geq 0.35\ m.s^{-1}$) whereas the fifth and sixth flow regimes to the lowest one ($U_m \simeq 0.073\ m.s^{-1}$).

Nota: On each couple of figures, a scheme (a) gives details of what can be observed on the photograph (b). Black lines are drawn on these photographs to differentiate the various layers.

1. *Pure homogeneous flow* (P-Ho)

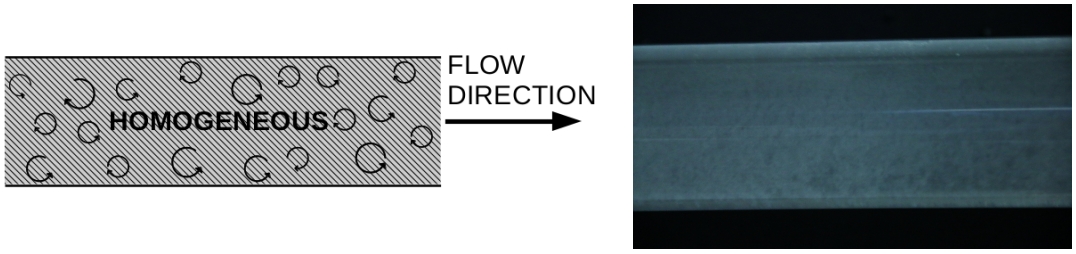

(a) (b)

Figure 3.3 (a) Scheme of the flow pattern. (b) Corresponding photograph.

There, the flow seems perfectly homogeneous. The agitation and the inter-particle collisions are strong enough to maintain an uniform repartition of the ice particles over the whole pipe cross-section.

2. *Degraded homogeneous flow* (D-Ho)

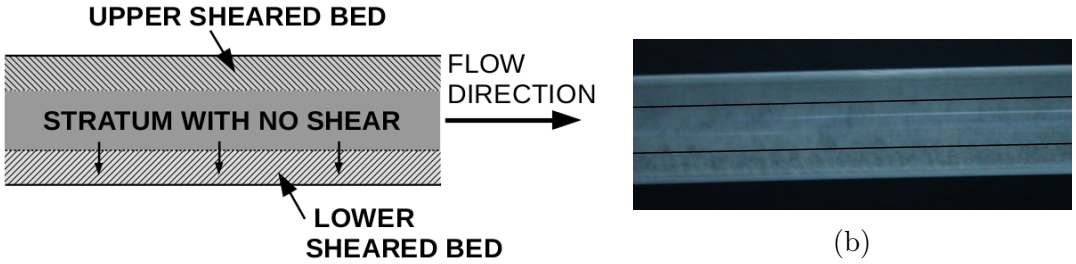

(a) (b)

Figure 3.4 (a) Scheme of the flow pattern. (b) Corresponding photograph.

The flow velocity is slightly reduced and the ice particles still occupy the entire pipe section quite homogeneously. Albeit, a stratum of low shear appears along the pipe middle height − with no apparent shear at all in several cases − where the particles gather in coarser aggregates. The lower sheared bed may seem a little less concentrated than the upper one. Sometimes, this step seems to be skipped.

3. *Stratified flow #1* (St #1)

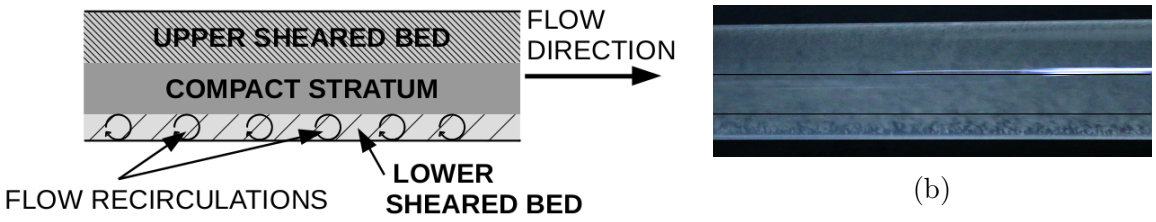

(a) (b)

Figure 3.5 (a) Scheme of the flow pattern. (b) Corresponding photograph.

The previous stratum of low shear becomes fully compact and forms a distinct layer – sliding more rapidly between the two others. This layer also tends to go down with the decrease of the flow velocity. It is surmounted by a sheared bed, made of thinner and denser aggregates (showing clear recirculations sometimes), that gets thicker as the velocity diminishes. At the bottom of the pipe, the other sheared bed gets thinner and less concentrated, and many small swirls can be seen along as if the compact layer above was moving on rolls. In several cases (when U_m passes under a critical velocity U_c), no more ice particle remains within the lower layer.

4. *Stratified flow #2* (St #2)

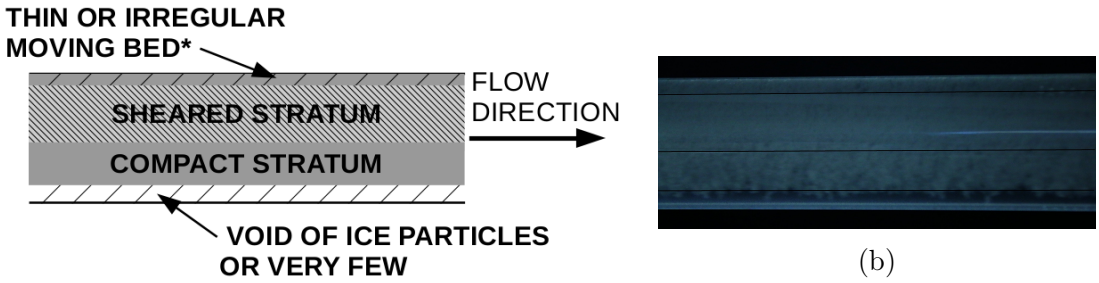

(a) (b)

Figure 3.6 (a) Scheme of the flow pattern. (b) Corresponding photograph.

This stage is reached either (i) when a new stratum shows up at the top of the pipe (a thin moving bed or long discontinuous blocks sliding on the upper wall and dragged by a dense sheared stratum located below) or (ii) when the compact middle stratum tends to lower under the pipe half height and becomes quite thin and unstable, made of bigger aggregates of ice particles disturbed by the flow. The small layer remaining below is most

of the time empty of ice particles. One may also observe both phenomena at the same time. Note that for the highest inlet ice volume fractions ($\Phi_m > 12\%$), this entire step seems skipped as the middle compact stratum tends to grow in diameter until it forms a complete "solid" column.

5. *Stratified flow #3* (St #3) − or *moving bed like*

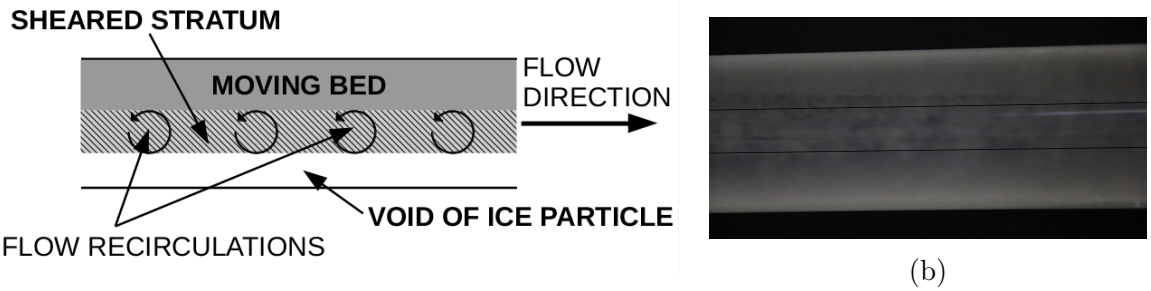

(a) (b)

Figure 3.7 (a) Scheme of the flow pattern. (b) Corresponding photograph.

There, only remains the upper moving bed dragged by a sheared layer of coarse aggregates just below. Sometimes, the sheared layer gathers with the moving bed so that only a thick moving bed subsists at the top. This step does not seem to occur for the higher Φ_m and is the last observed for the lower Φ_m.

6. *Annular flow* (An) − or *column-like*

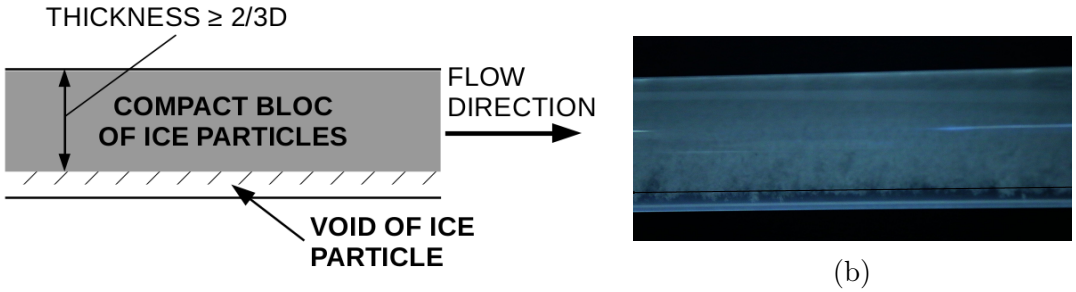

(a) (b)

Figure 3.8 (a) Scheme of the flow pattern. (b) Corresponding photograph.

Annular flows have been encountered only for $\Phi_m > 12\%$ and $U_m = 0.073\ m.s^{-1}$. Even if a solid block has formed, one can see on (b) that an ice density gradient crosses the column. Coarser but fewer ice aggregates stay at the bottom whereas thinner but denser gather towards the top.

Some remarks:

No pure heterogeneous flow seems to have been noticed throughout the experiments: when stratification appears, compact structures seem to form at the same time and several distinct strata can be identified within the flow. Moreover, pure moving bed observations remain quite rare (flow regime 5: St #3) − even after having tested quite large ranges of flow rate and ice concentration. It is almost always accompanied by a sheared stratum of particles just below. *Here, stratified really signifies that two or more distinct strata clearly form within the flow (either compact, sheared or with no particle), and thus it does not straightly imply a phase separation.*

A major observation is the apparition of a compact layer at middle pipe height, around flow regimes D-Ho and St #1. This compact layer is moved down with the velocity decrease. The low shear around the pipe axis, especially when the flow is homogeneous at higher velocities, added to the coalescent nature of the ice particles would provoke the formation of a "solid" block over this area. Then, an important shearing in the region located between the upper wall and the compact layer (also the region of highest ice concentration due to buoyancy forces), sometimes accompanied by strong flow recirculations, would cause the coalesced-particle layer to be progressively repelled from the top wall.

For the higher ice volume fractions, i.e $\Phi_m > 12\%$, where only the first of the three stratified regimes is noticed, the middle compact stratum tends to thicken with the velocity decrease and could even be qualified of "rigid column" around $U_m = 0.15\ m.s^{-1}$ − though sheared particles still surround it. *Annular* regime (flow regime 6) clearly appears at the lowest flow velocity, i.e. where the flow elements tend to present an axial symmetry along the pipe direction and only one rigid bloc of ice particles flows. Such a category was only reported by [Reghem, 2002] for ice slurry flows.

No stationary bed was noticed through the experiments as the flow rate was always strong enough to yield the whole mixture, even in fully separated flows (with well separate and parallel streams of two or more phases $\Leftrightarrow$ saltation).

[Hirochi *et al.*, 2004] used a totally different way to classify the flow patterns observed with their ice slurry flows, which some elements recalled the present observation. Only three categories were developed: (i) *dispersed-particle flow*, which would correspond to the homogeneous flow, or even heterogeneous, since solid particles fill the whole cross-section of the pipe ; (ii) *cluster flow*, when ice particles gather and form blocks of different sizes moving along with the flow; (iii) *column flow*, a cylindrical rigid body of variable diameter forms within mixture flow. The authors insisted on two facts. First, no "saltation flow" (regime identified as static or moving bed) was observed during their experimentations, though they used three different types of ice particles with various sizes, as well as var-

ious pipe diameters. Similarly, the present experimentations rather showed flows where a compact layer slides between sheared ones. As an approximative symmetry presently appears within the flow for higher ice concentrations and lower flow velocities, it could be related to column flows. Second, the cohesive nature of the ice particles dominates ice slurry flows. Such a characteristic becomes highly preponderant for flow conditions in which the particle buoyancy has a very little influence. It is consistent with the recurrent observations of a compact stratum moving with the flow even at relatively high velocities (see flow regime St #1, or even D-Ho, where coarser aggregates seem to form around the pipe axis). A block more or less cylindrical rapidly forms around the pipe axis when the velocity decreases. Even though the coalesced-particle block is clearly cylindrical, it would be more rigorous to call it cluster or column flow than moving bed or heterogeneous flow − since heterogeneous generally does not imply a compact layer and moving bed supposes a compact layer, but sliding on the wall.
The term *Column flow* was also employed by [Lee *et al.*, 2002] to describe their concentrated flows (ice content $> 15\%$) for all flow velocities. *Cluster flow* appellation would suggest that relative movements of big groups of ice particles may still occur, like in flow pattern 2, D-Ho. Albeit, it has been preferred to classify it as *stratified* since the observations could only show several flowing strata. Eventually, [Hirochi *et al.*, 2004]'s classification remains too simple and several flow features are missing.

3.2.2 Transition modes

Flow pattern maps

Observations through pipe wall showed, as presented in Fig. 3.9, that the more the flow rate − expressed here in terms of mean inlet velocity U_m − is augmented the less the flow tends to present compact structures as well as a phase segregation. This matches the different observations done by the researchers on slurry flows in general, see [Doron and Barnea, 1996; Turian and Yuan, 1977], and on ice slurry flows specifically, see [Hirochi *et al.*, 2004; Kitanovski *et al.*, 2002]. Concerning the effects of the ice concentration raise, some differences may be remarked. For instance, Figure 3.9 shows that the more ice volume fraction Φ_m is elevated the sooner − in velocity − the transition towards pure homogeneous regime (P-Ho) is triggered: for $\Phi_m = 2.1\%$, P-Ho is only seen at $U_m = 0.58$ $m.s^{-1}$, for $\Phi_m = 9.2\%$, P-Ho appears at $U_m = 0.51$ $m.s^{-1}$ and eventually, for $\Phi_m = 18.4\%$, P-Ho is already present at $U_m = 0.36$ $m.s^{-1}$.

[Doron and Barnea, 1996] rather exhibited a contradictory fact, saying that "fully suspended" flows − equivalent to *homogeneous* flows in the present context − are more likely

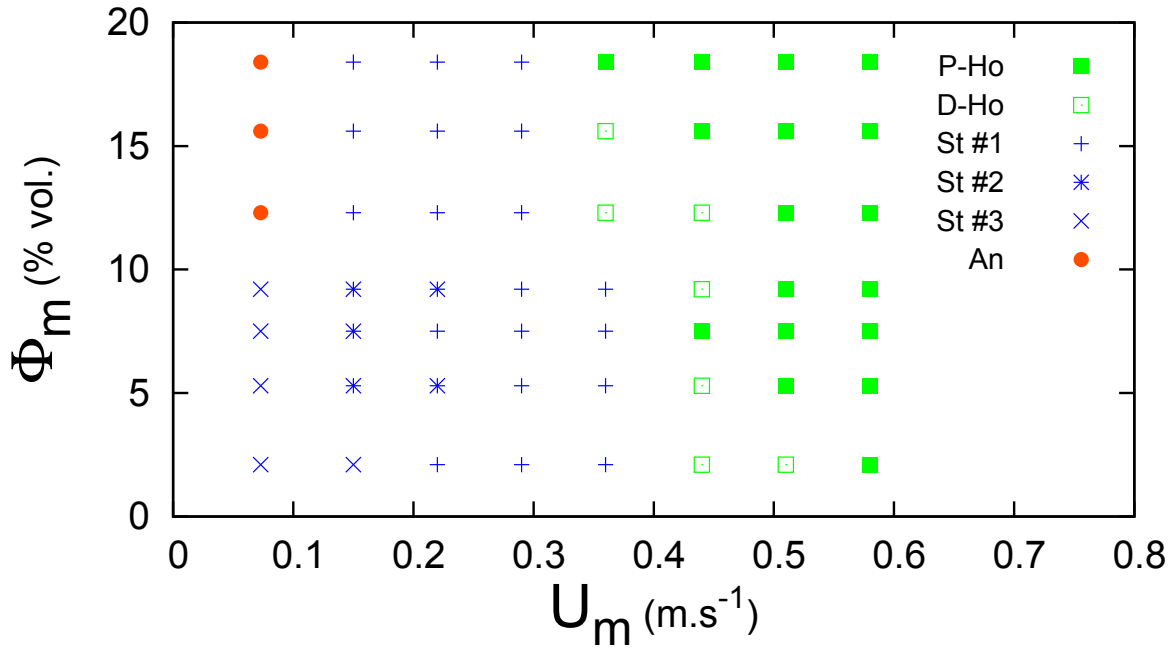

Figure 3.9 Map of the different flow patterns as a function of the inlet flow velocity U_m and ice volume fraction Φ_m.

to occur at low solid concentration and high flow velocity. Thus, according to [Doron and Barnea, 1996], the augmentation of the solid concentration would make the pattern change from "fully suspended" to "moving bed" at higher flow velocities. Even though moving bed flows are not much observed presently nor fully suspended flow can straightly be associated to homogeneous flow, transition from homogeneous (Ho) to stratified flows (St) is mainly triggered by the velocity variation and not by the ice concentration variation. Moreover, if "moving bed" implies a phase separation − contrarily to "fully suspended" −, Table 3.1 reports lower critical velocities (i.e. velocities marking the apparition of a phase separation) as the ice volume fraction raises, instead of higher critical velocities like expected by [Doron and Barnea, 1996].

[Reghem, 2002] showed close tendencies to the present ones. He also remarked that annular flows only form at higher ice concentration levels (towards 20% vol. in his study) and low velocities ($< 0.1\ m.s^{-1}$). Such a regime here appears with the same type of conditions: $U_m = 0.073\ m.s^{-1}$ and $\Phi_m > 12\%$. For lower ice contents and still low velocities, [Reghem, 2002] observed that, instead of annular, the flow was stratified − in his definition, it is similar to moving bed − which compares well with the present experimental observations. Otherwise, it is remarked that for low flow velocities, the pattern change is almost solely triggered by velocity change. It seems to correlate the various experimental results displayed in the study of [Kitanovski *et al.*, 2002].

Other cartographies, as in the works of [Kitanovski *et al.*, 2002; Turian *et al.*, 1971], provide the evolution of the flow patterns as a function of the particle size notably. In the present study, no mean enables to control such a parameter. However, the ice slurry generators now produce very thin ice particles ($d \sim 0.1$ mm), which corresponds to the present experimental conditions: the actual orbital rod generator is told to give ice particles with $0.050 < d < 0.1$ mm. Some further observations showed a diameter d around 0.1 mm. Otherwise, the mapping developed by [Hirochi *et al.*, 2004] − based on a non-dimensional parameter that incorporates the agitating energy of the flow and the energy required to disperse the particles − was not reproduced since the compressive yield stress is presently unknown and seems more relevant when the effects of varying the particle size are to be studied.

Transition criteria

As advised in the Handbook on Ice Slurries [Kauffeld *et al.*, 2005], the minimum velocity value U_{min} to avoid phase separation writes:

$$U_{min}^{K} = \mathbf{1.4}\sqrt{gD|1-s|} \quad \text{where} \quad s = \frac{\rho_i}{\rho_l} \tag{3.2}$$

One recalls that g is the gravitational acceleration and D is the pipe diameter.

U_{min}^{K} is the half of [Guilpart *et al.*, 1990]'s value:

$$U_{min}^{G} = 2 \times U_{min}^{K} \tag{3.3}$$

which is told to be recommended for additional safety, even re-employed in the study of [Wang *et al.*, 2017]. In the present case, $U_{min}^{K} = 0.26$-$0.27\ m.s^{-1}$ according to [Kauffeld *et al.*, 2005] and $U_{min}^{G} = 0.52$-$0.54\ m.s^{-1}$ according to [Guilpart *et al.*, 1990]. This *a priori* condition supposes that above such velocities, there is no risk of phase separation.

For $\Phi_m < 10\%$, Kauffeld's condition [Kauffeld *et al.*, 2005] is such as $U_{min}^{K} \in R_U$ (see Tab. 3.1) with considering that it just implies a flow separation, i.e. apparition of a pure liquid phase zone at the bottom of the pipe. Since no precise threshold velocity could be identified, it is possible that a separation appears between U_{min}^{K} and the upper bound of the R_U. Thus, for the lower ice fractions, an uncertainty remains concerning the condition validity. For ice concentrations $\Phi_m > 10\%$, the phase separation occurs only for $U_m < 0.22$

Φ_m (vol.)	R_U $(m.s^{-1})$	Pattern type
2.1%	$[0.22, 0.29]$	St #1
5.3%	$[0.22, 0.36]$	St #1 $\rightarrow$ St #2
7.5%	$[0.22, 0.29]$	St #1
9.2%	$[0.22, 0.36]$	St #1 $\rightarrow$ St #2
12.3%	$[0.073, 0.15]$	St #1 $\rightarrow$ An
15.6%	$[0.15, 0.22]$	St #1
18.4%	$[0.15, 0.22]$	St #1

Table 3.1 Ranges of velocities R_U for which a phase separation appears within the flow with the corresponding pattern type at each studied ice concentration Φ_m. St refers to stratified flows and An to an annular flow.

$m.s^{-1}$ and even 0.15 $m.s^{-1}$ (see Tab. 3.1) − which stays much lower than U^K_{min}. Guilpart's condition [Guilpart *et al.*, 1990] stays largely above the velocities where a phase separation occurs and seems even to imply that the mixture stays perfectly homogeneous − as the flow is always P-Ho for $U_m > U^G_{min}$ in the present experiments.

The main lack of this type of formula, based on the Froude number, remains that it does not take into account the ice particle size or its concentration (two major parameters of influence), and so it may be inaccurate in many cases. Otherwise, the phase separation principally occurs within regime St #1, see the previous section 3.2.1 for an exact description. For two cases, $\Phi_m = 5.3\%$ and $\Phi_m = 9.2\%$, it occurs when passing from St #1 to St #2 and for a last one, $\Phi_m = 12.3\%$, from St #1 to An (annular regime always implies a phase separation as long as the compact ice column does not take the whole pipe cross-section).

Albeit, it might be relevant to report straightly to the Froude number Fr:

$$Fr = U_m^2/(gD|1 - s|) \tag{3.4}$$

as it was used to characterize pattern transitions by [Stutz and Reghem, 2001; Stutz *et al.*, 2001]. The authors established that:
− $Fr > 15$: heterogeneous flow
− $0.2 > Fr > 15$: moving bed flow
− $Fr < 0.2$: stationary bed flow

Interestingly, values of $Fr > 15$ seem to correspond, in the study [Hirochi *et al.*, 2004], to the area where the excess pressure loss coefficient ϵ reaches 0, where $\epsilon = (\Delta P_{is} -$

$\Delta P_l)/(\phi \Delta P_l)$. Presently, the Froude number Fr only varies with the flow velocity U_m, as the variation of s is totally negligible. Its values are shown in Tab. 3.2, and all of them are comprised between 0.2 and 15 except for the lowest flow velocity $U_m = 0.073\ m.s^{-1}$. The range $[0.2, 15]$ corresponds to a "flow with moving bed" according to [Stutz *et al.*, 2001] that they defined as involving a moving bed under which a heterogeneous mixture flows.

$U_m\ (m.s^{-1})$	Fr $(-)$	Flow pattern types
0.58	9.3	Ho
0.51	7.2	Ho
0.44	5.4	Ho
0.36	3.6	St ; Ho
0.29	2.3	St
0.22	1.3	St
0.15	0.62	St
0.073	0.15	St ; An

Table 3.2 Froude number Fr for each flow velocity U_m. Ho refers to a homogeneous flow, St to a stratified flow and An to an annular flow.

Here, although the flow patterns are a little different from the expected ones, some similar elements appear:

(i) $Fr < 0.2$ is supposed to implies "stationary bed flow" according to [Stutz and Reghem, 2001; Stutz *et al.*, 2001]. This is not observed in the present case but, for $U_m = 0.073\ m.s^{-1} \Leftrightarrow Fr = 0.15\ (< 0.2)$, there is a major pattern change in most of the cases (each of them, except $\Phi_m = 2.1\%$) yielding very "compact" final patterns: St #1 $\longrightarrow$ An, for $\Phi_m > 10\%$, and St #1/2 $\longrightarrow$ St #3, for $\Phi_m < 10\%$.

(ii) Without talking about the fact that, for $15 > Fr > 0.2$, stratified flows (according to the present definition of "stratified" in section 3.2.1) emerged instead of pure "moving bed flows" (according to [Stutz *et al.*, 2001]'s definition), this range of Froude numbers also leads to homogeneous flows presently. Experimentally, $Fr = 5 - 6$ corresponds here to $U_m \sim 0.44\ m.s^{-1}$, which marks the transition zone from *stratified* St to *homogeneous* Ho (see Fig. 3.9 or Tab. 3.2). The critical Froude number $Fr = 5 - 6$ could preferably be used to define this pattern transition.

3.3 Pressure drops and friction factor in a straight pipe

3.3.1 Pressure drops in a horizontal straight pipe

In this section, it is attempted to interpret some pressure drop evolutions from the flow pattern observation or reversely. Figure 3.10 displays the variations of the pressure drop as a function of both the inlet mean velocity U_m and the ice fraction Φ_m. As expected, it increases with increasing values of Φ_m and U_m.

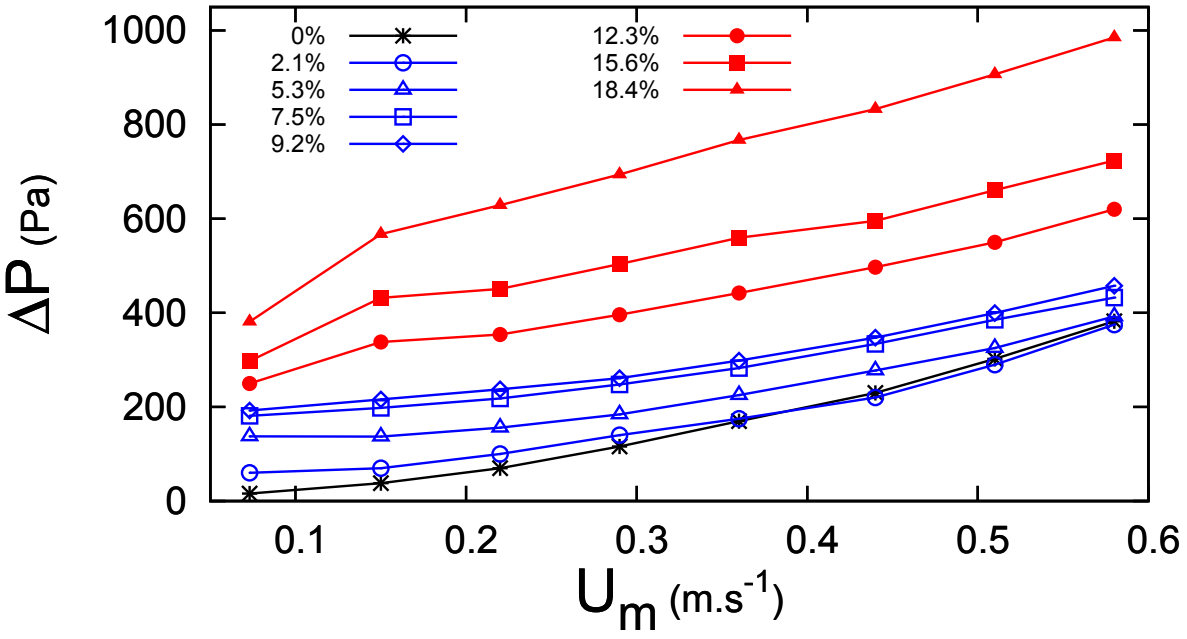

Figure 3.10 Pressure drop ΔP as a function of the mean flow velocity U_m for each inlet ice volume fraction Φ_m

in Fig. 3.10, it seems that the flows whose initial ice volume fraction Φ_m is lower than 10% (blue curves) behave quite differently from the ones with higher initial ice contents (red curves), which confirms the former observations on the flow regimes. For the highest ice volume fractions, the observations have shown that the whole pipe cross-section is filled with ice particles in almost every case. The exception may occur for the lowest flow velocities $U_m = 0.073 - 0.15\ m.s^{-1}$ where a thin space filled with just pure liquid possibly remains. For $\Phi_m < 10\%$, the velocity decrease rapidly creates a lower zone filled with few ice particles and soon totally empty of particles. This is one of the major differences noticed between the two groups of ice fractions which could notably explain the differences in terms of pressure drop.

Quantitatively, one can see that the pressure drops are globally much higher for $\Phi_m > 12\%$ and vary much faster with the augmentation of the ice concentration. For instance, $\Delta P_{18.4\%} - \Delta P_{9.2\%} = 469$ Pa, whereas $\Delta P_{9.2\%} - \Delta P_{0\%} = 128$ Pa at $U_m = 0.36\ m.s^{-1}$. The half height compact layer which appears in the flow pattern St #1 tends to get thicker as the velocity decreases in the cases of higher initial ice volume fractions, almost always surrounded by flowing ice particles. This might highly reinforce the flow resistance and thus much larger pressure drops would be recorded.

At low velocity, particularly for $U_m = 0.073\ m.s^{-1}$, the pressure drop variation at $\Phi_m > 12\%$ is close to the one at $\Phi_m < 10\%$. Annular flow is observed for $\Phi_m > 12\%$ whereas it is stratified flow #3 (moving bed like) for $\Phi_m < 10\%$. In both types of flow, one compact stratum forms and gets progressively thicker as the ice volume fraction increases. The only great difference between An and St #3 is the portion of the pipe cross-section covered by the column. Moreover, the compact stratum flows very slowly and is, most of the time, only surrounded by pure liquid acting as a lubricant. Thus, the pressure drop variation would follow this progressive expansion of the ice column over the pipe cross-section.

For $\Phi_m > 12\%$, one can remark an important gap in terms of the pressure drop values between the two lowest velocities (i.e. 0.073 and 0.15 $m.s^{-1}$). After that, each curve evolves quite linearly, particularly for $\Phi_m = 18.4\%$. $\Delta P_{12.3\%}$ and $\Delta P_{15.6\%}$ seem to have parallel evolutions. Here, the link between the observed phenomenon and the pressure drop gap is very straight: there is a change of flow state, being initially totally compact (*An* regime in Fig. 3.9) and suddenly becoming stratified. This pressure drop difference would represent the energy necessary to trigger the motion or to break the compact ice column. The phenomenon is not observed for $\Phi_m < 10\%$ where always remains a large area in the pipe cross-section filled with pure liquid phase only. Such an area plays the role of a bypass for the fluid phase and the pressure drop transition is then smoother.

For the lower ice concentrations ($\Phi_m < 10\%$), the pressure drop aspects stay close to the one of pure liquid flowing (see black curve with $\Phi_m = 0\%$), though these are a little flattened as the ice concentration increases. Globally, the pressure drop raise is slightly accelerated when the flow velocity increases, as observed by [Hirochi *et al.*, 2004], even though the flow pattern may change. Within this group (the blue one in Fig. 3.10), the variations of the pressure drops between each ice concentration tend to be less elevated with increasing the flow velocity − becoming very close to each other towards 0.6 $m.s^{-1}$: $\Delta P_{9.2\%} - \Delta P_{2.1\%} = 82$ Pa.

[Ayel *et al.*, 2003] reported the conclusions of [Darby, 1986], who exhibited a minimum in pressure drop at the transition between the saltation flow and the heterogeneous one, followed by a constant increase of the pressure drop as the flow velocity raises. The saltation flow is defined by the authors as the clear separation of the two phases within the flow (similar to a pure moving/stationary bed). It would correspond to St #3. The flow pattern An can hardly be considered as a saltation regime as the "layer" looks more like a column, neither St #2 where too many distinct layers are implied even if phase separation often occurs within. Despite the fact that the curves do not show a pressure minimum at low velocity when the flow pattern changes, it stays very flat (see the blue curves for $\Phi_m < 10\%$) and sometimes occurrences close to the one described by [Darby, 1986] were even observed through the experiments. For instance, at $\Phi_m = 5.3\%$, $U_m = 0.073\ m.s^{-1}$, the flow pattern is St #3 (a thick moving bed slides on the top) with $\Delta P \sim 130Pa$. Then, the raise of flow velocity (towards $U_m = 0.15\ m.s^{-1}$) leads to the transition to pattern St #2. Albeit, it can have slightly different features: (i) if a thin moving bed remains along top wall, the pressure drop remains almost unchanged ($\Delta P \sim 130$ Pa) whereas (ii) if this last has been replaced by a sheared one it is possible to see a slight pressure drop reduction of 15 Pa (then $\Delta P \sim 115$ Pa). This example clearly illustrates the specific sensibility between pressure drops and flow pattern evolution.

in Fig. 3.11, one may find again some of the previous observations. This time, the pressure drops are expressed as a function of the inlet ice volume fraction flowing along the pipe.

After $\Phi_m = 7\%$, the respective evolutions of the pressure drops are quite close, except for the lowest velocity tested $U_m = 0.073\ m.s^{-1}$. Although a gradation exists between the pressure drop values, the various encountered patterns do not seem to have a relevant impact on the way that ΔP evolves in terms of Φ_m.
Between $\Phi_m = 7.5\%$ and 9.2%, very little pressure drop augmentation is noticed at any flow velocity before a sharp rise as Φ_m increases. On the flow pattern map (Fig. 3.9), between these two ice volume fraction values, there is a sort of uncertainty stripe: i.e. for $U_m = 0.44\ m.s^{-1}$, whereas the flow becomes D-Ho when Φ_m decreases, it gets back to P-Ho between the two aforementioned Φ_m values. In the same way, for $U_m = 0.22\ m.s^{-1}$, whereas the flow becomes St #2 at $\Phi_m = 9.2\%$, it punctually gets back to St #1 at $\Phi_m = 7.5\%$. It occurs as if the flow tends to re-homogenise around a critical ice volume fraction value, being $\Phi_m \sim 7 - 9\%$. As the ice fraction decreases, there could be a threshold value or a balancing ice volume fraction for which the decreasing intensity of particle-particle interactions would strongly coexist with the growing intensity of liquid-

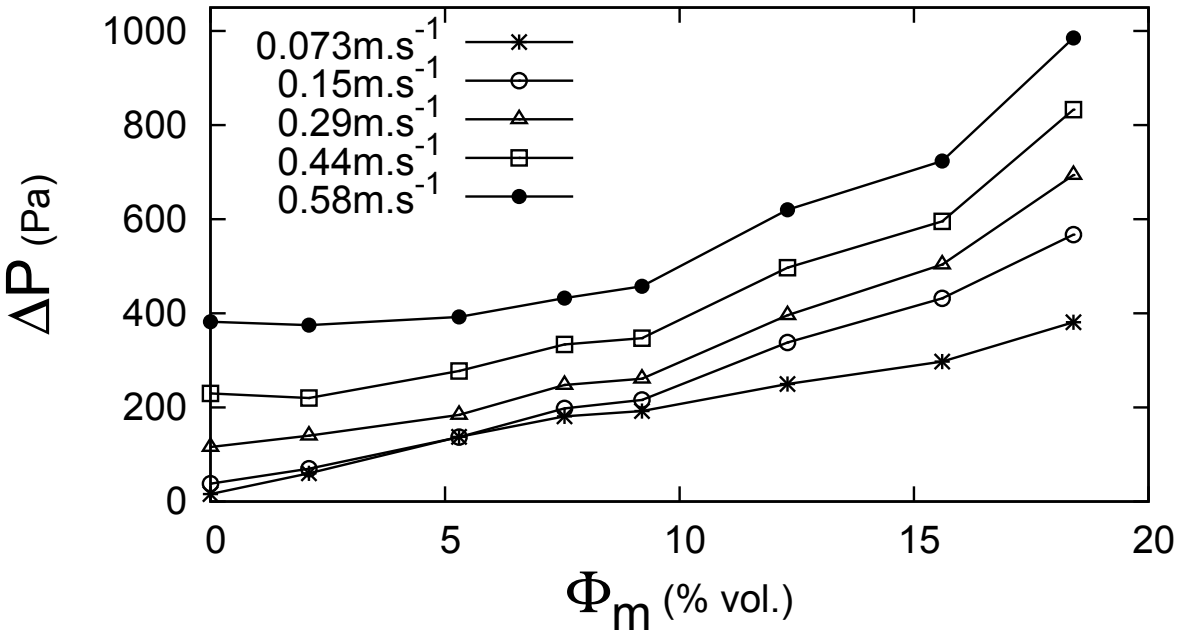

Figure 3.11 Pressure drop ΔP as a function of the inlet ice volume fraction Φ_m for five inlet flow velocities U_m.

particle interactions, having a singular repercussion on the particle dispersion as well as on the pressure drop. However, it was also shown that generally flows with higher ice volume fractions ($\Phi_m > 10 - 12\%$) behave quite differently from flows with lower ice volume fractions.

3.3.2 Friction factor correlations

In this section, the Darcy friction factors Cf is evaluated here from the present pressure drop ΔP measurements and compared to the ones obtained from three semi-empirical correlations. The friction factor values are given in Figure 3.12 as a function of the flow velocity U_m. The correlation of [Reghem, 2002] is extracted from [Turian *et al.*, 1971]'s work. A new set of coefficients was derived from his experimental data and it gives the friction factor Cf_R as a function of Φ_m, f_l and Fr as shown on Eq. 3.5:

$$Cf_R = Cf_l + 9330\Phi_m^{2.07} \times Cf_l^{1.963} \times Fr^{-0.627} \tag{3.5}$$

where Cf_l is the Darcy friction factor for the liquid phase and Fr the Froude number. The mean uncertainty on the friction factor is around 11%. The experiments were conducted in pipes of respective diameters 44.6 mm and 21.5 mm − which is close to the present one (here $D = 38.23$ mm) − for an ice content varying from 0% to 30% in volume and

initial flow velocities from 0.1 to 3 $m.s^{-1}$. The ice slurry was made from an initial aqueous solution of 10%-ethanol in mass. Unlike the two next models, this one had not been built on a rheological perspective − that does not account for the two-phase character of ice slurries nor for the flow regime (laminar/turbulent) for instance.

[Mellari, 2016] developed her own correlation from a rheological Herschel-Bulkley model, using generalized Reynolds number Re_{MR} defined by [Metzner and Reed, 1955] based on her experimental flow index n and consistency coefficient k. Her friction factor Cf_M is only valid for laminar flows and is expressed as follows:

$$Cf_M = \frac{64}{Re_{MR}} \tag{3.6}$$

$$\text{where} \quad Re_{MR} = \frac{U_m^{(2-n)} D^n \rho_{is}}{k} \frac{1}{8^{(n-1)} \left(\frac{1+3n}{4n}\right)}$$

In her experimental study, the ice slurry was made from a monopropylene glycol solution with a mass concentration between 5% and 24%. The pipe diameter was 25.4 mm, the flow velocities ranged from 0.25 to 1.2 $m.s^{-1}$ and the ice mass fraction from 0% to 25%.

The correlation Cf_O developed by [Onokoko *et al.*, 2017] was obtained by considering the ice slurry as a Bingham fluid. The yield stress τ_0 and Bingham viscosity μ_B were determined from experimental data (both function of the ice volume fraction Φ_m) and coupled with the Danish-Kumar laminar correlation (see [Danish *et al.*, 2011]):

$$Cf_O = 4 \times K_1 \left(1 - \frac{10K_2^4}{(K_1^4 + 3K_2)^4} + \frac{6K_2^3}{(K_1^4 + 3K_2)^3} + \frac{K_2}{(K_1^4 + 3K_2)}\right) \tag{3.7}$$

$$\text{where} \quad K_1 = \frac{16}{Re_B} + \frac{16He}{Re_B^2}, \quad K_2 = -\frac{16He^4}{3Re_B^8}$$

where $Re_B = \rho_{is} U_m D/\mu_B$ is the Bingham Reynolds number and $He = \tau_0 \rho_{is} D^2/\mu_B^2$ is the Hedström number. It introduces also a critical Reynolds Re_c drawn from [Swamee and Aggarwal, 2011]'s study and valid for $1 \leq He \leq 10^8$:

$$Re_c = 2100 \left(1 + \frac{He}{3600}\right)^{0.35} \tag{3.8}$$

It covers the transitional regime between laminar and turbulent flows for Bingham fluids. Their experiments were conducted in a pipe of $D = 0.017$ m in diameter and an ice slurry made from a monopropylene glycol solution of 4.6% initial mass concentration. The ice fraction was varied from 5% to 20% in mass and the flow velocity from 0.074 to 2.81 $m.s^{-1}$.

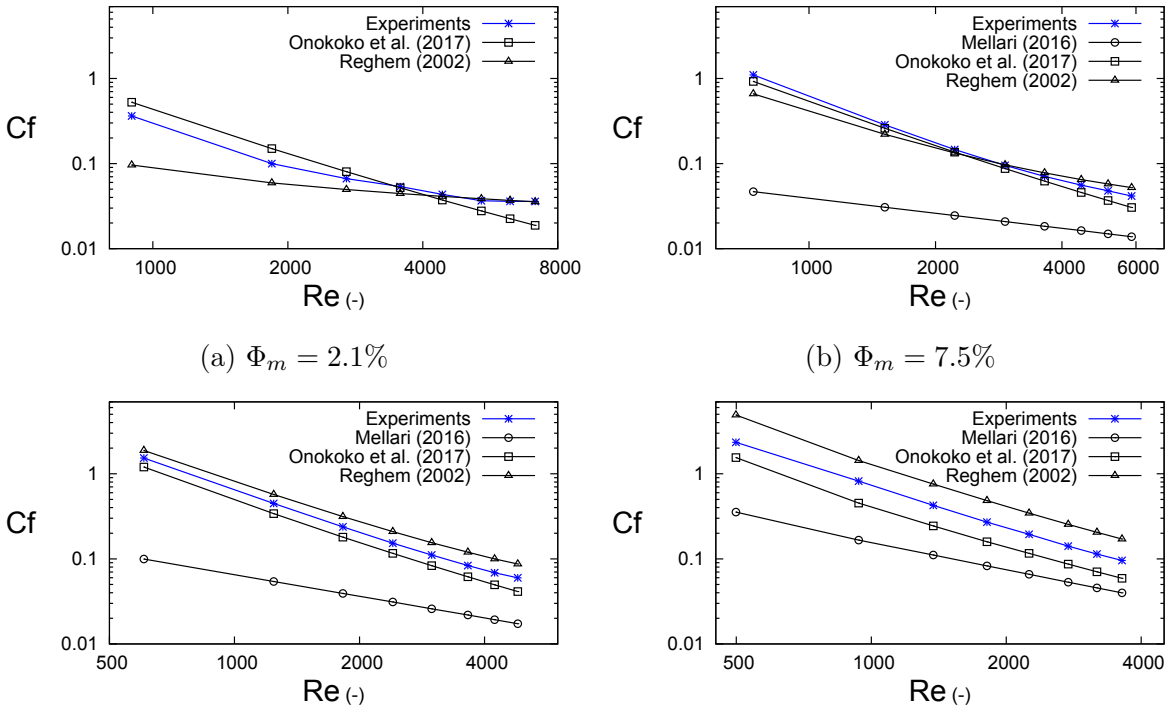

(a) $\Phi_m = 2.1\%$ (b) $\Phi_m = 7.5\%$

(c) $\Phi_m = 12.3\%$ (d) $\Phi_m = 18.4\%$

Figure 3.12 Comparison of the calculated and measured friction factors Cf as a function of the Reynolds number Re for various inlet ice volume fractions Φ_m

In Figure 3.12, one may notice that [Mellari, 2016]'s correlation largely underestimates the present experimental results for each case shown, as well as it underestimates the values given by the two other friction factor correlations. Her correlation was built from ice slurries made from the same additive as presently (monopropylene glycol) but flowing in a smaller pipe of diameter $D = 0.0254$ m. This represents the two thirds of the diameter of the present pipe. The influence of such a dimensional parameter on the rheological behaviour of the flow is non-negligible, especially since stratification phenomena are observed. Otherwise, her model was developed for laminar flows. It will be seen (in next section 3.3.3) that, for low Φ_m and higher U_m, the flow tends to be turbulent. Even if the correlation's results remain much lower than present experimental ones, they get closer as ice concentration Φ_m increases. The reasons could be a lower flow agitation and a better flow homogenisation rendering the rheological model more relevant. For $\Phi_m = 18.4\%$, the pipe cross-section is entirely filled by ice particles for almost all inlet velocities U_m consid-

ered. Again, this illustrates the influence of the flow pattern (stratified flow presently) on the friction coefficient.

The two other correlations, respectively developed by [Reghem, 2002] and [Onokoko *et al.*, 2017], frame quite closely the experimental results. The first tends to overestimate and the second stays below, except at lower Φ_m and U_m (Figs. 3.12a and 3.12b). The two correlations cross each other around $Re = 4000$ for $\Phi_m = 2.1\%$ and a little above $Re = 2000$ for $\Phi_{=}7.5\%$, points also crossed by the experimental results curiously. Interestingly, for the two aforementioned ice volume fractions, the correlation proposed by [Onokoko *et al.*, 2017] seems to better reproduce the experimental friction factor below the "cross point" whereas the one of [Reghem, 2002] gets closer above. It is worth mentioning that [Onokoko *et al.*, 2017]'s correlations was originally built for laminar flows (see the discussion in section 3.3.3).

3.3.3 Turbulence issues

In this section, it is attempted to discuss whether one can objectively identify an ice slurry flow as being turbulent or not from quantitative parameters. Despite the fact that several authors got interested to the turbulence nature of ice slurry flows, this issue still remains very complex and no general reliable criterion exists so far. Throughout the experiments, it has been observed that, beyond a certain level of flow velocity ($U_m > 0.4/0.5\ m.s^{-1}$), the mixture seems always very agitated and keeps its full homogeneity. For lower velocities, even if a compact stratum has formed, one may see vortices or recirculations appear locally. Albeit, it does not imply necessarily that the flow is turbulent.

Transition

In Figure 3.13, the friction factors C_f found experimentally are displayed as a function of the Reynolds number Re for all ice concentrations.

$$Re = \frac{\rho_{is} U_m D}{\mu_{is}} \tag{3.9}$$

This Reynolds number, corresponding to the classical one, is here calculated for the mean values of the mixture flow. As mentioned in section 3.1.2, the ice slurry properties, such as the viscosity μ_l and density ρ_l for the liquid phase, are given by the correlations found in the Handbook [Ashrae *et al.*, 2013] for 9.5 wt.% of initial mono-propylene glycol concentration. Concerning the calculation of the ice slurry mixture viscosity, it is done through [Brouwers, 2010]'s correlation (presented in Eq. 4.4 afterwards) where the viscosity formulation is

independent from the shear rate and the shear stress (Newtonian behaviour assumed). Thus, such a Reynolds number Re is chosen for two reasons : (i) it is coherent with the Newtonian modelling utilised to obtain the mixture viscosity and (ii) it remains a global estimation of the bulk flow regime: its physical meaning and value are purely indicative.

It is compared to the classical Darcy and Blasius correlations for laminar and turbulent pipe flows, respectively. The friction factors evaluated by the Darcy Cf_D and Blasius Cf_B are expressed as:

$$Cf_D = \frac{64}{Re} \tag{3.10}$$

$$Cf_B = \frac{0.316}{Re^{0.25}} \tag{3.11}$$

Usually, the transition between the two regimes occurs for $2000 < Re < 3000$ for a single-phase Newtonian fluid flow in a cylindrical pipe (even if it may strongly depend on the rugosity of the pipe walls). Here, one can notice that, except for $\Phi_m = 0\%$, none of the friction factor values gets close to the Darcy curve. They remain much higher and even seem to tend to another curve (green curve) as the ice volume fraction increases. This asymptotic curve could be described by $Cf(Re) \simeq e^{10.784} \times Re^{-1.617}$. For the lowest values of ice volume fraction, i.e. $\Phi_m < 7.5\%$, the Blasius curve is reached at certain higher Reynolds numbers denoted Re_t. For $\Phi_m = 2.1\%$, $Re_t \sim 4400$ and for $\Phi_m = 5.3\%$, $Re_t \sim 5500$. For the respective last values of $\Phi_m = 7.5\%$ and $\Phi_m = 9.2\%$, towards $Re_t = 6500$, the C_f values get very close to the blue curve. This would indicate that turbulent flow is reached and here Re_t would be the transition Reynolds number for the various Φ_m (similar to the critical Reynolds number Re_c). It confirms qualitatively the former results of [Grozdek *et al.*, 2009], who observed that Re_t increases with increasing values of Φ_m. Then, with their largest pipe diameters and in the laminar range ($Re < 2000$), the authors found important discrepancies between their experimental friction factors and the Darcy correlation (for Poiseuille flows) being even more marked as Re decreases. The authors attributed that to the appearance of heterogeneous (non-uniform or stratified) flows in larger pipe diameters, which influences the flow dynamics and thus the resistance properties over the pipe cross-section. This explanation is not valid as pure homogeneous flows are observed on a wide velocity range for high ice fractions corresponding to friction factors aligned on the green curve of Figure 3.13.

Strangely, the pattern tendency around the Re_t values seems the opposite of what could be expected in terms of Re evolution. For $\Phi_m = 2.1\%$, the regime appears purely homogeneous for the highest value of the flow velocity only (Fig. 3.9), and yet shows little

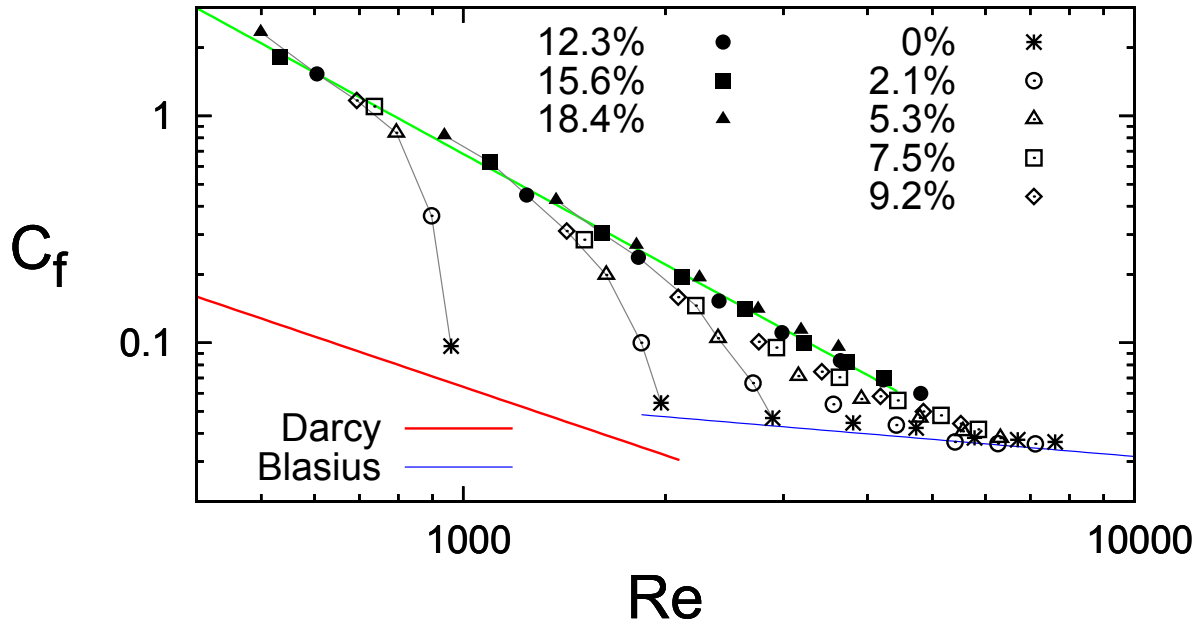

Figure 3.13 Friction factor C_f as a function of Reynolds number Re for each ice volume fraction Φ_m. The thick red line represents Cf_D and the thin blue one Cf_B. Grey lines correspond to the iso-velocities $U_m = 0.073,\ 0.15,\ 0.22\ m.s^{-1}$ from left to right.

shearing at middle pipe height for the two next values of flow velocity (i.e. 0.51 and 0.44 $m.s^{-1}$). Then, as Φ_m value gets higher, pure homogeneous flow tends to last longer when decreasing U_m whereas the friction factor values are less and less close to the Blasius curve (Fig. 3.13). Dispersion of the ice particles due seem mainly due to direct particle-particle interactions more than due to the flow motion or agitation.

One could ask if the bulk Reynolds number Re used for single-phase Newtonian fluids is the most relevant parameter to describe the transition from laminar to turbulent ice slurry flows in pipes and so if all the experimental data could collapse into a single curve at low velocities by plotting Cf against a more relevant definition of the Reynolds number. [Kumano *et al.*, 2010, 2013] used the Metzner-Reed (according to [Metzner and Reed, 1955]) generalized Reynolds number Re_{MR} calculated with their own rheological parameters k and n (Ostwald-de Waele model). They found that Re_{MR} decreases with increasing the ice fraction when the flow is supposed to be laminar. The same fact is noticed in the present study with the "original" Re number (Fig. 3.13). The transition to turbulence is observed in their case for $Re_{MR} \simeq 2000$ ($Re_{MR}/Re \simeq 0.5$). In the present experiments, the transition is always observed for much higher values of Re_{MR} such that this Reynolds number does not appear the most relevant parameter. [Niezgoda-Želasko and Zalewski,

2006b] and [Grozdek *et al.*, 2009] observed friction factor local minima when varying Re and used this observation to delimit the flow regimes. The phenomenon has not presently been noticed. A hypothesis to explain this absence could be the pipe diameter D: for [Niezgoda-Żelasko and Zalewski, 2006b], $0.01 \leq D \leq 0.02$ m and for [Grozdek *et al.*, 2009], $0.009 \leq D \leq 0.025$ m, which are quite smaller compared to the present one: $D = 0.03823$ m. Smaller pipe diameters could prevent stratification phenomena. Moreover, in the case of [Grozdek *et al.*, 2009] where D is the largest, the friction factor minimum is no longer visible (except at $\Phi_m = 0\%$). In further research works, it could be of interest to establish a link between the observation of a C_f minimum and the pipe diameter.

Laminarisation

Laminarisation occurs when the ice concentration Φ_m is increased above a certain level within the flow for a given inlet velocity U_m. Figure 3.14 exhibits the transition from turbulent to laminar for several given flow velocities U_m with the augmentation of the ice concentration Φ_m. The values of the critical Reynolds number Re_t obtained previously from the distributions of the friction factor are used to rebuild the flow pattern map and inform whether, for a given flow pattern, the flow is laminar or turbulent. Figure 3.14 displays the transition from laminar to turbulent regimes for stratified and homogeneous flow patterns as a function of the inlet velocity U_m and ice fraction Φ_m. As expected, the transition is delayed when the ice fraction increases confirming the results of [Niezgoda-Żelasko and Zalewski, 2006b].

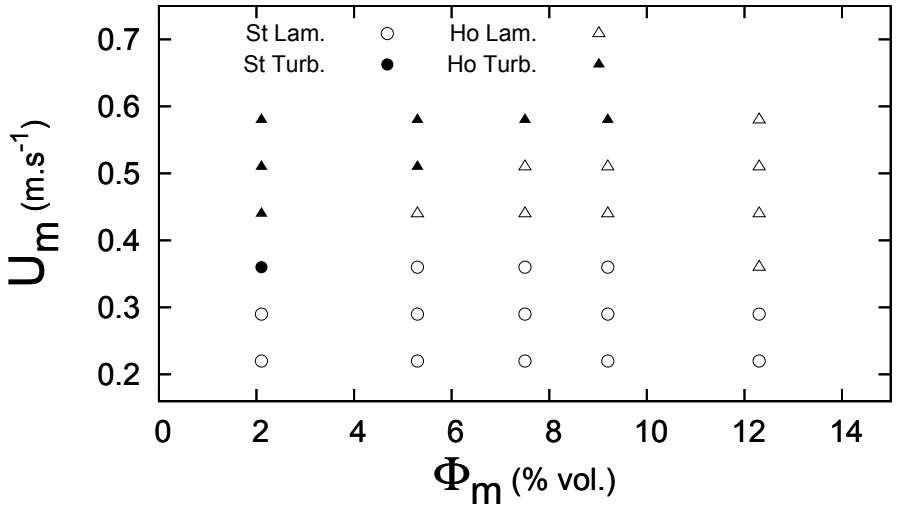

Figure 3.14 Evolution of both flow pattern and flow regime as a function of the inlet flow velocity U_m and ice volume fraction Φ_m. St $\rightarrow$ stratified and Ho $\rightarrow$ homogeneous, with their respective flow regimes.

It seems that there are two ways to visualise the phenomenon and its effects. The first way is that when ice concentration raises, the critical Re_c is moved towards higher values according to the work of [Niezgoda-Želasko and Zalewski, 2006b]. For these authors, Re_c corresponds to a minimum of C_f expressed as function of the Bingham Reynolds number Re_B, minimum which marks the transition between the laminar and turbulent regimes. Such a lag tends towards higher Re_B and would demonstrate that the flow remains laminar over velocity values U_m where it was supposed to be turbulent with no or few ice particles inside. As the present experimental data did not show minima with the C_f values, no real conclusion can be drawn about this point. Anyhow, one can see in Figure 3.13 that the higher Φ_m is, the later C_f values reach the Blasius curve.

Nota: the reason for such a phenomenon would be the interaction between ice particles and fluid phase that dissipates an important part of the kinetic energy. Nevertheless, one must remain careful with this issue as sometimes solid particles may rather reinforce kinetic energy within the flow − mainly depending on their size. [Niezgoda-Želasko and Zalewski, 2006b] noticed that bigger ice particles, in lesser concentration ($< 10\%$ in mass), may induce a phase segregation and thus may augment the turbulence or trigger it earlier. This observation is made here with $U_m = 0.36\ m.s^{-1}$ (see the points in Fig. 3.14 comprised between 0.3 and 0.4 $m.s^{-1}$), laminarisation occurs from $\Phi_m = 2.1\%$ to $\Phi_m = 5.3\%$ over an area where a phase separation is noticed. When the flow velocity is higher, the flow tends to be more homogeneous and thus laminarisation is delayed (see the points for $U_m \sim 0.6$ $m.s^{-1}$).

The second way is to look at the evolution of the pressure drop ΔP as a function of the ice concentration Φ_m. [Kumano *et al.*, 2013] defined a critical ice fraction Φ_{crit} for which the flow regime changes. The value of Φ_{crit} corresponds to a minimum for the pressure drops (when varying Φ_m and maintaining a constant Re_{MR}), recalling the observations of [Niezgoda-Želasko and Zalewski, 2006b]. The latter have already exhibited a transition from turbulent to laminar flow at constant U_m with raising Φ_m when a local minimum of the pressure drop was reached. This was valid only beyond a certain mean flow velocity U_m, the flow remaining always laminar below. in Figure 3.11, even though it is less pronounced than in the mentioned studies, one can see that curves flatten for lower ice concentrations and at higher velocities, i.e. $U_m > 0.4\ m.s^{-1}$, and they also show slight minima. A larger range of mean flow velocities U_m would have probably been required to clearly observe such minima. The study of [Niezgoda-Želasko and Zalewski, 2006b] very well shows that the higher the flow velocity is, the more the pressure drop minima are pronounced and transposed towards higher Φ_m.

3.4 Pressure drops in elbows and T-junctions: discussion

So far, few experimental research works [Kawada *et al.*, 1996; Mika, 2013; Niezgoda-Żelasko and Żelasko, 2014; Nørgaard *et al.*, 2005; Rached *et al.*, 2007; Reghem, 2002] were specifically interested in the behaviour of ice slurry flows through bends or T-junctions. Two of them developed their own correlations in order to calculate the local loss coefficients: [Niezgoda-Żelasko and Żelasko, 2014] for pipe bends and [Mika, 2013] for T-junctions. Although the objective sought here is rather informative, it appears important to keep carrying some research and bring out more elements of understanding of ice slurry flows through such singularities. Thus, this part aims principally at giving a global insight on ice slurry flows in elbows and T-junctions in the perspective to relate the flow regimes to the pressure drop variations.

Three configurations have been considered: I, II and III. Looking at Fig. 3.2b, I corresponds to BV1 open and BV2 closed ; II corresponds to BV1 closed and BV2 open ; III corresponds to both BV1 and BV2 open. For each one of the configurations, four mean inlet ice volume fractions Φ_m are studied: 0%, 5.1%, 12.2% and 18.0%, with the previous eight mean inlet velocities U_m. The flow pattern type entering this elbowed/deviation part can still be observed through the visualisation area. The bend diameter of the elbows is equal to 52 mm.

In Fig. 3.15, the pressure drops ΔP have been displayed as a function of the inlet flow velocity U_m. Globally, configuration III gives the lowest pressure drops, which is understandable since the flow can take two separate branches having the same diameter compared to the straight pipe. Then, slightly more elevated, come the pressure drop values of configuration I. In this configuration, the ice slurry is only deviated by one elbow, otherwise it progresses straightly: horizontally and then vertically. The principal difference occurs with configuration II where the values are much higher. There, the fluid mixture undergoes three deviations − two through T-junctions and one through an elbow.

For the two lowest ice contents and no ice at all ($\Phi_m = 0\%, 5.1\%, 12.2\%$), the pressure drop behaviour is quite similar in each configuration and is also similar to the one observed in Fig. 3.10, i.e. the parabolic shape with the slope increasing as the flow velocity increases too. Whereas, in the long straight pipe, flows with ice volume fractions superior to 12% exhibit close behaviour, here it does not seem the case any more. Moreover, the pressure

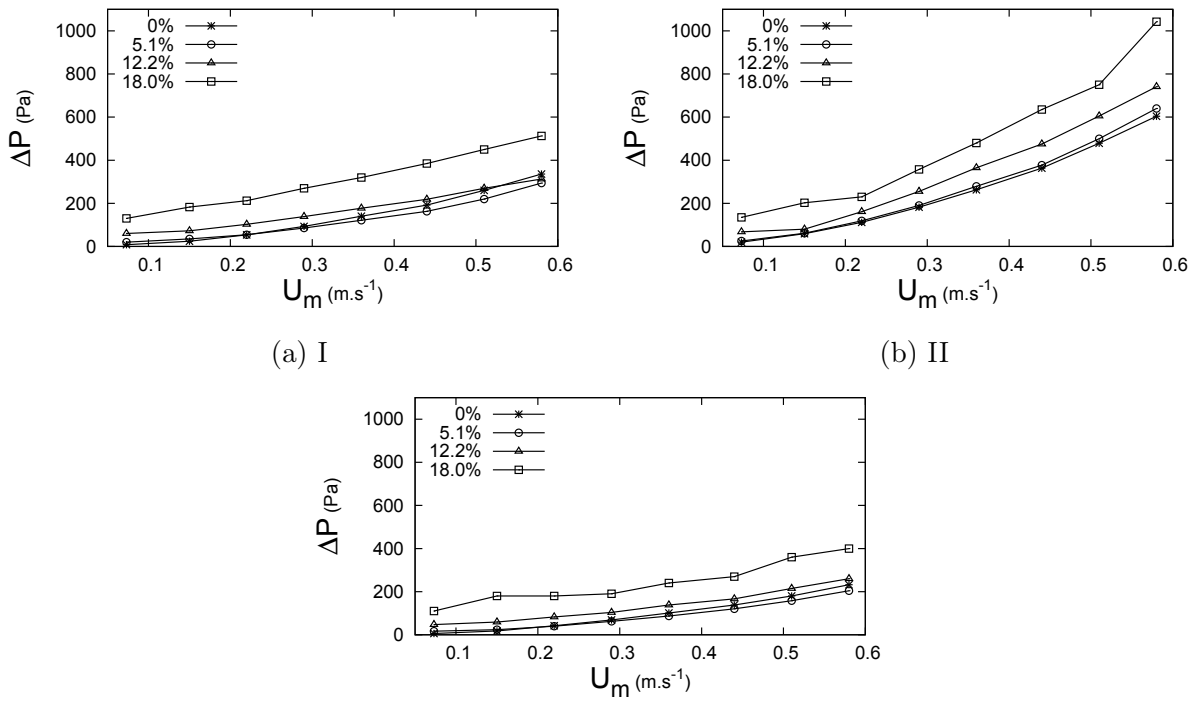

(a) I

(b) II

(c) III

Figure 3.15 Pressure drops ΔP measured between P1 and P2 as a function of the mean flow velocity U_m for 4 ice fractions and the 3 configurations I, II and III.

drop values for $\Phi_m = 12.2\%$ stays close to the ones obtained for the low ice content flow ($\Phi_m = 5.1\%$). This is quite hard to explain in terms of flow patterns as their observations − before entering the elbowed area − remain unchanged. Beyond $\Phi_m = 12\%$, the whole pipe cross-section is filled with ice particles except at the lowest tested velocity and a thick stratum tends to appear near the pipe middle height. Nevertheless, the various deviations could maintain a certain level of agitation within the flow at $\Phi_m = 12.2\%$, strong enough to prevent the reformation of large compact structures unlike the flow at $\Phi_m = 18.0\%$ for which the cohesive forces stay largely preponderant. Otherwise, only a very slight pressure drop augmentation is observed for $\Phi_m = 12.2\%$ in configuration II between $U_m = 0.073$ and 0.15 $m.s^{-1}$. For the lowest flow velocity ($U_m = 0.073 m.s^{-1}$), the flow pattern is purely annular. Thus, the energy required to pass three 90°-deviations must be elevated and one can think that the column-like flow remains through the two T-junctions and the elbow. However, at $U_m = 0.15$ $m.s^{-1}$, the flow rate is sufficiently high to break the compact ice column, explaining the flattening of the pressure drop from 0.073 to 0.15 $m.s^{-1}$. For ice fraction of 18%, Figure 3.15b shows a pressure drop flattening at higher velocities (between 0.15 and 0.22 $m.s^{-1}$), indicating that the column-like flow is retained at 0.15

$m.s^{-1}$. In fact, the pattern modification is lagged in velocity (relatively to the lower ice volume fraction $\Phi_m = 12.2\%$) since, at higher ice concentration levels, the ice particles are more compacted and thus more energy is required to break the compact coalescent column.

The highest ice content fluid ($\Phi_m = 18.0\%$) seems to behave completely independently, showing various differences from one configuration to another. Firstly, the pressure drop values in this case are much higher comparatively to the other cases − except for the configuration II where the pressure drops are much comparable. Secondly, the shapes of the three curves are rather different: in configuration I, the pressure drop increases quite linearly, which recalls the former results for the straight pipe. In configuration II, the pressure drop increase remains linear only between $U_m = 0.22$ and $0.51\ m.s^{-1}$ whereas the increase is small before and seems to become large afterwards. In configuration III, the variations are irregular: after a sharp increase at low velocities, the pressure drops get more constant for U_m between 0.15 to $0.29\ m.s^{-1}$ before increasing further at higher velocities. Interestingly, the velocity range $U_m = [0.15 - 0.29]\ m.s^{-1}$ corresponds to the flow pattern categorized as St #1 in Figure 3.9.

In configuration I particularly, the pressure drops for the pure liquid case overtake the ones of 5.1%-ice slurry flow at $U_m \sim 0.2\ m.s^{-1}$ and 12.2%-ice slurry flow at $U_m \sim 0.5\ m.s^{-1}$. The phenomenon appears again in configuration III, though this time the 0%-ice curve does not overtake the 12.2%-ice's one but still tends to get close. This tendency has already been observed for the straight pipe as shown in Figure 3.10. For [Niezgoda-Želasko and Želasko, 2014], this phenomenon tends to be less visible in the bends or in the elbows they studied, and disappear totally beyond an ice mass fraction of 10%. In the present case, the volume ice fraction of 12.2% corresponds to $\sim$ 11% mass − last value being located above the previous threshold. Moreover, the phenomenon seems here amplified compared to the pipe flow as the pipe pressure drops with $\Phi_m = 12.3\%$ stayed high above the ones of the 0%-ice flow without ever crossing each other. Nevertheless, the pressure drops presently are not strictly given for the elbow since a horizontal pipe and a vertical one (neglecting the T-junctions straightly passed) are also framed by the pressure probes. [Reghem, 2002] notably showed that there is a decrease of the pressure drops in vertical pipes for ice slurry flows (with friction coefficients inferior to 0), so that it could be the main factor explaining the important pressure drop reduction with $\Phi_m = 5.1\%$ and 12.2% relatively to $\Phi_m = 0\%$ here.

3.5 Brief summary

Three principal patterns were revealed: homogeneous, stratified and annular (or column). Stratified flow essentially means a flow made of several strata occurring with or without a phase separation. The existing transition criteria based on the critical deposition velocity or the Froude number cannot be used with confidence to predict the transition between two flow patterns for the present experimental conditions.

Pressure drops have been measured simultaneously to the flow visualisations with the objective to link the flow patterns to the pressure drop variations. In some cases, a flow pattern change does not have any impact on the pressure drop distribution. Albeit, as observed with the flow patterns, two groups of different ice volume fractions seem to emerge with a critical inlet ice fraction around $\Phi_m \simeq 10 - 12\%$. In terms of friction coefficient, all the measured values tend to collapse into a single curve at low bulk Reynolds numbers ($Re \leq 800$), then get very close to the Blasius correlation at higher Reynolds numbers, such that the flow is turbulent for $Re \geq 6000$ for all ice fractions. In between, the results depend highly on the inlet ice fraction. Laminarization phenomenon was confirmed and rather occurred for homogeneous flows.

Finally, the pressure drops were measured through three geometrical configurations including 90°-bends and T-junctions. They are found to be quite similar to those measured in the straight pipe for Φ_m up to 12.2%. On the contrary, for $\Phi_m = 18\%$, significantly higher pressure drops have been measured, leading to high pumping powers. Ice particles accumulate in the singularities at this ice fraction leading certainly to different flow patterns compared to those observed in the straight pipe case.

CHAPTER 4

NUMERICAL MODELLING OF SOLID-FLUID MIXTURE FLOWS

This part of the research project focuses on the development and the assessment of an advanced numerical model in order to investigate the dynamic behaviour of ice slurry flows under isothermal conditions. It is organised as follows: in Section 4.1, each model component is presented in detail as well as the main parameters of the numerical methodology. Then, in Section 4.2, simulations are run for different solid suspension flows and ice slurry flows, and the numerical results are validated against experimental data available in the literature. Finally, Section 4.3 presents a budget of the transport equation for the particle volume fraction to highlight the main mechanisms responsible for the particle distribution.

4.1 Mathematical and numerical methodologies

4.1.1 Model features

The present model assumes that the fluid is a single-phase and incompressible mixture with appropriate thermophysical properties. The flow is steady and isothermal and all particles are considered spherical with a constant diameter d. For the turbulent flow regimes, it will be seen in Chapter 5 that the SST $k-\omega$ model is generally preferred. Nevertheless, other turbulence models will be associated with the developed suspension flow model in order to compare and assess them.

Continuity and momentum equations

Under the previous assumptions, the conservation equations may be written as:

Continuity equation

$$\frac{\partial}{\partial x_i}(\rho_m u_i) = 0 \tag{4.1}$$

Momentum equation

$$\frac{\partial}{\partial x_i}(\rho_m u_i u_j) = -\frac{\partial p}{\partial x_j} + \frac{\partial \tau_{ij}}{\partial x_i} + \rho_m g \tag{4.2}$$

where g is the acceleration due to gravity and τ_{ij} represents the shear stress components expressed as:

$$\tau_{ij} = \mu_m \dot{\gamma}_{ij} \tag{4.3}$$

The equation proposed by [Brouwers, 2010] (Eq. 4.4) has been preferred to [Thomas, 1965]'s equation used by other authors, such as [Kitanovski and Poredoš, 2002; Onokoko and Galanis, 2013; Wang *et al.*, 2013b], to model the effective mixture viscosity μ_m. Equation 4.4 was formerly validated for particle volume fractions $\phi < 0.64$ and found to lead to better results at higher local ice fractions than the Thomas' formula (see [Blazejewski, 2012]).

$$\mu_m = \mu_l \left(\frac{1-\phi}{1 - 1.5625 \times \phi} \right)^{4.444} \tag{4.4}$$

In the present case, it is worth mentioning that the mixture viscosity μ_m corresponds to the effective suspension viscosity μ_{eff}. Finally, the mixture density is calculated by a mixing-type law as follows:

$$\rho_m = \phi \rho_s + (1-\phi)\rho_l \tag{4.5}$$

where ρ_s is the solid particle density or the ice density, and ρ_l is the liquid phase density. μ_l and ρ_l, depending on the aqueous solution, its initial additive concentration and its temperature, can be evaluated using the empirical correlations provided by [Ashrae *et al.*, 2013; Kauffeld *et al.*, 2005] for various aqueous solutions.

Particle volume fraction equation

[Phillips *et al.*, 1992]'s constitutive equation originally developed for concentrated suspensions has been chosen to model the transport of the particle concentration. It consists of a diffusion equation that accounts for the shear-induced particle migration. The equation governing the particle concentration field may be expressed as follows:

$$\frac{\partial}{\partial x_i}(\rho_m u_i \phi) = -\frac{\partial N_t}{\partial x_i} \tag{4.6}$$

Particle flux expressions used to obtain the diffusion equation (Eq. 4.6) were formerly derived by simple scaling arguments. [Bui and Rudman, 2003] showed that this model is also valid for turbulent flows. The analogy between ice slurry and solid suspension flows has been checked by several authors [Fang and Phan-Thien, 1995; Phillips *et al.*, 1992; Shauly *et al.*, 2000]. Equation 4.6 represents the balance between the convective and the diffusive particle fluxes. The term N_t is split into three terms : the flux N_c due to the

shear rate gradient (Eq. 4.7), the flux N_μ due to spatial viscosity variation (Eq. 4.8) and the flux N_s proposed by [Richardson and Zaki, 1954] due to the particle settling (Eq. 4.9). These three fluxes are expressed below:

$$N_c = -\rho_m K_c a^2 \phi \frac{\partial \dot{\gamma}\phi}{\partial x_i} \tag{4.7}$$

$$N_\mu = -\rho_m K_\mu a^2 \dot{\gamma} \phi^2 \frac{1}{\mu_m} \frac{\partial \mu_m}{\partial x_i} \tag{4.8}$$

$$N_s = \rho_m \omega_{s0} f(\phi) \phi \delta_{i3} \tag{4.9}$$

where $\dot{\gamma}$ represents the magnitude of the local shear rate tensor, $a = d/2$ is the particle radius and ω_{s0} is the terminal particle settling velocity. $K_c = 0.41$ and $K_\mu = 0.62$ are two dimensionless constants that were empirically determined by [Phillips *et al.*, 1992].

Originally, the particle volume fraction transport equation (Eq. 4.6) comprised three components, being a flux term accounting for the Brownian motion of the particles − and two other flux terms − (Eq. 4.7) and (Eq. 4.8) already mentioned − accounting for diffusion, either due to the spatial variations of the particle interaction frequency $\nabla(\phi\dot{\gamma})$ or due to the spatial variations of the effective viscosity $\nabla(\mu\phi)$. [Phillips *et al.*, 1992] discussed the possibility of neglecting the term $\nabla(\phi\dot{\gamma})$. In the context of ice slurry flows, all terms are conserved. The last flux term N_s accounts for the particle buoyancy and so possible stratification phenomenon. The terminal particle settling velocity ω_{s0} is calculated using Equation 4.10 proposed by [Zhiyao *et al.*, 2008]:

$$\omega_{s0} = \frac{d_*^3}{d} \nu \left[38.1 + 0.93 d_*^{\frac{12}{7}} \right]^{-\frac{7}{8}} \tag{4.10}$$

This equation is valid for Reynolds numbers $Re_s = \frac{\omega_{s0} d}{\nu} \leq 2 \times 10^5$. The dimensionless particle diameter d_* is defined by:

$$d_* = \left(\frac{g \Delta\rho}{\nu^2} \right)^{\frac{1}{3}} d \tag{4.11}$$

where $\Delta\rho = \rho_s/\rho_l - 1$ and $g = 9.81\ m.s^{-2}$.
The dumping function f derived from Gurel's formula (see in [Blazejewski, 2012]) is used to fit the mixture viscosity modelled by Equation 4.4:

$$f = \frac{(1-\phi)^2}{\mu_r} \tag{4.12}$$

where μ_r is the relative viscosity defined by $\mu_r = \mu_m/\mu_l$. Other damping, or hindrance, functions exist though. [Richardson and Zaki, 1954] proposed $f(\phi) = (1 - \phi/\phi_{max})(1 - \phi)^{\alpha-1}$ and [Kapoor and Acrivos, 1995] $f(\phi) = (1-\phi)/\mu_r$. The last must also be combined with a viscosity expression. Among the most used viscosity expressions, one finds the [Thomas, 1965]'s equation and the [Krieger and Dougherty, 1959]'s expression ($\mu_r = (1 - \phi/\phi_{max})^{-2}$). All these formulas are close in their expressions and leads to small differences for the hindered particle settling (see Figure 4.1).

index	mixture viscosity μ_m	hindrance function $f(\phi)$
I	–	[Richardson and Zaki, 1954], $\alpha = 2$
II	–	[Richardson and Zaki, 1954], $\alpha = 4$
III	[Thomas, 1965]	Gurel's formula
IV	[Krieger and Dougherty, 1959]	[Kapoor and Acrivos, 1995]
V	[Krieger and Dougherty, 1959]	Gurel's formula

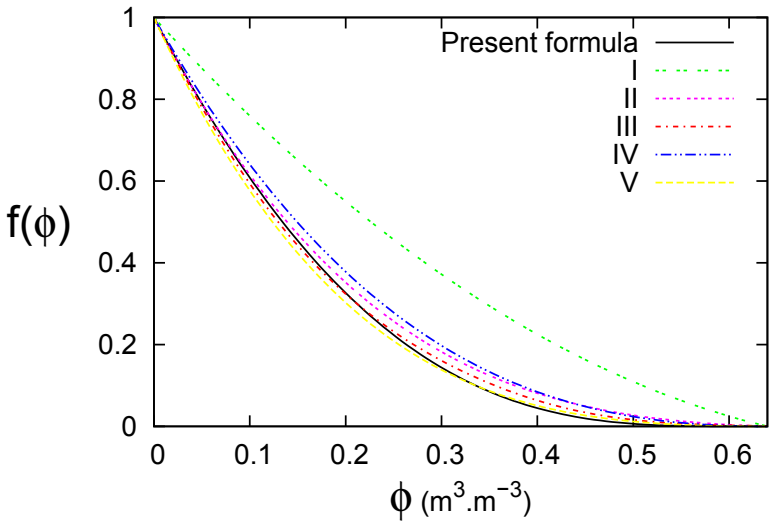

Figure 4.1 Hindrance functions from different formula combinations. α represents the exponent of [Richardson and Zaki, 1954]'s formula.

The function f proposed by [Revay and Higdon, 1992] and used by [Onokoko and Galanis, 2013] was found to lead here to unrealistic ice fraction along the upper pipe wall. Equation 4.4 allows to predict the viscosity of homogeneous suspensions having a volume fraction of solid particles going up locally to about 64%. Numerically, in addition to the dumping function f, the particle settling phenomenon is turned off when the particle volume fraction ϕ exceeds 0.64, corresponding to the maximum random packing proposed by [Brouwers, 2010]. Depending on the arrangement of the dispersed particles, the maximum packing factor ranges between 0.52 and 0.74 [Kauffeld *et al.*, 2005].

Turbulence modelling and particle dispersion

Four different turbulence closures will be compared for the first time, in Section 5.2, to assess the capability of turbulence models to predict isothermal ice slurry flows. This numerical benchmark includes the RNG $k-\varepsilon$, the $k-\omega$, the $k-\omega$ SST and the RSM (Reynolds Stress Model based on the specific dissipation rate ω). The mesh distributions used in the present work (see in Section 4.1.2) are thin enough to account for near-wall effects leading to low-Reynolds number modelling. The $k-\omega$ SST turbulence model [Menter, 1994] is a two-equation model using the $k-\varepsilon$ model in the core of the flow and switches to the $k-\omega$ model in the near-wall regions. The $k-\omega$ model is known to perform better than $k-\varepsilon$ models for boundary layer flows. Moreover, the $k-\omega$ SST model is less sensitive to boundary conditions, notably at the pipe inlet. Preliminary calculations have besides shown that the RNG $k-\varepsilon$ model fails to provide the right concentration profiles for solid suspension flows [Bordet *et al.*, 2016b] and ice slurry flows [Bordet *et al.*, 2016a]. For all these reasons, the $k-\omega$ SST model will be mainly used in the following.

For turbulent flows, a supplementary diffusion term $-\frac{\partial}{\partial x_i}(\Gamma_T \frac{\partial \phi}{\partial x_i})$ is added in the ϕ-transport equation (Eq. 4.6). Γ_T term is derived from stochastic Lagrangian models [Pope, 2000] and may be expressed for anisotropic turbulence as:

$$\Gamma_T = \overline{u_i' u_j'} T_L \tag{4.13}$$

where the term $\overline{u_i' u_j'}$ corresponds to the Reynolds stress tensor components − in the case of isotropic turbulence, $\overline{u_i'^2} = \frac{2k}{3}$ − and T_L to the Lagrangian integral time scale defined by:

$$T_L^{-1} = \frac{3}{4} C_0 \frac{\varepsilon}{k} \tag{4.14}$$

such as k and ε are the turbulence kinetic energy and the rate of dissipation of turbulence kinetic energy, respectively. As the SST $k-\omega$ model currently used carries the scale ω known as the specific dissipation rate instead of ε, then ε has to be evaluated through:

$$\varepsilon = \beta^* \omega k \tag{4.15}$$

with the constant $\beta^* = 0.09$ [Menter, 1994]. The Langevin-model constant C_0 introduced in Equation 4.14 is related to the Kolmogorov constant. Based on extrapolated direct numerical simulation data, [Pope, 1994] estimated the constant C_0 as being close to the value 6.2, which will be used in the present model.

4.1.2 Numerical considerations

The mathematical model has been implemented in a finite volume solver with second-order upwind for each transport equation. The interpolation method for the gradients'calculation is the Green-Gauss Cell-Based method. The pressure-velocity coupling is achieved using the SIMPLE algorithm.

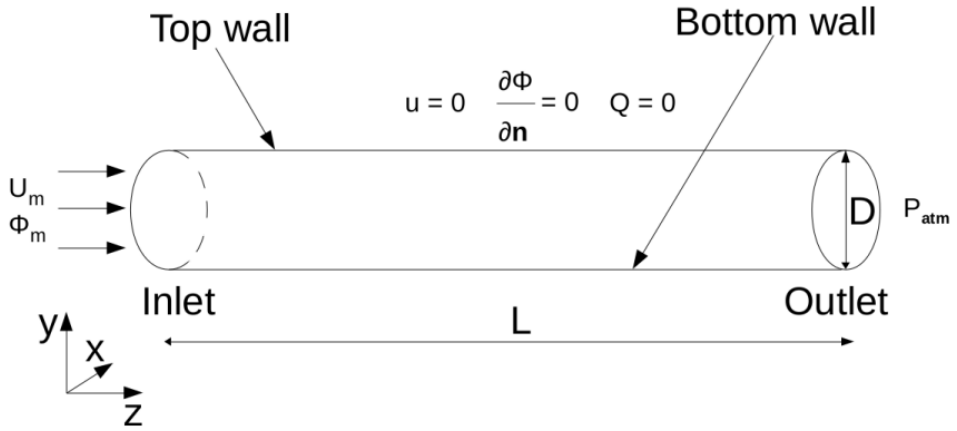

Figure 4.2 Schematic view of the pipe flow configurations with relevant notations and boundary conditions.

Constant velocity U_m and particle concentration Φ_m are specified at the tube inlet. Turbulence intensity is fixed to 5% at the inlet. It has been carefully checked that varying the turbulent intensity does not modify the hydrodynamic and concentration fields. No slip conditions are imposed at the walls with a Neumann boundary condition for the particle volume fraction. At the tube outlet, the pressure is fixed to the atmospheric pressure. All the boundary conditions are given in Figure 4.2.

All turbulence closures have been used in their low-Reynolds formulation. A mesh refinement is then required in the near-wall regions. To successfully capture the viscous sublayer, the wall coordinate y^+ $(= r^+)$ remains always lower than $y^+ \sim 1$. The mesh expansion rate is fixed to 1.1 until it reaches the log-law layer, that is to say around $y^+ = 30$. The mesh grid is composed of 1.3×10^6 cells with about 2000 cells per cross-section, with a cross-section every 2.5 mm. It has been carefully checked that this mesh arrangement provides grid-independent solutions. A sketch of the mesh grid is shown in Figure 4.3 for a given cross-section. All calculations were run on the supercomputer Mammouth Série MS2 using 16 processors. The typical CPU time is around 2.6 seconds per iteration using 16 cores and 14 hours are required to get statistically converged solutions.

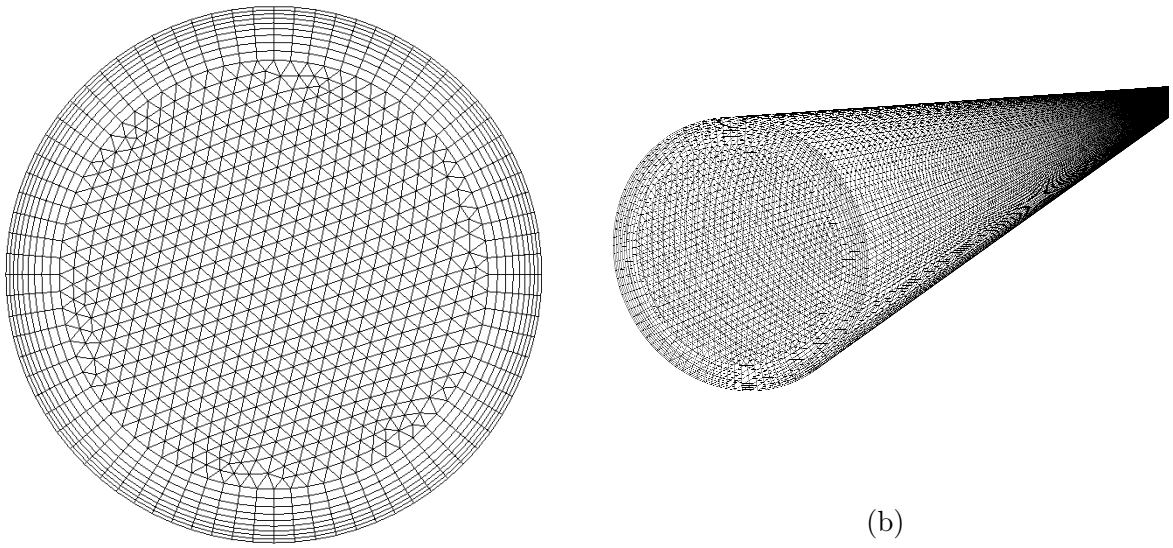

(a) (b)

Figure 4.3 (a) View of the mesh grid in a pipe cross-section. (b) 3D view of the pipe mesh.

4.2 Validation

Due to the complexity of performing local concentration measurements in insulated pipes, there is a lack of local and reliable experimental data for ice slurry flows. The present results are then compared to two other solid-liquid suspensions (cases I [Kaushal *et al.*, 2005] and II [Gillies *et al.*, 2004]) and to the velocity measurements of [Vuarnoz *et al.*, 2002] (case III, 11 wt% ethanol−water solution) and of [Stamatiou and Kawaji, 2005] (case IV, 6.2 wt% NaCl−water solution) for ice slurry flows. The characteristics of these four test cases are summarized in Table 4.1. Note that for the solid-liquid suspensions (Cases I and II), the mixture properties have been evaluated at $T = 20°\text{C}$. The mesh grids used for these three cases are similar to the one shown in Figure 4.3. The total numbers of cells are 2.4 millions (resp. 1.79) for cases I and II (resp. case III) with 2998 cells (resp. 2032) per cross-section. For case IV, the mesh is fully Cartesian, counts 3861 rectangular faces per cross-section and $1.2M$ rectangular hexahedron cells.

Case I corresponds to spherical glass spheres suspended in water. The numerical predictions are compared to the experimental data of [Kaushal *et al.*, 2005] and to the numerical simulations of [Wang *et al.*, 2013a] using a two-phase Euler-Euler model coupled to a $k-\varepsilon$ closure for three sets of parameters (Φ_m, d). On Figure 4.4a, the concentration profile varies slightly along the vertical pipe diameter ($0.09 < \phi < 0.12$) in the experiments. The present simulation agrees fairly well with the experiments, whereas the model of [Wang

	Case I [Kaushal *et al.*, 2005]	Case II [Gillies *et al.*, 2004]	Case III [Vuarnoz *et al.*, 2002]	Case IV [Stamatiou and Kawaji, 2005]
carrier fluid	water	water	water + $10wt.\%$ ethanol	water + $6.2wt.\%$ NaCl
particles	glass	sand	ice	ice
$d\ (\mu m)$	125 - 440	90	100	100
$D\ (m)$	0.0549	0.103	0.023	rectangular section 0.31×0.0254
$L\ (m)$	4.2	6	1.86	0.610
$\rho_s\ (kg.m^{-3})$	2470	1850	917	917
$\rho_l\ (kg.m^{-3})$	1000	1000	987	1042
$\mu_l\ (Pa.s)$	0.001	0.001	0.00503	0.0018
$\omega_{s0}\ (mm.s^{-1})$	8.3 - 53.3	2.637	0.0563	0.2783
$U_m\ (m.s^{-1})$	4	3	1.3	0.151
$\Phi_m\ (-)$	0.1-0.2	0.19	0.17	0.019
$Re = (\rho_m U_m D)/\mu_m$	$\geq$ 140 000	232 172	3656	3760

Table 4.1 Characteristics of the four solid-liquid suspensions.

et al., 2013a] predicts a higher concentration gradient within the pipe. In the present model, it may be attributed to the turbulent dispersion term, which counter-balances the sedimentation phenomenon ($\omega_{s0} = 8.3\ mm.s^{-1}$), leading to a more homogeneous concentration profile. The same behaviour is observed for the two other sets of parameters on Figures 4.4b and 4.4c. The simulations of [Wang *et al.*, 2013a] under-estimate the experimental values of ϕ close to the top wall ($y/D > 0.2$) and, by conservation, over-estimate them along the bottom wall ($y/D < 0.2$). Very close to the walls, the present model seems to perform better. It is noteworthy that the dispersion term better stabilizes the calculations.

Case II corresponds to the turbulent flows of sand-water suspensions in an isothermal straight pipe. For this case, [Gillies *et al.*, 2004] measured the velocity and concentration profiles for $U_m = 3\ m.s^{-1}$ and $\Phi_m = 0.19$. As for case I, due to the density of the particles, the concentration is higher along the bottom wall. Once again, the model of [Wang *et al.*, 2013a] leads to a more inhomogeneous concentration distribution along the pipe diameter as shown in Figure 4.5a. On the contrary, the present model predicts the right profile with $0.17 < \phi < 0.22$ and a nearly constant fraction of particles in the bulk flow. The two models predict the same mean axial velocity distribution corresponding to a classical turbulent Poiseuille profile. It means that the presence of particles does not modify too

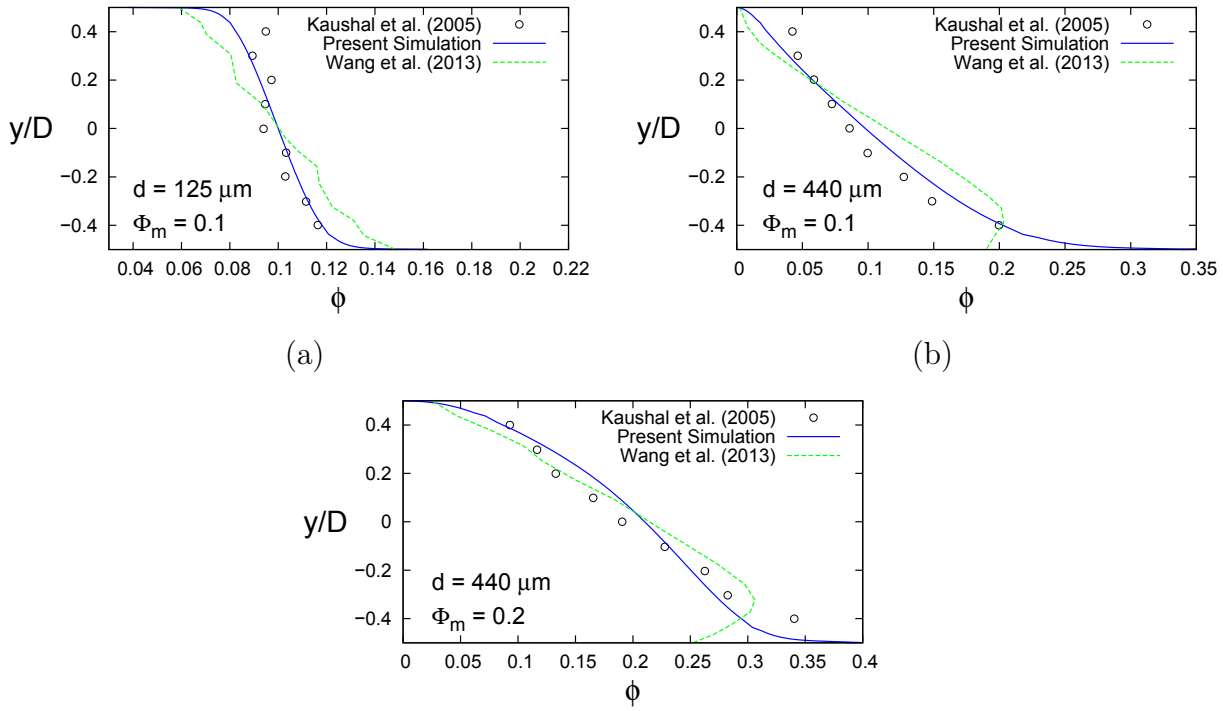

Figure 4.4 Radial distributions of the volume fraction of glass particles for $U_m = 4\ m.s^{-1}$ and: (a) ($\Phi_m = 0.1$, $d = 125\ \mu m$), (b) ($\Phi_m = 0.1$, $d = 440\ \mu m$) and (c) ($\Phi_m = 0.2$, $d = 440\ \mu m$). Comparisons between the present simulations, the experimental data of [Kaushal *et al.*, 2005] and the numerical simulations of [Wang *et al.*, 2013a].

much the mean velocity field. The particle concentration remains indeed around 0.2 for the whole pipe and the fluid dynamic viscosity varies then weakly.

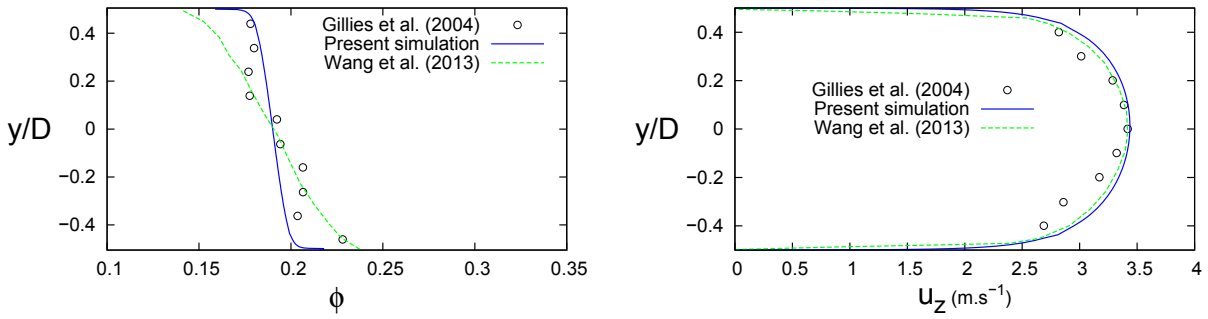

(a) (b)

Figure 4.5 Radial distributions of (a) the volume fraction of sand particles and (b) of the mean axial velocity for $U_m = 3\ m.s^{-1}$ and $\Phi_m = 0.19$. Comparisons between the present simulations, the experimental data of Gillies et *al.* [Gillies *et al.*, 2004] and the numerical simulations of [Wang *et al.*, 2013a].

The present model has also been compared to the velocity measurements of [Vuarnoz *et al.*, 2002] using ultrasonic Doppler velocimetry for ice slurry flows ($\Phi_m = 0.17$ and $U_m = 1.3\ m.s^{-1}$). For these conditions, the authors showed that the ice slurry may be considered as a Newtonian fluid. In these experiments, the mass concentration of ethanol was fixed to 10.3%. On Figure 4.6, it is shown that the present model including the turbulent dispersion term compares fairly well to the experimental data [Vuarnoz *et al.*, 2002]. It improves the predictions of the two more complex models of [Wang *et al.*, 2013a] and [Zhang and Shi, 2015], which respectively tend to over-estimate and under-estimate the velocity profile around the pipe centre. These authors used an Euler-Euler approach including interface forces (drag, lift and turbulent dispersion) and coupled to a standard k-ε closure.

On the last cases (see Figure 4.7), that specifically concern ice slurry flows, the developed modelling is this time associated with the realizable $k-\varepsilon$ turbulence closure for comparison with the SST $k-\omega$ (closure originally chosen for the modelling). Case IV (Fig. 4.7a) has not been introduced yet, since it is a little particular. This case considers upward vertical ice slurry flow in a rectangular cross-section duct, instead of horizontal pipe flows. The section of the duct measures 0.025 m (thickness Tk) $\times$ 0.305 m (width). Data collection is done at 0.61 m after the entrance. The axial bulk velocity U_m and the mean ice concentration Φ_m equal 0.151 $m.s^{-1}$ and 1.9$vol.\%$ respectively. The particle diameter is $d = 0.1$ mm and the bulk Reynolds number is $Re = 3760$. The numerical methodology is

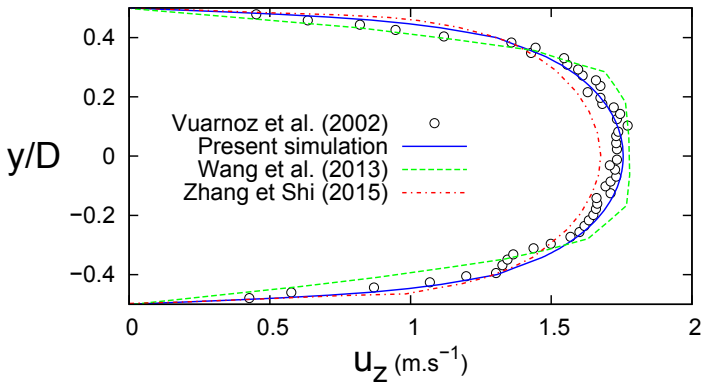

Figure 4.6 Radial distributions of the mean axial velocity at $z/L = 0.95$ for $\Phi_m = 0.17$ and $U_m = 1.3\ m.s^{-1}$. Comparisons between the present simulations, the experimental data of [Vuarnoz *et al.*, 2002] and the numerical simulations of [Wang *et al.*, 2013a] and [Zhang and Shi, 2015].

the same as with the circular cross-section pipes. The second of the two cases (Fig. 4.7b) simply corresponds to Case III presented just before.

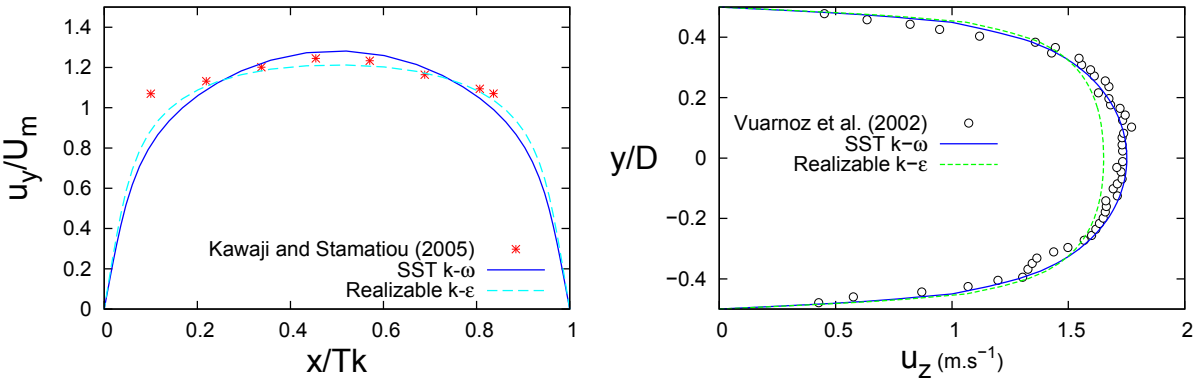

(a) (b)

Figure 4.7 Axial flow velocities : (a) [Stamatiou and Kawaji, 2005]'s case, vertical duct with a rectangular cross-section, u_y here represents the vertical velocity over the dimensionless section thickness x/Tk at mid-height ($y = 0.305m$), and (b) [Vuarnoz *et al.*, 2002]'s case, horizontal duct with a circular cross-section (see Case III). Comparison of two turbulence models with the experimental data.

It is worth mentioning that $Re < 4000$, for both cases of Figure 4.7. This tends to indicate that these flows are not fully turbulent. Usually, with ice slurry flows, it is hard to know precisely the flow regime around transitioning values. Albeit, both turbulence models (in association with the present flow modelling) are able to predict the experimental velocity profile quite well in each cross-section. Nevertheless, the realizable $k - \varepsilon$ reproduces more

accurately the squared velocity profile of Figure 4.7a but underestimates the experimental data of Figure 4.7b where the chosen turbulence model (SST) reveals very efficient. Globally, the SST $k-\omega$ predicts higher maximal velocities compared to the other turbulence model, probably due to lower turbulence levels.

4.3 Budget analysis of the transport equation for the particle volume fraction

Previously, a special effort has been made in order to build a comprehensive hydrodynamic model to predict isothermal ice slurry flows. In addition to the momentum equations, a transport equation for particle volume fraction was written (see in section 4.1.1). This equation comprises five distinct terms to account for the different physical mechanisms acting on the particle motion. Despite the fact that the entire modelling has been validated against a set of experimental data for transition and turbulent flows in horizontal straight pipes, the contribution of each individual term of the particle volume fraction equation was never well clarified.

So the present model is here analysed term by term; the experimental case of [Kaushal *et al.*, 2005] is re-employed as a simulation basis. These cases − involving a mixture of glass beads and water (Table 4.1) − went over a large range of flowing conditions and thus provide numerous data for solid suspension flows.

4.3.1 Case description

Geometrically, the study case of [Kaushal *et al.*, 2005] involves a horizontal straight pipe, with a diameter $D = 0.0549$ m. The particle volume fraction measurement is done after a length $L = 4.159$ m from the 180°-bend plugged at the entrance of the straight pipe. Pressure drop measurements are also done on a $3m$-portion beginning 0.599 m after the entrance.

The numerical geometry respects the aforementioned experimental criteria without accounting for the entrance 180°-bend (Figure 4.2). The mesh comprises around 2,400,000 cells and 3000 faces per cross-section. The inlet conditions are supposed uniform, and thus U_m as well as Φ_m are ruled uniformly at the inlet. U_m ranges from 2 to 3 $m.s^{-1}$ and Φ_m from 10% to 30%. Every set of experimental data is composed of three varying initial parameters : U_m and Φ_m (Table 4.2), and the particle diameter d taking two values : 125 μm and 440 μm.

U_m & Φ_m	$d = 125\mu m$	$d = 440\mu m$
2 $m.s^{-1}$ & 10%	$95,000$	
2 $m.s^{-1}$ & 30%	$46,000$	–
2 $m.s^{-1}$ & 20%	–	$72,000$
3 $m.s^{-1}$ & 20%	–	$109,000$

Table 4.2 Reynolds number Re ($= \rho_m U_m D/\mu_m$) for each simulated case.

Through the next sections, the general effects of each equation term (see Equation (4.6)) is exhibited, as well as the impact of each varying parameter taken individually (Φ_m, U_m and d). Equation 4.6 expresses the particle motion within the flowing mixture; the main features are recalled hereafter.

$$\underbrace{\frac{\partial \phi}{\partial t}}_{=0 \text{ steady flow}} = \underbrace{-\frac{\partial}{\partial x_i}(u_i \phi)}_{F_c} + \underbrace{\frac{\partial}{\partial x_i}(K_c a^2 \phi \frac{\partial \phi \dot{\gamma}}{\partial x_i})}_{D_c} + \underbrace{\frac{\partial}{\partial x_i}(K_\mu a^2 \dot{\gamma} \phi^2 \frac{1}{\mu_m} \frac{\partial \mu_m}{\partial x_i})}_{D_\mu} \underbrace{-\frac{\partial}{\partial x_i}(\omega_{s0} f(\phi) \phi \delta_{i3})}_{F_b} + \underbrace{\frac{\partial}{\partial x_i}(\Gamma_T \frac{\partial \phi}{\partial x_i})}_{D_t} \tag{4.16}$$

Nota : when these terms are positive, it means that there is a local gain of particles, and reversely when they are negative.

The first three elements – F_c, D_c and D_μ – come from the phenomenological model developed by [Phillips *et al.*, 1992] for concentrated suspensions. F_c corresponds to the convective flux, i.e. the particles drained with the whole mixture flow, D_c to the diffusion due to the spatial variation of the particle interaction frequency and D_μ to the diffusion due to the spatial variation of the effective viscosity. In addition, two more terms are introduced. The first term F_b accounts for the particle flux due to buoyancy effects (or more generally to settling effects, since in the case of glass particles heavier than the carrier fluid, the flux is vertically oriented towards the bottom). F_b also depends on the particle concentration : a damping function $f(\phi)$, derived from Gurel's formula ($f(\phi) = (1-\phi)^2/\mu_r$, see in [Blazejewski, 2012]) combined with the viscosity model (see in [Brouwers, 2010]), reduces the initial settling velocity when the concentration increases. The second term D_t accounts for the particle dispersion due to turbulence agitation [Pope, 2000].

4.3.2 Effects of the particle volume fraction Φ_m

On Figure 4.8, for which the model appears to be in very good conformity with the experimental concentration profile, one also observes the values of each component along the pipe vertical diameter. At a first sight, only D_t, F_b and F_c seem to have a relevant impact

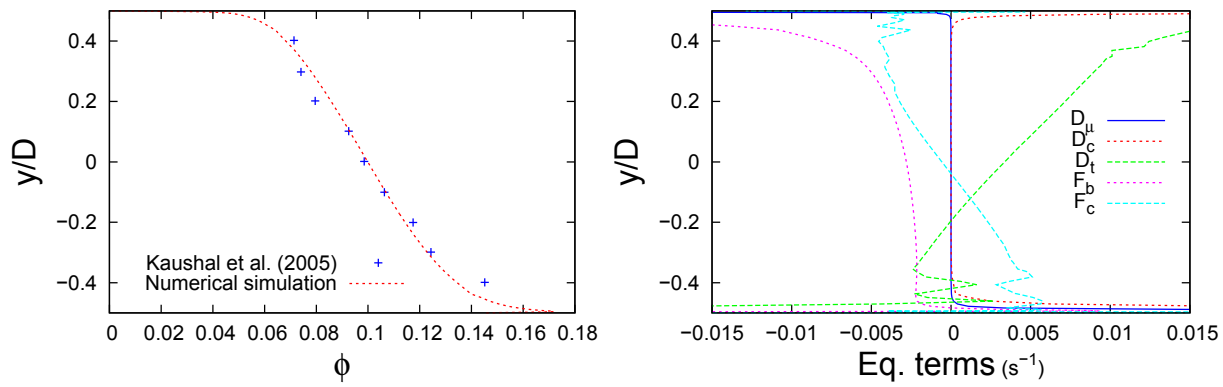

(a) (b)

Figure 4.8 Results obtained for $U_m = 2\ m.s^{-1}$, $\Phi_m = 10\%$ and $d = 125\ \mu m$ along the vertical diameter at $z = 4.16$ m: (a) particle concentration and (b) ϕ-transport equation components.

in the particle transport over the pipe height (the other values stay much lower). Globally, D_t decreases as the pipe height (y/D) diminishes, whereas F_b increases in the same orientation. Intuitively, it appears logical that the turbulent dispersion creates a filling of particles towards the upper part of the pipe and that the particle settling provokes an emptying of particles over this upper area. However, for the case exhibited on Figure 4.10, the previous observation might seem erroneous; different profiles show up that will be discussed farther below. Concerning D_μ and D_c, their action is not clear on Figure 4.8b, as both principally operate in the near wall region (Figure 4.9) and remain insignificant within the flow core for this set of parameters (i.e. with low particle concentration and small particle diameter).

On Figure 4.9a, one can observe a slight decrease of particle concentration very close to the bottom wall for each of the two considered Φ_m. This phenomenon of particle repelling, already exhibited by [Matousek, 2002], seems here correctly captured. According to the last author, this is the "result of the particle dispersion due to sporadic inter-particle contacts", likely to occur "in a region of steep velocity gradient (typically the near-wall region, see Figure 4.9b) and of high concentration of solids (towards the bottom wall presently)". Now referring to Figures 4.9c and 4.9d, D_c appears to be the origin of this repelling phenomenon (see its significant negative values), that the other terms compensate. When approaching the wall, the shear rate tends to become very strong, increasing at the same time the strength and the frequency of the particle collisions, and sending these particles away from the wall – as similarly described by [Matousek,

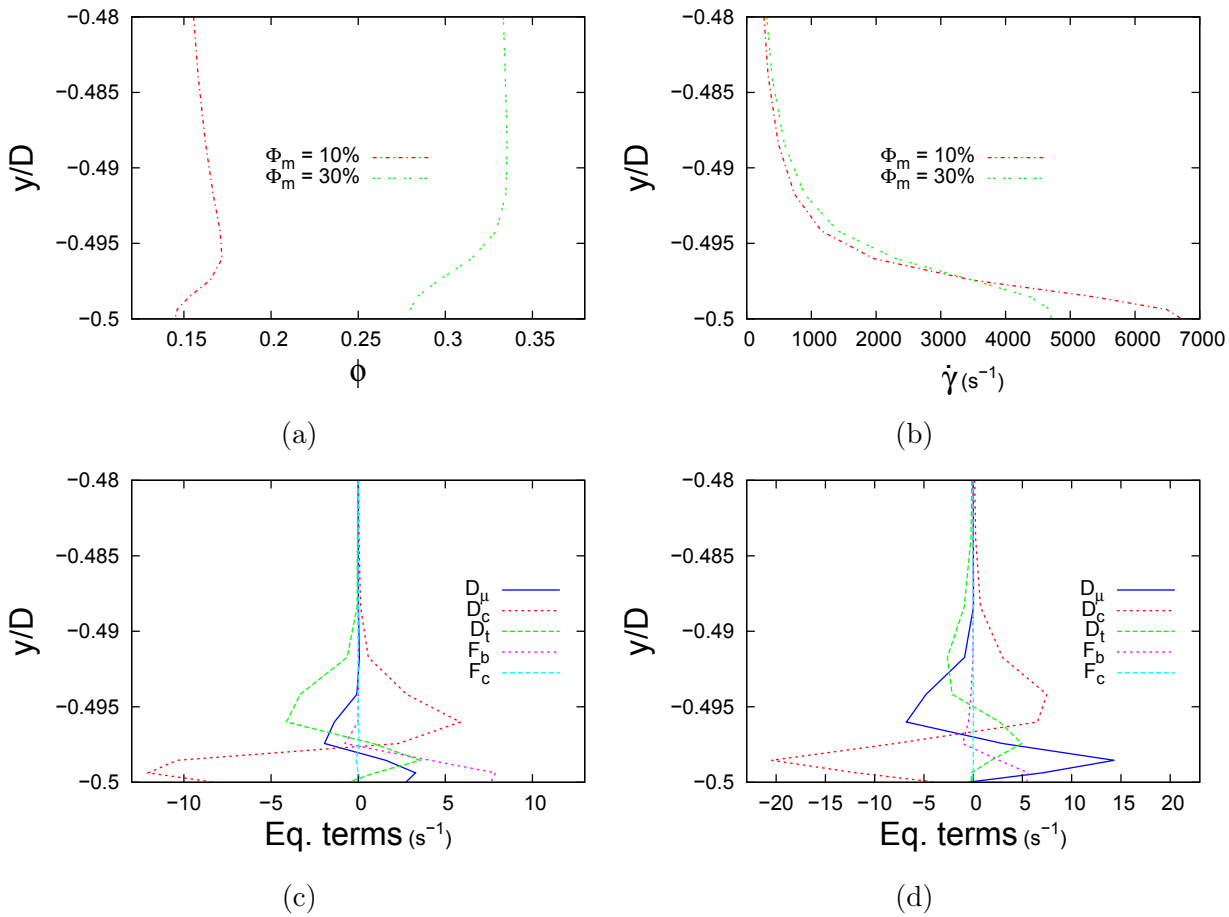

Figure 4.9 Results obtained for $U_m = 2\ m.s^{-1}$ and $d = 125\ \mu m$ along the vertical diameter above the bottom wall at $z = 4.16$ m: (a) particle concentrations, (b) shear rate magnitude and (c) and (d) ϕ-transport equation components for $\Phi_m = 10\%$ and $\Phi_m = 30\%$ respectively.

2002]. Beside, the augmentation of Φ_m clearly provokes an aggravation of the repelling phenomenon : the absolute peak value of $|D_c|$ is almost doubled from $\Phi_m = 10\%$ to $\Phi_m = 30\%$ ($|D_\mu|$ follows this value augmentation as well, to establish the balance).

As rapidly mentioned before, the fact that D_t takes positive values on the upper part of the pipe vertical diameter, that F_b takes negative values there and reversely, is more a general tendency (much better exhibited on Figure 4.11 below, for instance). On Figure 4.10b, the turbulent dispersion term D_t has become completely negative whereas particle settling term F_b seems this time completely positive along the whole pipe height. Comparatively to the previous case (with $\Phi_m = 10\%$), the mean particle volume fraction Φ_m has been tripled and the bulk Reynolds number Re almost divided by two (Table 4.2). The norms of $|D_t|$ and $|F_b|$ are lower in the second case (i.e. of higher particle concentration), especially

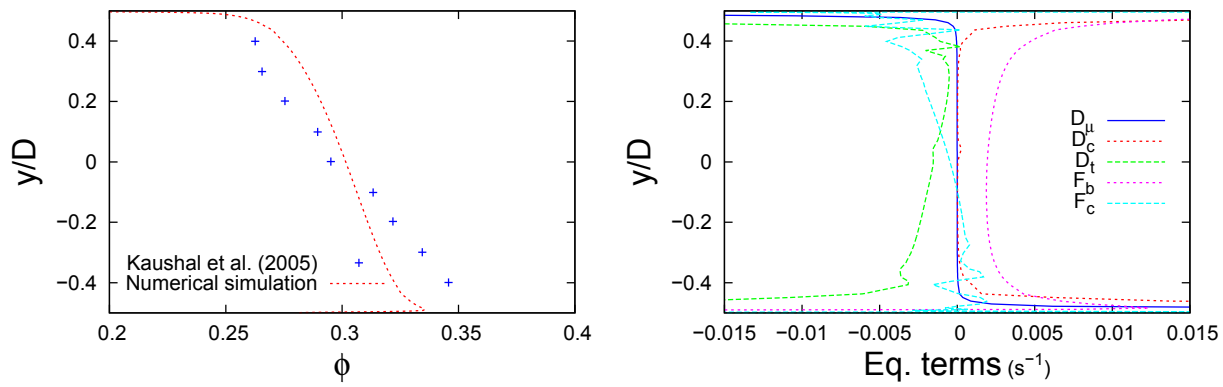

(a) (b)

Figure 4.10 Results obtained for $U_m = 2\ m.s^{-1}$, $\Phi_m = 30\%$ and $d = 125\ \mu m$ along the vertical diameter at $z = 4.16$ m: (a) particle concentration and (b) ϕ-transport equation components.

towards the top. This matches the fact that, with higher Φ_m, particle settling is more hindered as well as turbulence dispersion is more attenuated (this is understandable by the significant diminution of Re).

4.3.3 Effects of the flow velocity U_m

On Figure 4.11, the values of ϕ and of the various equation terms are plotted for two axial positions along the pipe. In fact, it was noticed that the numerical results match very well the experimental ones (except at the very bottom) at $z = 1.5$ m in terms of the particle concentration profile (Figure 4.11a) : a phase segregation clearly appears between the pipe upper and lower parts (also report to Figure 4.13a with tightened concentration iso-contours compared to Figure 4.13e). At $z = 4.16$ m, the numerical simulation yields a different concentration profile : there, the numerical values of ϕ augment quite uniformly from the top to the bottom of the pipe ($\frac{\partial \phi}{\partial (y/D)} \simeq -0.4, \forall (y/D)$). Figures 4.11b and 4.11c show two different behaviours for D_t (turbulence dispersion) and F_b (stratification). It seems that such a segregation phenomenon is related to the emergence of local maxima and minima for the two last parameters around the middle pipe height (see the peaks and the very specific shape of the profiles on Figure 4.11b). Originally, the mechanism causing the particle segregation is the stratification − modelled by F_b − whereas the turbulence dispersion would rather have a compensating effect in this case. Above a demarcation line (see the orange horizontal line on the figure), F_b takes negative values and, below this line, takes positive values. In combination with a very strong gradient $\frac{\partial F_b}{\partial y}$, this signifies that

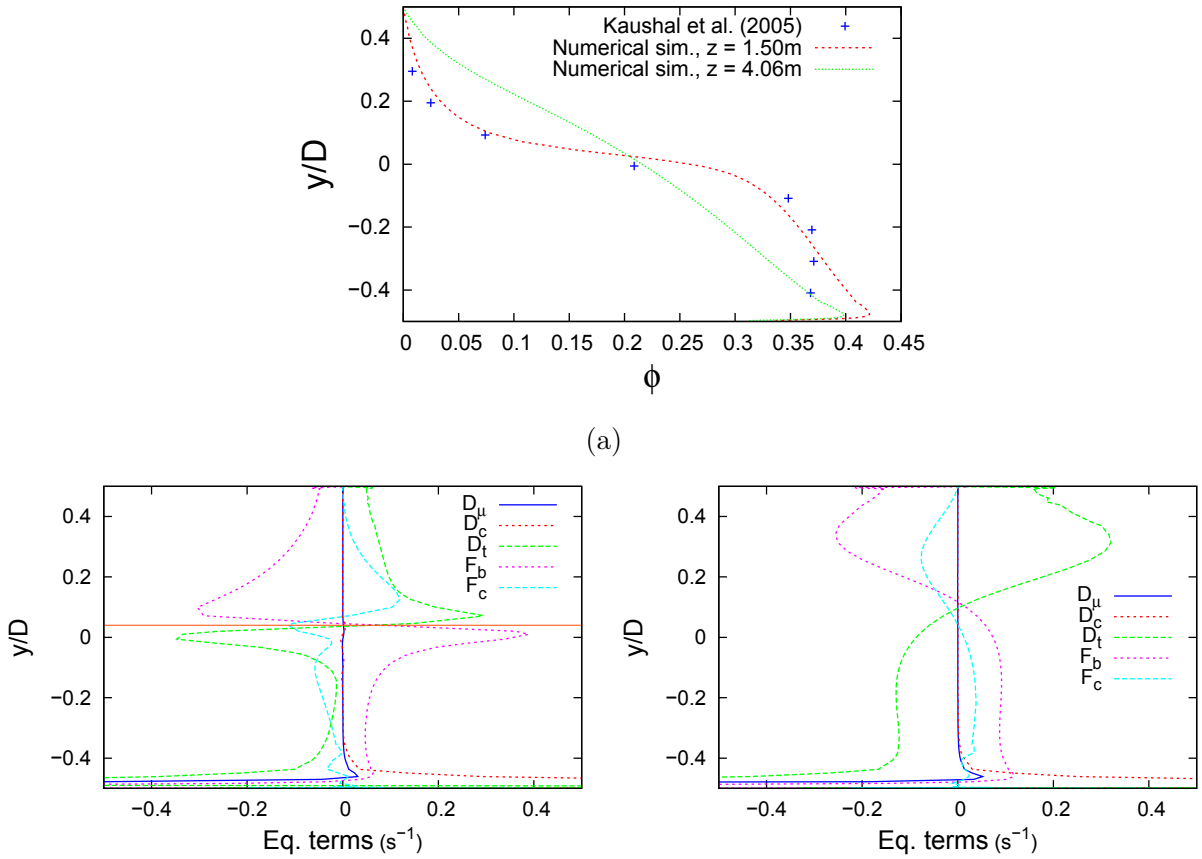

Figure 4.11 Results obtained for $U_m = 2\ m.s^{-1}$, $\Phi_m = 20\%$ and $d = 440\ \mu m$: (a) particle concentrations at two pipe axis positions, (b) and (c) ϕ-transport equation components at $z = 1.5$ m and at $z = 4.16$ m respectively, along the vertical diameter.

F_b causes an important particle transport towards the bottom at this mid-height location.

Mathematically, a parameter which remains hard to accurately model is the turbulence intensity. The turbulence dispersion − acting on the particles − directly depends on the local turbulence intensity and thus would require a very good approximation of the turbulence field to be capable of producing correct values. Figure 4.12 presents the turbulence kinetic energy k at both previous axial positions (see also Figure 4.13b and 4.13f for the cross-section k-fields). Although the two profiles compare very well on large zones near the top and bottom walls, they show large discrepancies in the flow core ($-0.3 < y/D < 0.2$) : there, the turbulence kinetic energy k at $z = 4.16$ m is much higher than at $z = 1.5$ m. In fact, $k_{z4.16} > 6 \times k_{z1.50}$ at $y/D \sim 0.02$. One can even remark that this position is similar

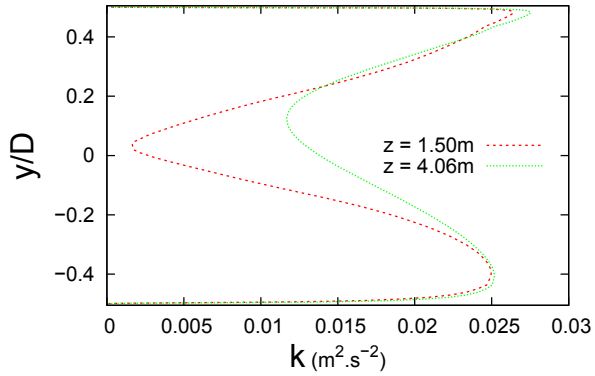

Figure 4.12 Turbulence kinetic energy k for $U_m = 2\ m.s^{-1}$, $\Phi_m = 20\%$ and $d = 440\ \mu m$.

to the orange line one. Obviously, this has a direct repercussion on the particle dispersion, with bringing a better homogenisation of the mixture in the flow core. A comparison of D_t between Figures 4.11b and 4.11c effectively reveals that $|D_t|_{z4.16} > |D_t|_{z1.50}$ (except locally, around pipe mid-height), which means a better efficiency of turbulent dispersion over a large pipe area.

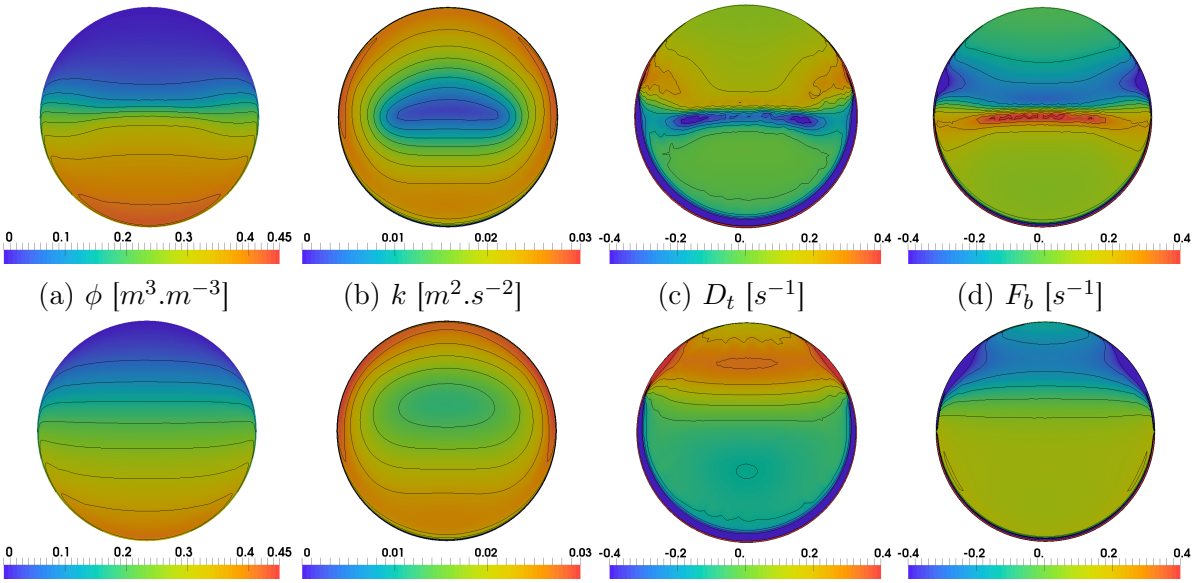

(a) ϕ $[m^3.m^{-3}]$ (b) k $[m^2.s^{-2}]$ (c) D_t $[s^{-1}]$ (d) F_b $[s^{-1}]$

(e) ϕ $[m^3.m^{-3}]$ (f) k $[m^2.s^{-2}]$ (g) D_t $[s^{-1}]$ (h) F_b $[s^{-1}]$

Figure 4.13 Results obtained for $U_m = 2\ m.s^{-1}$, $\Phi_m = 20\%$ and $d = 440\ \mu m$. From (a) to (d), pipe cross-section is located at $z = 1.5$ m, and from (e) to (h) at $z = 4.16$ m. (a) and (e) particle concentration, (b) and (f) turbulence kinetic energy, (c) and (g) turbulent dispersion effect, (d) and (h) buoyancy effect.

Even though, in the simulated case ($U_m = 2\ m.s^{-1}$, $\Phi_m = 20\%$, $d = 440\ \mu m$), the flow regime is still transitory at $z = 1.5$ m as well as this axial position does not correspond to the one where experimental measurements were done, the numerical data at $z = 1.5$ m illustrates very well the mechanics that triggers particle segregation (i.e. an upper pipe area of very little particle concentration and a lower pipe area highly concentrated, with a important concentration gradient between the two). Moreover, in this case, it would also suggest that the turbulence development is probably overestimated by the numerical simulation at $z = 4.16$ m. No experimental data exist to verify this fact though.

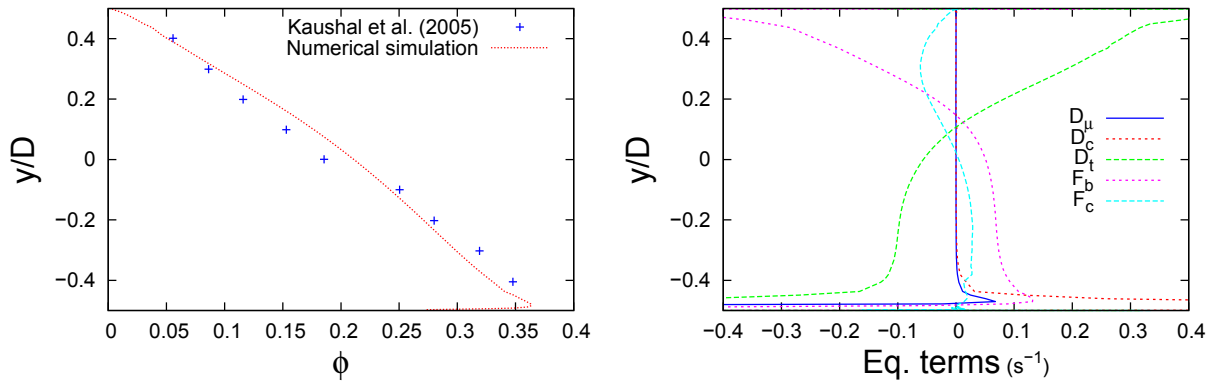

(a) (b)

Figure 4.14 Results obtained for $U_m = 3\ m.s^{-1}$, $\Phi_m = 20\%$ and $d = 440\ \mu m$ along the vertical diameter at $z = 4.16$ m: (a) particle concentration and (b) ϕ-transport equation components.

On Figure 4.14a, one sees that the particle concentration profile is slightly less heterogeneous than in the previous case. For $U_m = 3\ m.s^{-1}$, $\phi(0.4) = 0.05$ and $\phi(-0.5) = 0.35$, whereas for $U_m = 2\ m.s^{-1}$, $\phi(0.4) = 0.02$ and $\phi(-0.5) = 0.40$. The impact of velocity variation is much clearer on Figure 4.14b, where D_t and F_b profiles are strongly modified towards the pipe top : the norms of both terms keep increasing beyond $y/D \sim 0.3$. Re increases from $72,000$ to $109,000$, and the effects of turbulence augmentation are firstly perceptible in the upper pipe region as mentioned. In this region, the particle concentration is lower, so particle settling is stronger by definition, demanding a larger contribution from turbulence agitation D_t to bring up and maintain the particles there.

4.3.4 Effects of the particle diameter d

For particle diameter $d_2 = 440\ \mu m$, the initial particle settling velocity is much higher than $d_1 = 125\ \mu m$: $\omega_{s0}^2 = 53.3 > 6 \times \omega_{s0}^1$ as $\omega_{s0}^1 = 8.3\ mm.s^{-1}$. The impact of D_μ and D_c should also be affected as these terms are proportional to d^2 – considering identical

flow conditions, the values of each term with $d_2 = 440\ \mu m$ would be more than 12 times superior to the ones expected with $d_1 = 125\ \mu m$.

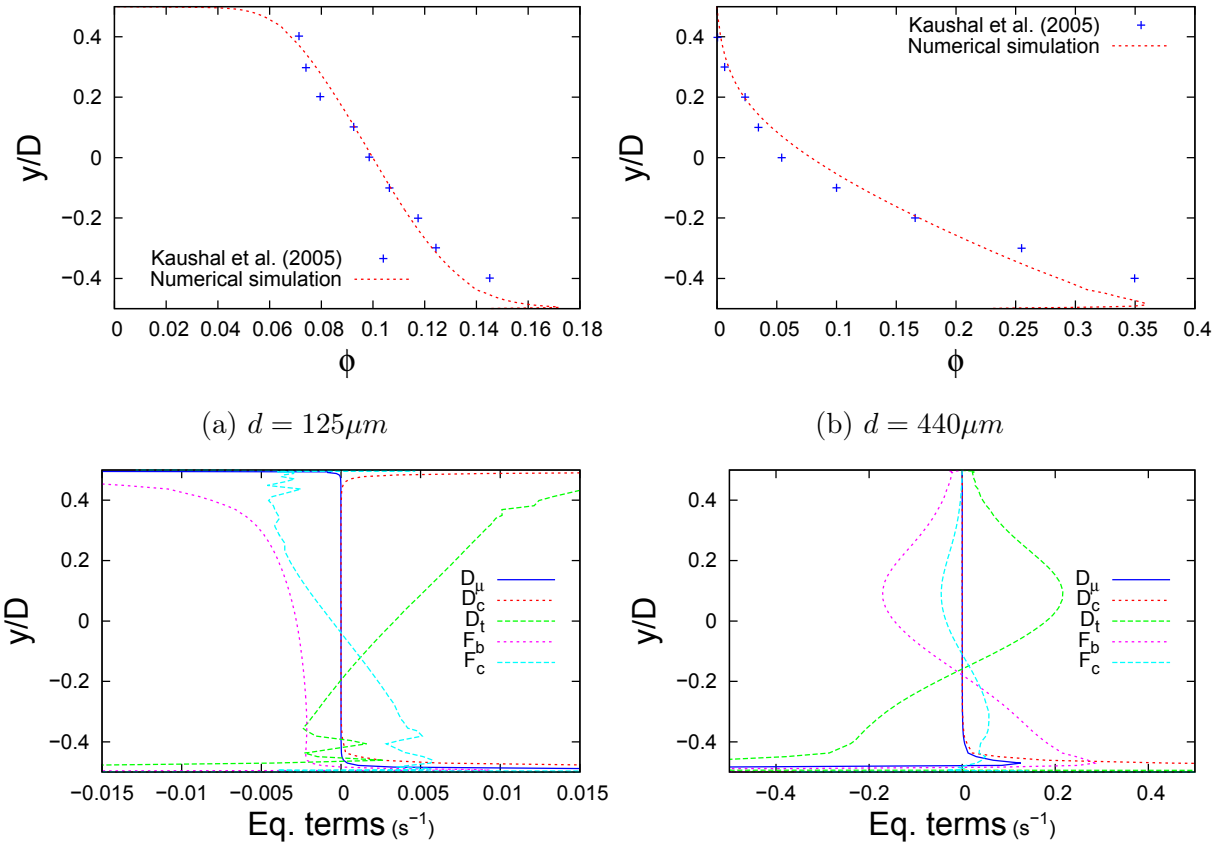

(a) $d = 125\mu m$ (b) $d = 440\mu m$

(c) $d = 125\mu m$ (d) $d = 440\mu m$

Figure 4.15 Results obtained for $U_m = 2\ m.s^{-1}$, $\Phi_m = 10\%$ along the vertical diameter at $z = 4.16$ m, for both particle sizes d: (a) and (b) particle concentrations, and (c) and (d) ϕ-transport equation components.

As well as with the concentration profiles $\phi = f(y/D)$, each equation term seems strongly impacted by the particle size variation. Concerning their values, there is almost 2 orders of magnitude between the two cases (see Figures 4.15c and 4.15d). The same observation can be done near the bottom wall (Figure 4.16) where it is perceptible for the terms D_μ and D_c. Moreover, the profiles of each term are sensibly different from one to another. For $d = 125\ \mu m$, D_t, F_b and F_c take higher values near the top wall, whereas for $d = 440\ \mu m$ these terms become higher near the bottom wall and for $y/D \sim 0.1$. As mentioned before, the particles d_2 are heavier than d_1, triggering the stratification and even the segregation in the second case (disappearance of the particle towards the pipe top, Figure 4.15b), where the effects of turbulent dispersion are not strong enough to compensate particle

settling, D_c crashes beyond $y/D \sim 0.1$, whereas this term significantly increases towards the upper wall on Figure 4.15a.

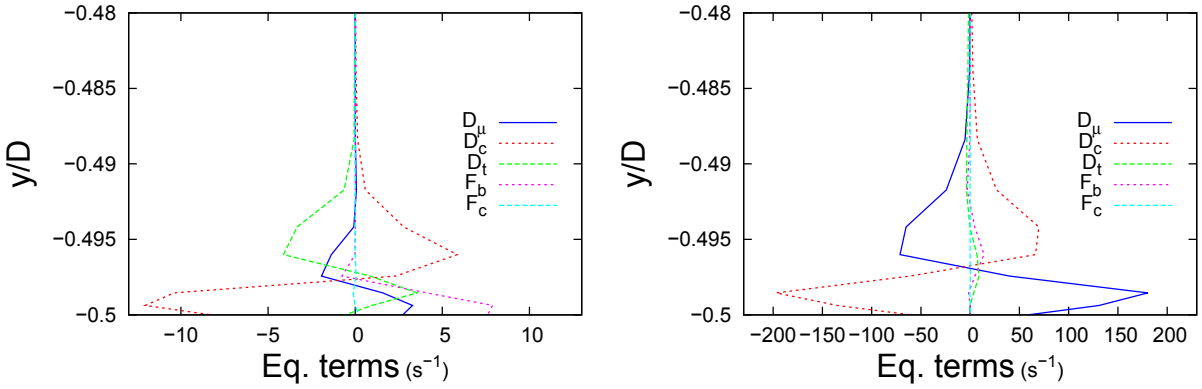

(a) (b)

Figure 4.16 Budget of the ϕ-transport equation components for $U_m = 2\ m.s^{-1}$, $\Phi_m = 10\%$ for: (a) $d = 125\ \mu m$ and (b) $d = 440\ \mu m$. Results obtained along the vertical diameter above the pipe bottom at $z = 4.16$ m.

At the bottom wall (Figure 4.16), in addition to the fact that the values considerably augment between $d = 125\ \mu m$ and $d = 440\ \mu m$, one sees that only D_μ and D_c predominate on Figure 4.16b (which was not the case for D_μ with the smaller particle diameter, see Figure 4.16a). These two terms traduce phenomena that act at the particle scale, and that highly depend on the particle size as noted at the beginning of the section (D_μ and $D_c \sim O(d^2)$). This explains the most the general augmentation of the two terms, but it does not obviously explain the new balance scheme. In the second case ($d = 440\ \mu m$), D_μ totally counterbalances D_c and the other three terms become totally negligible. In fact, there is also an important increase of the particle concentration between the two cases. The function modelling the mixture viscosity is of exponential form (one recalls that $\mu_m = \mu_l\{(1-\phi)\,/\,(1-1.5625\phi)\}^{4.444}$) so that the viscosity gradient gets larger when ϕ increases ($\partial\mu_m/\partial x_i$ is the basic engine to D_μ). As one may see on Figure 4.17, the viscosity gradient in the y-direction relative to the overall magnitude of the viscosity has considerably increased from the first case to the second near the bottom wall, explaining the reinforcement of D_μ. Moreover, the local raise of the viscosity is also factor to annihilate turbulence as well as particle settling.

On one hand, for very heterogeneous flows, such as these on Figures 4.15d or 4.11c, the equation terms D_t and F_b seem to balance each other with only a small relative contribu-

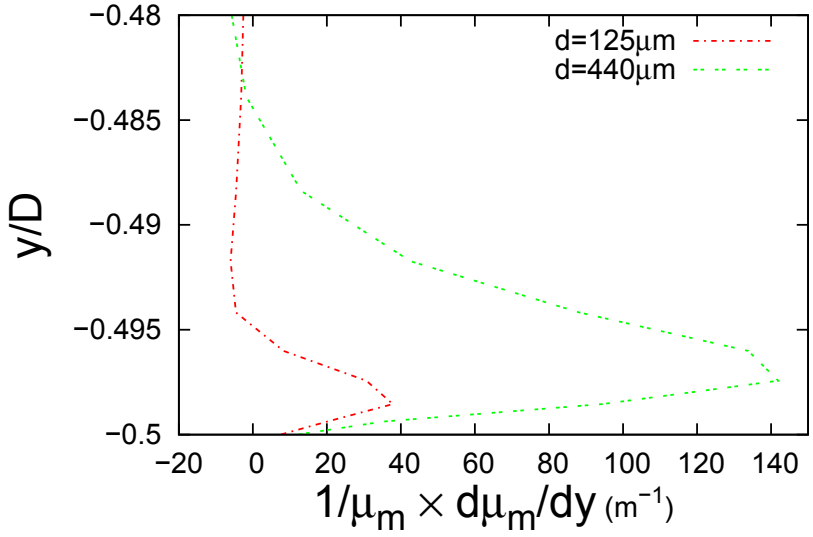

Figure 4.17 Results obtained for $U_m = 2\ m.s^{-1}$, $\Phi_m = 10\%$ and both particle diameters : $(1/\mu_m)(\partial\mu_m/\partial y)$ along the vertical diameter above the pipe bottom at $z = 4.16$ m.

tion of F_c. On the other hand, for homogeneous flows (where ϕ stays close to Φ_m and never reaches 0%) such as those on Figures 4.15c or 4.10, D_t and F_c seem to be correlated along the pipe vertical diameter. This may be interpreted so that, in case of homogeneous flows, particle settling (i.e. F_b) does no longer play a role of prime importance; F_c (traducing particle flux due to flow circulation within the pipe cross-section) tends to be preponderant over F_b (the stratification engine), as well as D_t does. In fact, F_c and D_t represent forces deriving from macro motions of the flow, which indeed have a stronger impact on smaller and lighter particles (relatively to F_b). However, F_b still has a balancing impact but not strong enough to provoke a real inhomogeneity. Thus, two specific behaviours between homogeneous and non-homogeneous flows are here exhibited with their phenomenology.

4.4 Brief summary

The present model has been assessed for a wide range of particle diameters ($0.09 \leq d \leq 0.44$ mm), Reynolds numbers ($3600 < Re < 230,000$) and volume fractions of particles ($0.019 \leq \Phi_m \leq 0.2$). It provides better predictions than more advanced two-phase Euler-Euler models coupled to $k - \varepsilon$ closures with standard wall functions [Wang *et al.*, 2013a; Zhang and Shi, 2015], while being less computational expensive. It highlights in particular the necessity of accounting for near-wall effects and choosing the appropriate turbulence closure. This will be confirmed by the numerical benchmark shown in Section 5.2. Further-

more, the budget analysis showed the model ability to reproduce some important features of solid-liquid suspension flows, such as the particle repelling phenomenon or the different levels of stratification as a function of the flow regime.

CHAPTER 5

Transitional and turbulent ice slurry flows in a horizontal straight pipe

The comprehensive understanding of ice slurry flow dynamics under isothermal conditions was the original objective of the numerical research. Also, the model developed and validated in the previous chapter is applied to several cases of ice slurry flows in a horizontal straight pipe. These cases are extracted from [Kitanovski and Poredoš, 2002]'s study, the principal elements are recapitulated in section 5.1. Firstly, a benchmark of turbulence models is done in section 5.2. Secondly, a detailed flow analysis is carried out in section 5.3, where [Kitanovski and Poredoš, 2002]'s analytical model is used for comparison.

5.1 Case description

The isothermal and turbulent (or transitional) flows of ice slurries in a horizontal straight pipe is considered under steady-state conditions. Table 5.1 summarizes the main geometrical and flow parameters for the configuration used by [Kitanovski and Poredoš, 2002]. Ice slurry is composed of liquid water with $10wt.\%$ ethanol. The two varying parameters are the inlet axial velocity U_m and the inlet particle concentration Φ_m.

$D\ (m)$	$L\ (m)$	$d\ (m)$	$U_m\ (m.s^{-1})$	$\Phi_m\ (m^3.m^{-3})$	$T\ (°C)$
0.0272	1.68	0.001	0.5, 1, 1.5, 2	0.10	-5
			0.5, 1, 1.5, 2	0.25	-6.32

$\rho_s\ (kg.m^{-3})$	$\rho_l\ (kg.m^{-3})$	$\mu_l\ (Pa.s)$	$\omega_{s0}\ (m.s^{-1})$
917.65	983.9	0.00459	0.005076
918.07	982.0	0.00559	0.003956

Table 5.1 Geometrical characteristics and flow parameters, μ_l and ρ_l come from the empirical data given by [Kauffeld *et al.*, 2005].

The operating conditions (U_m, Φ_m) are reported on the safety diagram provided by [Snoek, 1993] on Figure 5.1a. They cover the three regions of the diagram, including the "not recommended" region at low inlet velocities. This region is associated with possible clogging phenomena in the heat exchangers used to transport the cold. With the development of new ice slurry generators able to produce highly concentrated slurries (Φ_m up to 65% in [Trabelsi *et al.*, 2017] for example) and the possibility to reduce the size of the transport

systems (for the same amount of cold energy transported), the diagram has to be revisited. It will be shown in the following that no slug flow or clogging effects are reported numerically.

Depending on the set of parameters (U_m, Φ_m), different flow patterns have been reported in the literature [Kauffeld *et al.*, 2005; Kitanovski *et al.*, 2005], from moving or stationary bed flows to heterogeneous or homogeneous flows. Furthermore, the flow pattern also depends on the mean particle diameter. Figure 5.1b reports the transition diagram established by [Kitanovski *et al.*, 2005] for ice slurries with $10wt.\%$ of ethanol. This diagram has to be analysed with a certain caution. Firstly, the particle diameter considered in the present simulations is larger than the diameter (0.5 mm) used by [Kitanovski *et al.*, 2005] and secondly, this diagram is based on a theoretical model based on the [Wasp *et al.*, 1977]'s criteria. Regarding the diagram, three test cases remain in the transition from heterogeneous to homogeneous flows though regarding the diagrams established by [Reghem, 2002] or reported in [Kauffeld *et al.*, 2005], the eight test cases would be within the homogeneous flow region. It will be discussed and clarified in the following.

5.2 Numerical benchmark of turbulence models

Four turbulence closures in their low Reynolds formulation are compared for $\Phi_m = 0.25$ and $U_m = 1\ m.s^{-1}$. It is important to mention that the RSM presently used calculates the ω scale for the turbulence dissipation instead of ε. As shown in Figure 5.2, the RNG $k-\varepsilon$ predicts a more homogeneous concentration profile. Note that other $k-\varepsilon$ models including the standard and realizable models have been also considered but led to similar results and so are not shown here for the sake of clarity. It confirms the results of [Bordet *et al.*, 2016b] for solid suspensions. The RSM and the two $k-\omega$ models provide the same profile in the bulk region. However, the RSM does not exhibit an accumulation of ice particles along the top wall compared to the $k-\omega$ models. Though the standard $k-\omega$ and SST $k-\omega$ models provide similar profiles, the SST formulation is preferred for reasons evoked in section 4.1.1 and for its good performance for all types of solid suspension flows (see [Bordet *et al.*, 2016b] and section 4.2).

Figure 5.3 displays the law of the wall, i.e. the distribution of the normalized velocity $u^+ = u/u_\tau$ with the wall distance $y^+ = u_\tau \Delta r/\nu$. Δr refers to the cell wall distance and u_τ to the friction velocity defined as: $u_\tau = \sqrt{\tau_w/\rho_m}$. It confirms that the four turbulence closures predict fairly well the flow in the viscous sub-layer (up to $y^+ \simeq 5$) for which $u^+ = y^+$. After the buffer region, the velocity profiles may be presented by the classical

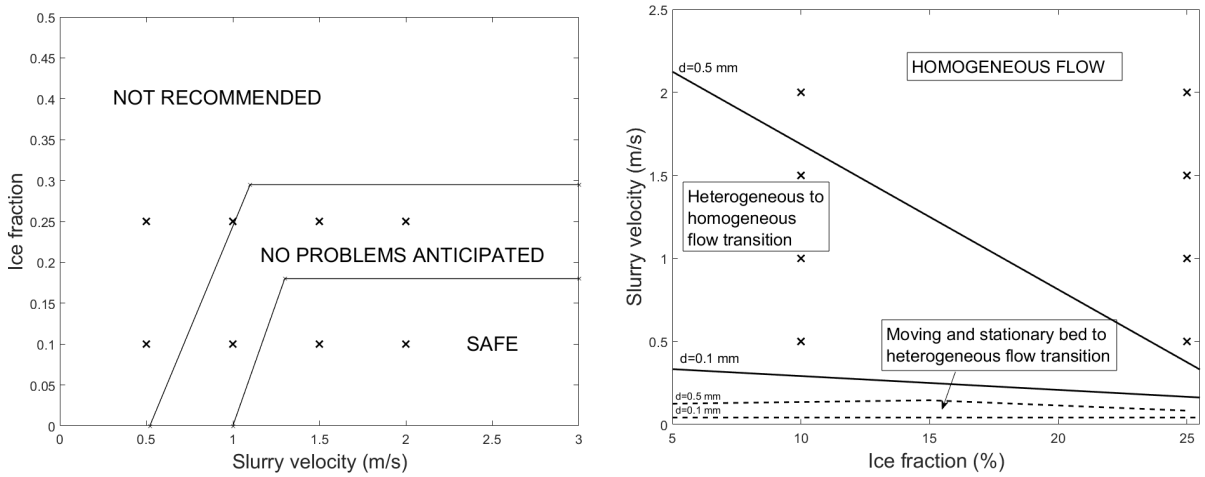

(a) (b)

Figure 5.1 (a) Safety diagram after [Snoek, 1993]; (b) Flow pattern transition diagram established by [Kitanovski *et al.*, 2005] for ice slurries with $10wt\%$ of ethanol. The symbols ($\times$) represent the present simulations discussed in Section 5.3.

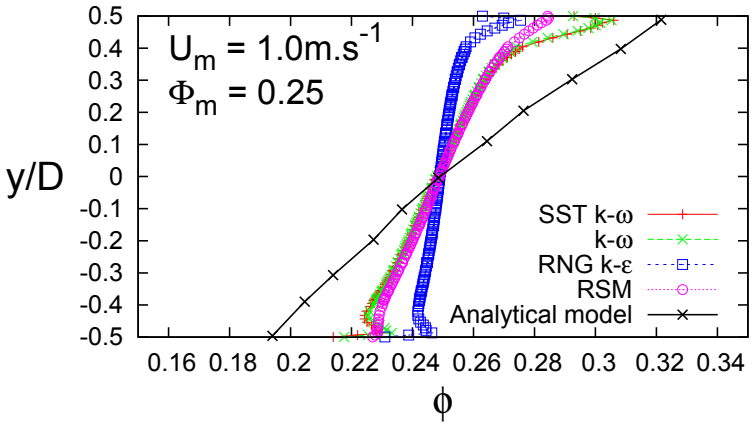

Figure 5.2 Radial distributions of the ice concentration ϕ ($m^3.m^{-3}$) at $z/L = 0.95$ for $\Phi_m = 0.25$ and $U_m = 1\ m.s^{-1}$; Comparison between the present simulations obtained using different RANS closures and the analytical model of [Kitanovski and Poredoš, 2002].

log-law:

$$u^+ = \frac{1}{A} \ln y^+ + B \tag{5.1}$$

where $A = 0.436$ and $B = 6.13$ are two constants. The logarithmic region is located for $y^+ \geq 30$. For the four turbulence models, the constant A is equal to $A \simeq 0.436$, which perfectly matches the recommended value for turbulent pipe flows [Zagarola and Smits, 1998]. The constant B usually lies between about 4.9 and 5.5. This small difference may

be easily explained by curvature effects and the two-phase nature of the flow. The RSM based on the dissipation rate ε of the turbulence kinetic energy (not shown here) fails to predict the right profile in the logarithmic region and tends to laminarise the flow. It points out the necessity of using the specific dissipation rate ω as the characteristic scale of turbulence instead of ε.

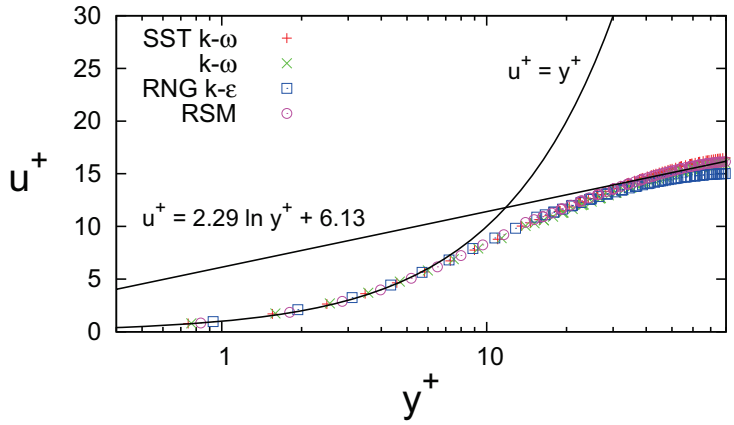

Figure 5.3 Law of the wall for the boundary layer along the top wall. See legend of Figure 5.2.

The radial distributions of the turbulence kinetic energy k starting from the top wall are shown in Figure 5.4 for the four turbulence closures. The RNG $k-\varepsilon$ model predicts higher turbulence kinetic energy levels than the other models. It is related to a higher turbulent dispersion of the particles through the term Γ_T and then to a more homogeneous concentration profile as shown previously. The other three models essentially predict the same profile. Compared to the $k-\omega$ models, the RSM predicts similar levels of turbulence kinetic energy, while exhibiting a more homogeneous ice concentration profile close to the walls. This may be explained by the anisotropy of the RSM and especially the contributions of the shear stress components to the term Γ_T.

Figure 5.5 shows the turbulence kinetic energy k over the whole pipe cross-section for each one of the turbulence closures. As expected, the values given by the standard $k-\omega$ and the SST one are sensibly similar. Albeit, it seems that the standard version predicts slightly lower levels of k around the pipe middle, which apparently does not have any repercussion on the ice concentration profile. Despite the fact that the turbulence kinetic energy values of the RSM-ω are close to the ones of the two $k-\omega$ models, asymmetric structures seem to appear with this last model. It is due to the anisotropic character of such a model. About the calculation cost, one must recall that the RSM is much more expensive, solving 7 equations for turbulent quantities instead of 2. Concerning the RNG $k-\varepsilon$, the values

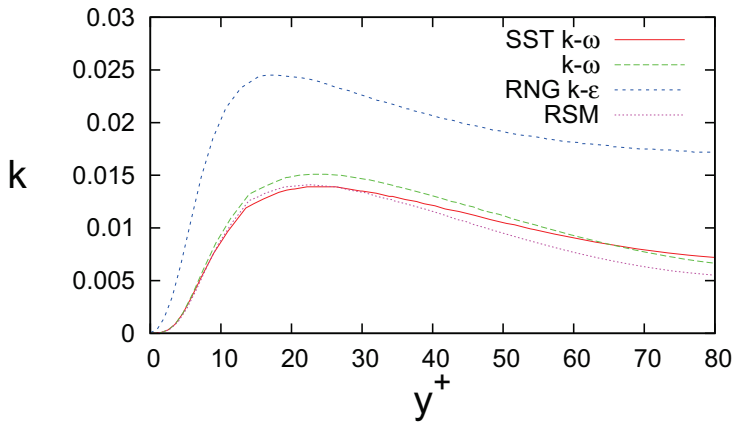

Figure 5.4 Wall profiles of the turbulence kinetic energy k $(m^2.s^{-2})$. See legend of Figure 5.2.

of k are much higher than those given by the previous turbulence closures – even in the flow core – confirming the previous observations along the vertical pipe diameter. As seen in section 4.3, turbulence modelling represents an essential step in the process for the prediction of the right ice concentration profiles, since it has a strong influence indeed.

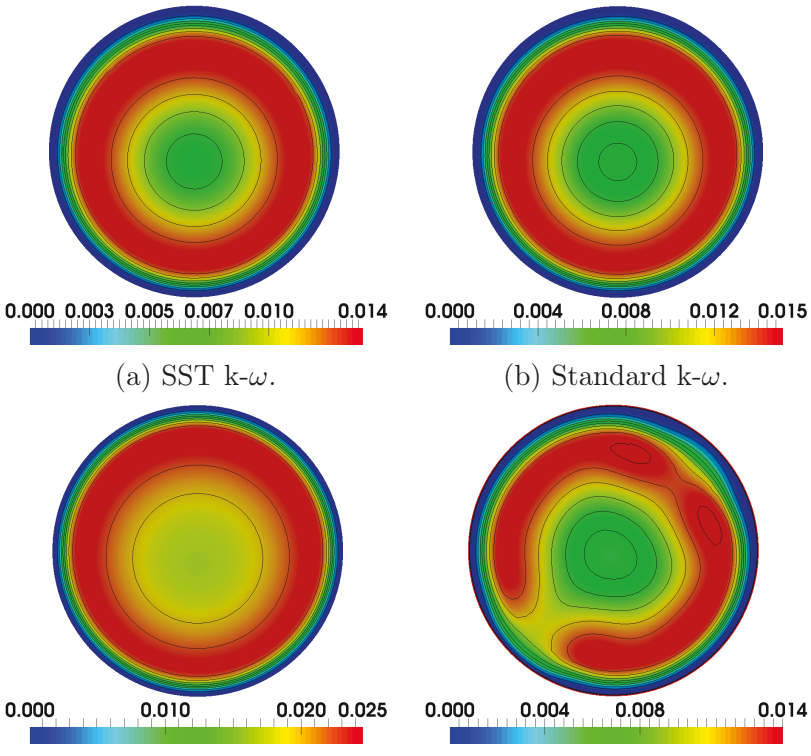

(a) SST k-ω. (b) Standard k-ω.

(c) RNG k-ε. (d) RSM-ω.

Figure 5.5 Fields of turbulence kinetic energy k $(m^2.s^{-2})$ over a pipe cross-section. See legend of Figure 5.2.

To explain the peculiar behaviour of the RNG $k-\varepsilon$ model and, especially, understand the overestimation of turbulence kinetic energy, budgets have to be done to carefully quantify the contribution of each term involved in the equation of k, which can be written in the following general form:

$$\frac{\partial k}{\partial t} + \underbrace{A_k}_{\text{advection}} = \underbrace{P_k}_{\text{production}} - \underbrace{\varepsilon_k}_{\text{dissipation}} + \underbrace{D_k^{\nu}}_{\text{laminar diffusion}} + \underbrace{D_k^{T}}_{\text{turbulent diffusion}} \tag{5.2}$$

where $\partial k/\partial t = 0$ for steady-state calculations. The terms A_k, P_k, ε_k, D_k^{ν} and D_k^{T} are:

$$A_k = \frac{\partial (k u_i)}{\partial x_i} \tag{5.3}$$

$$P_k = \frac{\tau_{ij}}{\rho_m} \frac{\partial u_i}{\partial x_j} \tag{5.4}$$

$$\varepsilon_k = \beta^* k \omega \quad or \quad \varepsilon \tag{5.5}$$

$$D_k^{\nu} = \frac{\partial}{\partial x_i} \left[\nu_m \frac{\partial k}{\partial x_j} \right] \tag{5.6}$$

$$D_k^{T} = \frac{\partial}{\partial x_i} \left[\frac{\nu_T}{\sigma_k} \frac{\partial k}{\partial x_j} \right] \tag{5.7}$$

with σ_k a model constant and ν_T the turbulent viscosity, which both depend on the model.

Figure 5.6 presents the corresponding profiles as a function of the wall distance y^+. As expected, for all models, the two main contributions in the turbulence kinetic energy equation are the production term counter-balanced by the dissipation, while advection has a negligible contribution to the $k-$budget. It is also noticeable that the viscous diffusion dominates the turbulent one. The RNG $k-\varepsilon$ exhibits a peculiar behaviour compared to the other models with higher values of dissipation and viscous diffusion terms in the viscous sub-layer and of the production term in the buffer region ($y^+ \simeq 11$). It confirms that models based on the specific dissipation rate ω better perform than those based on the dissipation rate ε.

Note that this numerical benchmark has also been done for other sets of parameters (U_m, Φ_m) leading to the same conclusions. Figures 5.3, 5.4 and 5.6 displayed radial distributions along the vertical diameter from the top wall to the pipe centre. Albeit, it has been carefully checked that extracting the profiles from the bottom wall to the axis leads to similar results (Figure 5.5), which highlights the weak influence of the local ice fraction on the law of the wall and budgets of the turbulence kinetic energy.

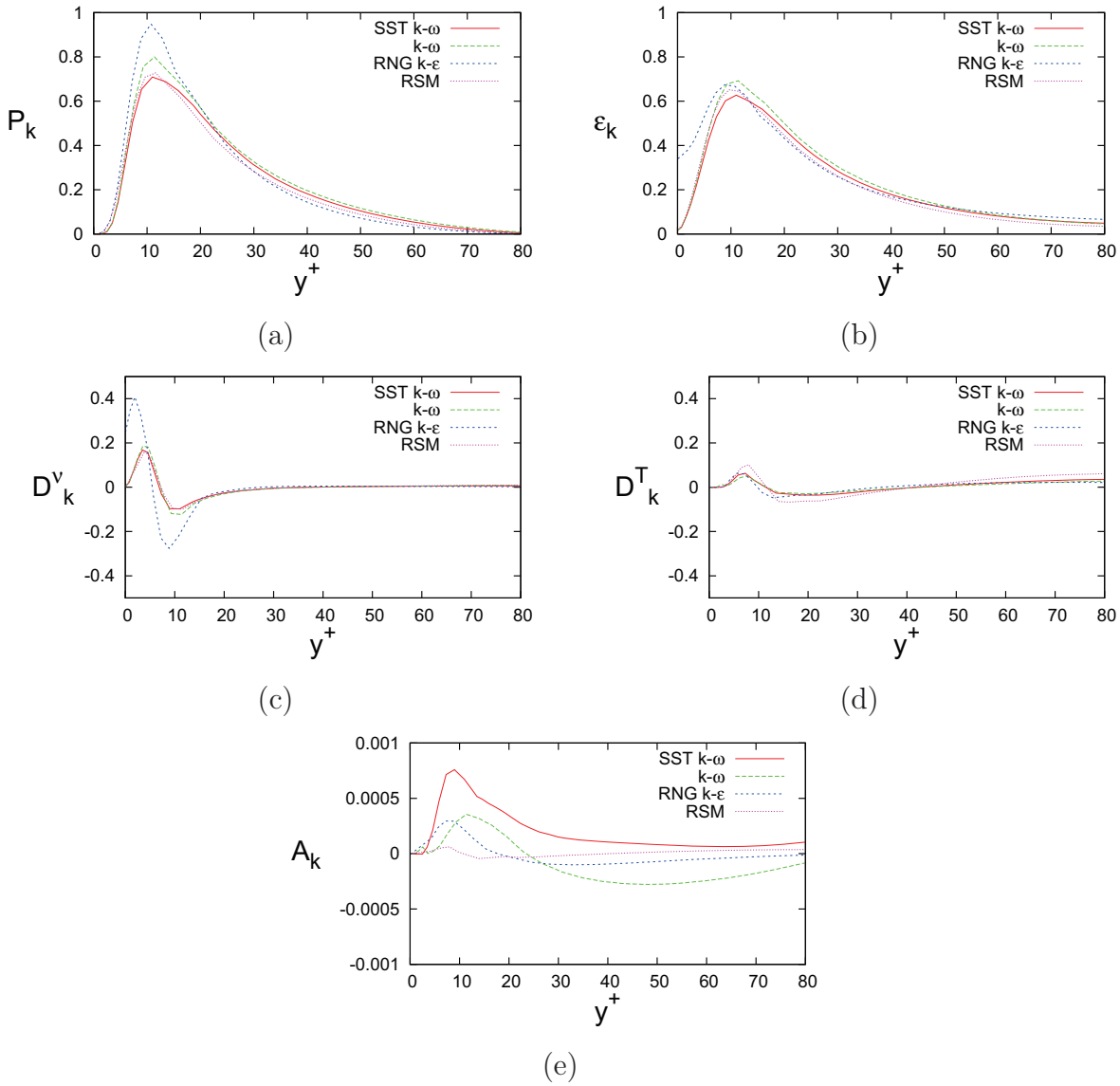

Figure 5.6 Budgets for the turbulence kinetic energy. See legend of Figure 5.2.

5.3 Influence of the ice concentration and flow velocity

For ice slurry flows in pipes and small ice particles ($100 \leq d \leq 300$ μm), four flow regimes are usually highlighted experimentally (see section 2.1.1) depending on the inlet axial velocity U_m and the inlet particle concentration Φ_m: homogeneous, heterogeneous, moving and stationary bed. Eight flow conditions are considered here: $\Phi_m = 0.1$ or 0.25 and $U_m = 0.5$, 1, 1.5 or 2 $m.s^{-1}$ to match the conditions investigated by [Kitanovski and Poredoš, 2002]. The physical and flow parameters are recalled in Table 5.1. Though the ice particle diameter $d = 1mm$ is larger than those considered by [Kitanovski *et al.*, 2005]

in Figure 5.1b, one may expect to obtain heterogeneous flows for $\Phi_m = 0.1$ and $U_m \leq 1$ $m.s^{-1}$ and homogeneous flows otherwise.

Generally, heterogeneous flows are observed at lower inlet velocities providing a non uniform ice particle distribution. Ice particles are mainly concentrated at the top wall of the pipe. For homogeneous flows, the ice concentration is more uniformly distributed along the radial direction at a given axial position. Stationary or moving bed flows are usually encountered at very low inlet axial velocities and for lower inlet ice concentration. The maximum value of ice concentration is thus reached near the top wall of the pipe. The model presently used only solves the mixture velocity and ice concentration fields, but does not for the velocities of the ice particles and the liquid phase separately. Thus, all attempts to observe one of these four regimes have to be taken with a certain caution.

5.3.1 Ice concentration

Figures 5.7 and 5.8 show comparisons between the present model combined with the SST k-ω turbulence model and the analytical model of [Kitanovski and Poredoš, 2002] in terms of the radial distributions of ice concentration close to the pipe outlet $z/L = 0.95$. Two ice concentrations are considered $\Phi_m = 0.1$ (Fig.5.7) and 0.25 (Fig.5.8) together with four different values of the inlet axial velocity U_m leading to eight couples of inlet conditions. The analytical model of [Kitanovski and Poredoš, 2002] assumes that the ice-slurry flow is fully suspended and homogeneous locally. For this reason, it can only represent homogeneous and heterogeneous flow regimes (see section 2.3.2). [Thomas, 1965]'s equation is considered to evaluate the local dynamic viscosity of the slurry. The radial profile for the ice concentration was determined using a diffusion equation for a turbulent flow. The main diffusion coefficient is based on the friction coefficient determined using the modified Colebrook formula [Doron *et al.*, 1987], while the hindered terminal velocity of the ice-particle is evaluated through the correlation proposed by Richardson and [Richardson and Zaki, 1954]. This model being simpler than the present one is used here for discussion only.

Figure 5.7 presents the ice concentration profiles for the lowest inlet concentration $\Phi_m = 0.1$. For the lowest inlet axial velocity $U_m = 0.5$ $m.s^{-1}$, the present model predicts a very heterogeneous flow as proposed by [Kitanovski and Poredoš, 2002]. The concentration maximum obtained at the top of the pipe is $\phi_{max} \simeq 0.29$, which is relatively well predicted by the analytical model. From the new classification established in section 3.2.1, the flow might also be considered as stratified St #2 since a thin layer empty of ice particles notably appears at the pipe bottom. Increasing the inlet axial velocity from 0.5 $m.s^{-1}$ ($Re = 2120$)

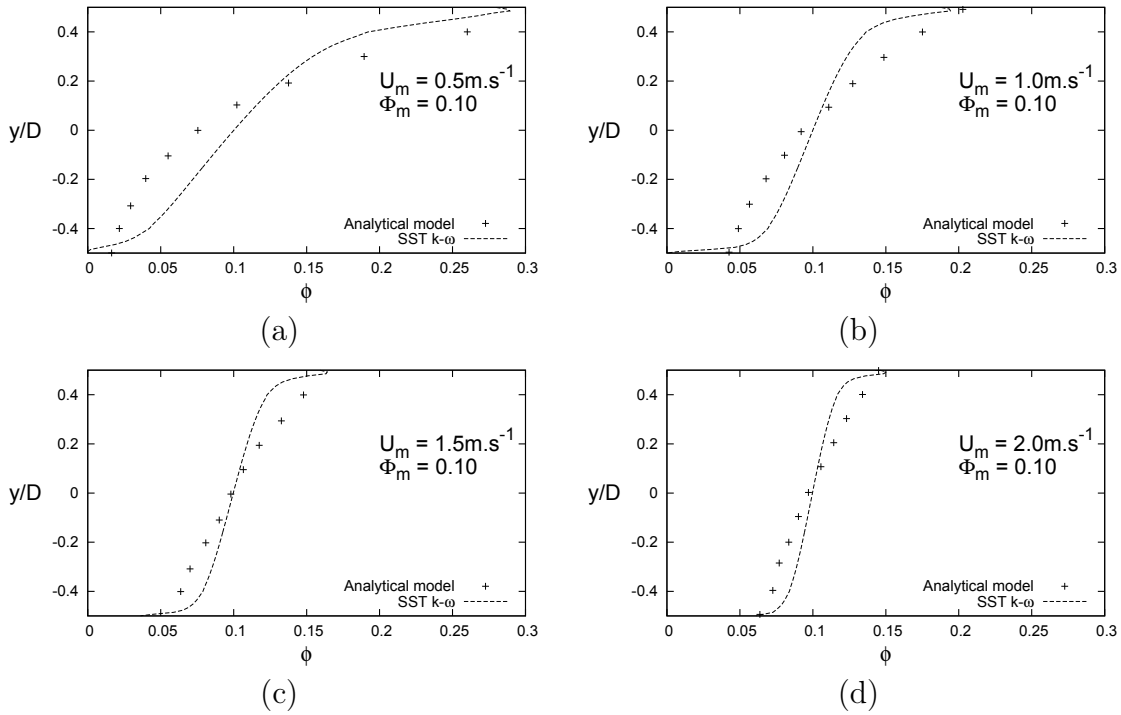

Figure 5.7 Ice concentration profiles of ice slurry along the vertical symmetry axis at $z/L = 0.95$ for inlet ice concentration $\Phi_m = 0.1$. Comparison between the present simulation and the analytical model of [Kitanovski and Poredoš, 2002] for four values of the inlet axial velocity U_m.

to 2 $m.s^{-1}$ ($Re = 8480$) leads progressively to more homogeneous concentration profiles with decreasing values of ϕ_{max} at the top of the pipe. For example, with $\phi_{min} \simeq 0.07$ and $\phi_{max} \simeq 0.15$ for $U_m = 2\ m.s^{-1}$, the ice slurry flow is then very close to a homogeneous distribution of the ice concentration. In that case, the turbulent agitation is preponderant over the buoyancy and results in an important dispersion of the ice particles. Interestingly, the thinning of the hydrodynamic boundary layer at the bottom of the pipe may be seen from the ice concentration profiles. Globally, a thin fluid layer remains near wall, notably due to the no-slip condition and the absence of turbulent diffusion (remember that the issue was discussed in details in Section 4.3), whereas the analytical model predicts ice concentration profiles uniformly progressing. As done earlier by [Matousek, 2002], [Wang *et al.*, 2013b] also reported the existence of a similar behaviour (near wall particle concentration decrease) for slurry flows composed of water and thin sand particles. Nevertheless, the last authors noticed that the particle repelling phenomenon could not be captured by their CFD calculations using a mixture model since the algebraic slip formulation was not accurate enough to describe the near wall significant phase slip. [Onokoko and Galanis, 2013] performed calculations using a realizable $k-\varepsilon$ turbulence model in a $3m$-long pipe.

For $d = 0.4$ mm, $U_m = 2\ m.s^{-1}$ and $\Phi_m = 0.1$, the authors obtained a flow region with constant ice concentration around the pipe axis, whose radial extension decreases when moving towards the pipe outlet. It confirms the present results using the RNG $k - \varepsilon$ closure (Figure 5.2), which tends to homogenize the flow due to an excessive turbulent diffusion.

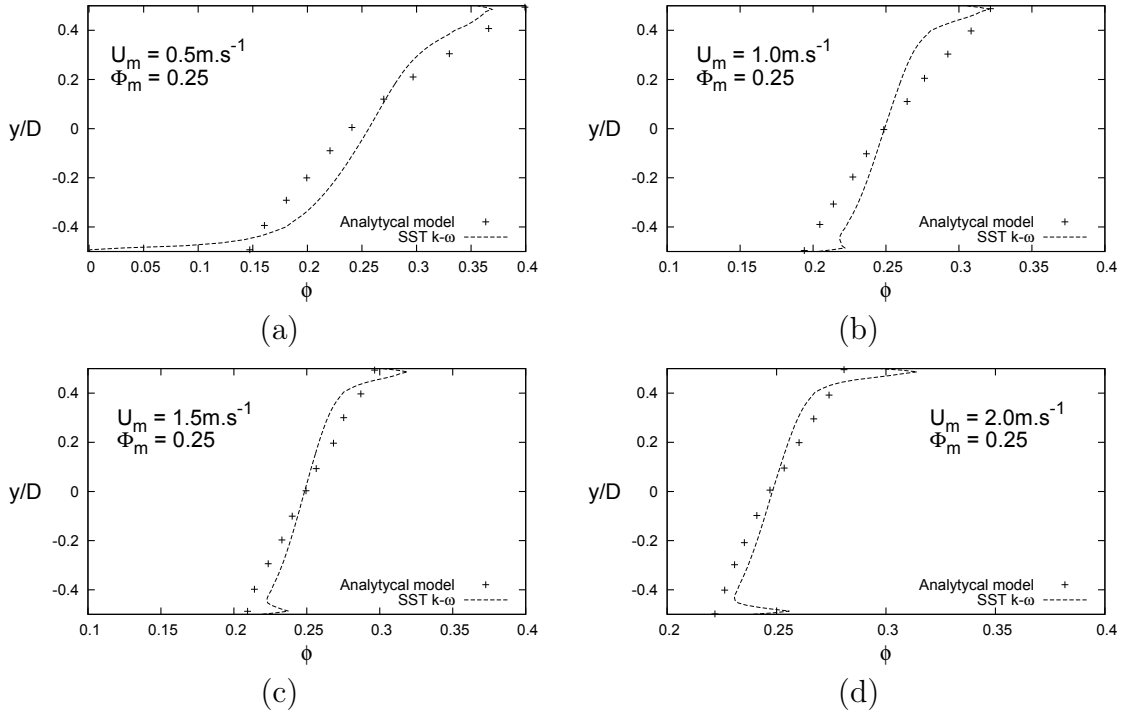

Figure 5.8 Ice concentration profiles of ice slurry along the vertical symmetry axis at $z/L = 0.95$ for inlet ice concentration $\Phi_m = 0.25$. Comparison between the present simulation in turbulent flow regime and the analytical model of [Kitanovski and Poredoš, 2002] for four values of the inlet axial velocity U_m.

Figure 5.8 shows the same profiles for a higher ice concentration $\Phi_m = 0.25$. For $U_m = 0.5$ $m.s^{-1}$, the ice concentration profile is similar to the one obtained for $\Phi_m = 0.1$ but as it will be shown later (Fig. 5.12d), it is accompanied by a very low axial velocity flow region along the top wall. It could then be referred to a stationary bed like flow regime, though the concentration profile does not show a phase separation. Increasing the inlet axial velocity leads to a more uniform profile for which the ice concentration slightly varies linearly with the radial direction. The flow is then considered as heterogeneous. The concentration also progressively decreases from $\phi_{max} \simeq 0.37$ for $U_m = 0.5\ m.s^{-1}$ ($Re = 970$) to 0.31 for $U_m = 2\ m.s^{-1}$ ($Re = 3880$). For this inlet ice concentration, the repelling phenomenon is quite well reproduced close to both walls. It is interesting to note that the analytical

model reproduces quite well the slope of the ice concentration profile obtained by the turbulence model in the bulk flow.

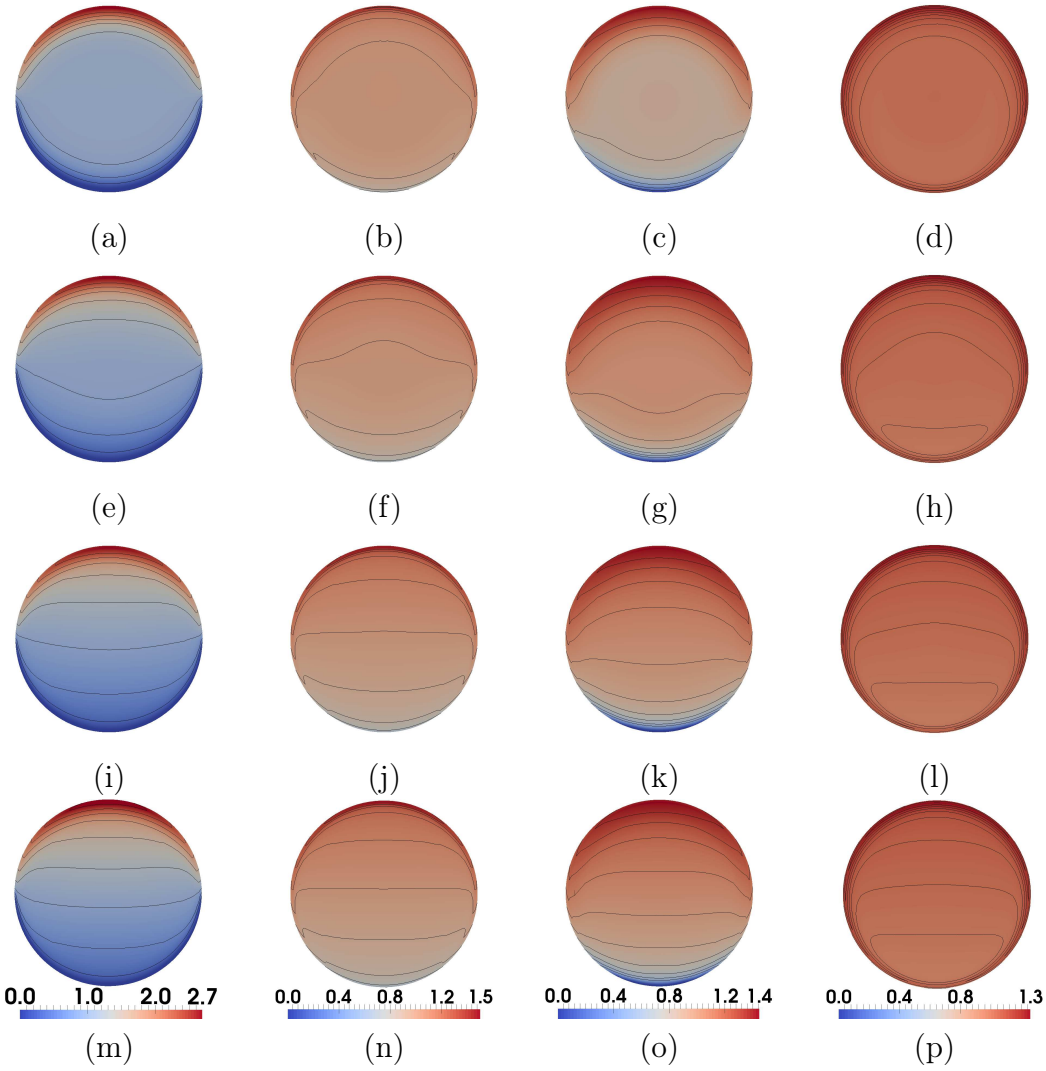

Figure 5.9 Maps of the normalized ice fraction ϕ/Φ_m, at different z-coordinate locations (a-d: $z/L = 1/9$, e-h: $z/L = 2/9$, i-l: $z/L = 1/3$ and m-p: $z/L = 4/9$) and for four different inlet conditions (U_m and Φ_m): (a,e,i,m) $\Phi_m = 0.1$, $U_m = 0.5\ m.s^{-1}$, (b,f,j,n) $\Phi_m = 0.1$, $U_m = 2\ m.s^{-1}$, (c,g,k,o) $\Phi_m = 0.25$, $U_m = 0.5\ m.s^{-1}$, (d,h,l,p) $\Phi_m = 0.25$, $U_m = 2\ m.s^{-1}$.

Still for the cases with $\Phi_m = 0.25$, thin concentration peaks appear with the velocity increase both at bottom and top walls. Explanations for this phenomenon have not been clarified. Physically, two points may be put forward: (i) the secondary flow occurring in the pipe cross-section (discussed afterwards, see Figure 5.13 notably) could drain the particles towards the walls and maintain them in the peripheral region. This is particularly visible on Figure 5.9m,n,o,p. The study of [Zhang and Acrivos, 1994] had shown that the

secondary flow impacts the particle concentration field especially close to the walls; (ii) it was seen in section 4.3.4 that the flux N_μ due to spatial viscosity variation (the whole equation term is called D_μ in section 4.3) seems to be the origin of a near wall particle filling. One sees that the more the velocity increases the more the peaks are noticeable, which is an expected effect of D_μ since near wall shear rate increases too. Such near wall peaks were already numerically observed in the studies of [Morris and Brady, 1998; Nott and Brady, 1994], although they used the suspension-balance model. In the near wall region, scale issues related to particle size or smooth shear rate predictions (see [Morris and Brady, 1998]) can easily be the cause of simulation errors there. In [Nott and Brady, 1994]'s modelling, wrong wall conditions resulted in those concentration peaks.

The variations of the ice concentration are presented in Figure 5.9 for four sets of parameters (U_m, Φ_m) and axial positions from $z/L = 1/9$ to $z/L = 4/9$. Note that for larger values of z/L, the ice concentration contours are similar and the flow may be considered as fully developed. Figure 5.9 highlights in particular the predominant influence of buoyancy, inducing an agglomeration of ice particles at the top of the pipe. Buoyancy − or more generally, the stratification caused by the particle settling − was analysed in details in Section 4.3. For $\Phi_m = 0.1$ and $U_m = 0.5\ m.s^{-1}$, the maximum ice fraction is around 2.7 times larger than the inlet ice concentration at the top of the pipe, while the fluid is purely liquid in the bottom. Keeping the inlet axial velocity constant but imposing $\Phi_m = 0.25$ leads to similar results but the maximum ice fraction is only $1.4\Phi_m$. For a higher velocity $U_m = 2\ m.s^{-1}$, the ice concentration is more uniform within a given cross-section and especially for $\Phi_m = 0.25$. ϕ is relatively uniform with still a maximum value at the top. The ice concentration does not vary much with z/L for the four sets of parameters and its distribution in such (r, θ) planes is clearly non axisymmetric apart from the last case ($\Phi_m = 0.25$, $U_m = 2\ m.s^{-1}$).

Another way to investigate the axial development of the ice concentration field is to look at the stratification parameter S introduced by [Darbouret, 2005]. The parameter S is defined as:

$$S = \frac{\phi_{max} - \phi_{min}}{\phi_m} \tag{5.8}$$

where ϕ_m is the maximum ice packing factor fixed to $\phi_m = 0.637$ as suggested by [Barnes *et al.*, 1989a].

Figure 5.10 presents the axial distributions of the stratification parameter S for the eight inlet flow conditions considered by [Kitanovski and Poredoš, 2002]. For all conditions, the parameter S remains rather constant with the axial distance z from the pipe inlet

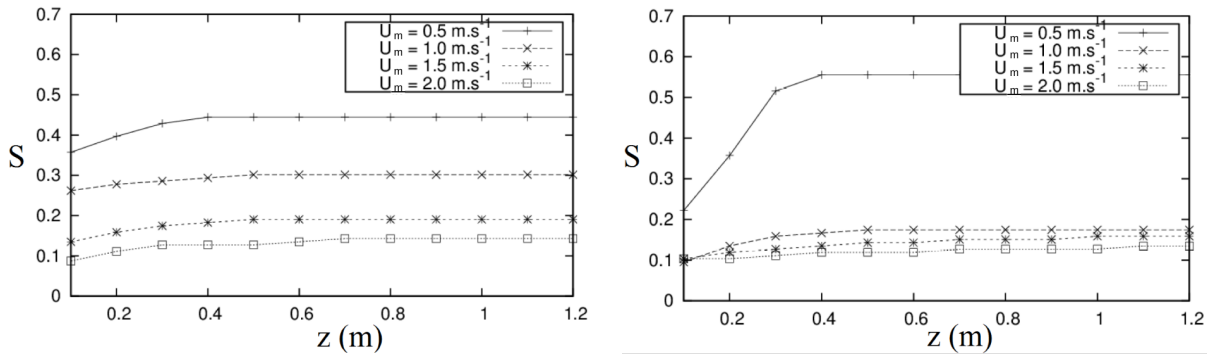

Figure 5.10 Axial distributions of the stratification parameter S for (a) $\Phi_m = 10\%$ and (b) $\Phi_m = 25\%$. Results obtained for four inlet axial velocities U_m.

revealing that the ice concentration field gets fully established for $z/L \geq 2/9$ ($z = 0.4$ m). For $\Phi_m = 0.1$ and $U_m = 0.5m.s^{-1}$ (considered as a very heterogeneous flow, or stratified flow #2), the fluid close to the bottom wall is purely liquid with no ice particles ($\phi_{min} = 0$) and S tends then to $S = 0.44$. A similar profile is observed for the possibly stationary bed flow ($\Phi_m = 0.25$ and $U_m = 0.5m.s^{-1}$) with S tending to $S = 0.55$. For other flows (less heterogeneous and even homogeneous), S decreases both with increased values of U_m or Φ_m and remains below $S \leq 0.2$. For $\Phi_m = 0.1$ and $U_m = 1m.s^{-1}$, where S is slightly above 0.3, the flow remains very heterogeneous (see figure 5.7b). The ice concentration field is rapidly independent from the axial position for less heterogeneous flow regimes ($S \leq 0.2$). Note that the asymptotic value $S = 0$ corresponding to a fully homogeneous flow can not be observed using the present model due to the repelling phenomenon near wall and more generally to wall effects. With replacing ϕ_m by ϕ_{max} in Equation 5.8, the transition from moving bed to heterogeneous flows is more visible and appears as soon as $S \neq 1$ or $\phi_{min} \neq 0$.

5.3.2 Hydrodynamic flow field

The ice concentration fields are not sufficient to clearly identify the different flow regimes and a critical insight into the hydrodynamic flow field is also required. Figure 5.11 displays some maps of the average axial velocity u at different (r, θ) planes along the pipe axis for four set of inlet conditions. Note that the two other velocity components are two orders of magnitude lower and so are not displayed here. From Figure 5.11, the axial evolution of u appears to be moderate for all operating conditions. For any ice concentration, the hydrodynamic boundary layer is much thicker for $U_m = 0.5\ m.s^{-1}$ compared to the cases with $U_m = 2\ m.s^{-1}$. The maximum value of u is slightly shifted below the pipe axis at low inlet velocities, leading to an asymmetric distribution of the axial velocity component. On

the contrary, for $U_m = 2\ m.s^{-1}$, the distribution appears rather symmetric. Increasing the inlet ice concentration leads to a thickening of the hydrodynamic boundary layer along the wall and by conservation of mass to an increase of the maximum axial velocity.

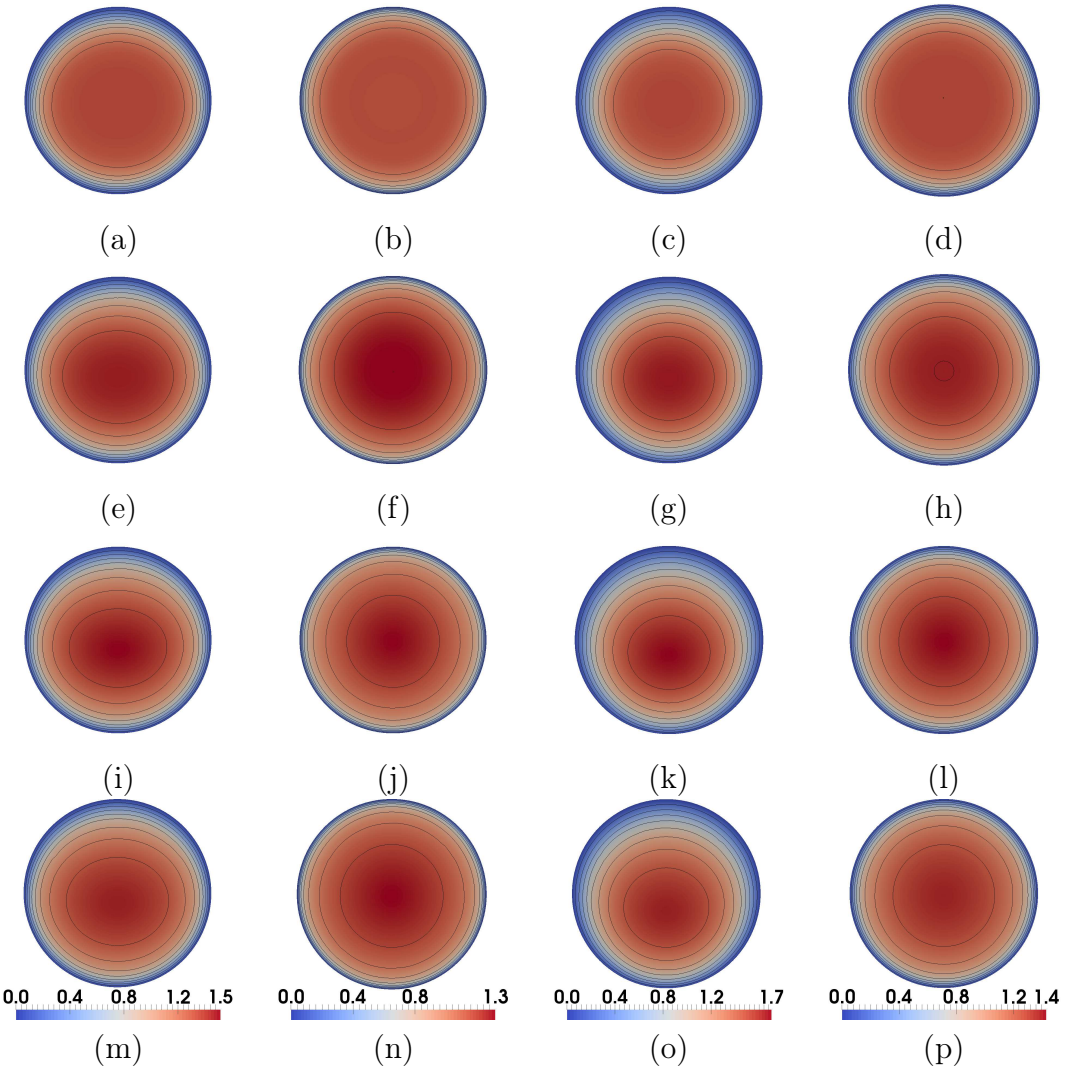

Figure 5.11 Maps of the normalized average axial velocity component u/U_m at different z-coordinate locations (a-d: $z/L = 1/9$, e-h: $z/L = 2/9$, i-l: $z/L = 1/3$ and m-p: $z/L = 4/9$) and for four different inlet conditions (U_m and Φ_m): (a,e,i,m) $\Phi_m = 0.1$, $U_m = 0.5\ m.s^{-1}$, (b,f,j,n) $\Phi_m = 0.1$, $U_m = 2\ m.s^{-1}$, (c,g,k,o) $\Phi_m = 0.25$, $U_m = 0.5\ m.s^{-1}$, (d,h,l,p) $\Phi_m = 0.25$, $U_m = 2\ m.s^{-1}$.

To have a more quantitative insight into the mean hydrodynamic field, Figure 5.12 presents some radial profiles of the average axial velocity for the eight sets of parameters. For $U_m = 1\ m.s^{-1}$, the radial distributions of the average axial velocity remain rather the same for $0.2 \leq z/L \leq 1$, which means that the velocity profile is not influenced by the local ice concentration. By comparing the profiles obtained for $\Phi_m = 0.1$ and $\Phi_m = 0.25$,

the main difference lies in the thickness of the hydrodynamic boundary layers. These are thinner at low ice concentrations, which results in lower axial velocities around the pipe axis by conservation of mass. As in the simulations of [Onokoko and Galanis, 2013] obtained for similar inlet conditions ($U_m = 2\ m.s^{-1}$ and $0.1 \leq \Phi_m \leq 0.2$), the profiles remain almost symmetric and resemble typical Poiseuille profiles encountered for single-phase flows of Newtonian fluids in pipes. For $U_m = 0.5\ m.s^{-1}$ and $\Phi_m = 0.1$ (Fig.5.12c), a slight asymmetry is observed with higher velocities in the lower half of the pipe due to lower ice concentrations. This was also obtained by [Onokoko and Galanis, 2013] for $0.2 \leq U_m \leq 0.35\ m.s^{-1}$ and $0.1 \leq \Phi_m \leq 0.2$. On Figures 5.12c and 5.12d, the thickening of the boundary layers when the inlet axial velocity decreases is clearly visible at $z/L = 0.8$.

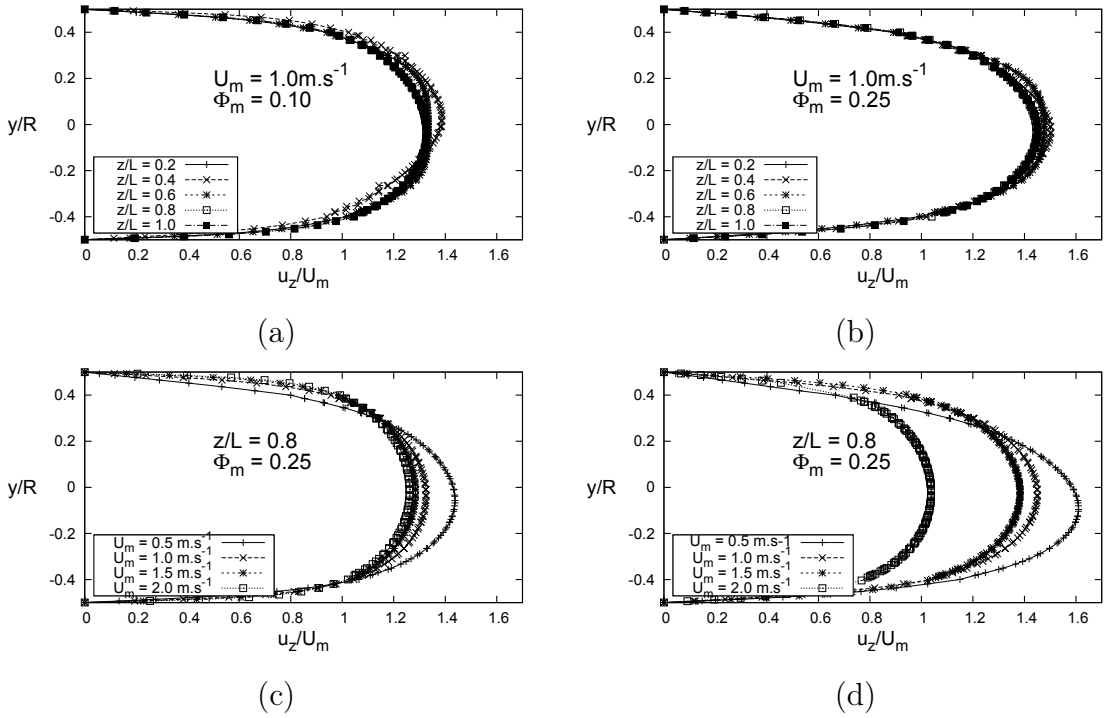

Figure 5.12 Radial distributions of the normalized axial velocity components u/U_m. Influence of the axial position z/L for $U_m = 1\ m.s^{-1}$ and (a) $\Phi_m = 0.1$ or (b) $\Phi_m = 0.25$. Influence of the inlet axial velocity U_m for $z/L = 0.8$ and (c) $\Phi_m = 0.1$ or (d) $\Phi_m = 0.25$.

Even if the main flow is axially oriented, a weaker secondary flow is usually encountered with ice slurry pipe flows (or more generally with solid-liquid flows, as also observed by [Zhang and Acrivos, 1994]). Figure 5.13 presents maps of the velocity vectors in a (r, θ) plane located at $z/L = 0.95$ for $\Phi_m = 0.25$ and two inlet velocities $U_m = 0.5$ and $2\ m.s^{-1}$. Four flow recirculations are clearly visible for the lowest velocity, which would rather be characteristic of a heterogeneous flow regime (or possibly moving bed flow regime, if slow

motion circulations are observed in the bed). Two intense large recirculations appear in the upper part of the pipe and two weaker smaller ones in the lower part. These recirculation cells are symmetric with respect to the vertical plane of symmetry. When increasing the inlet axial velocity to $U_m = 2\ m.s^{-1}$, only two symmetric recirculation cells with a lower intensity are still visible. The fluid mixture is drained downward in the middle of the pipe and by conservation of mass, upward along the walls.

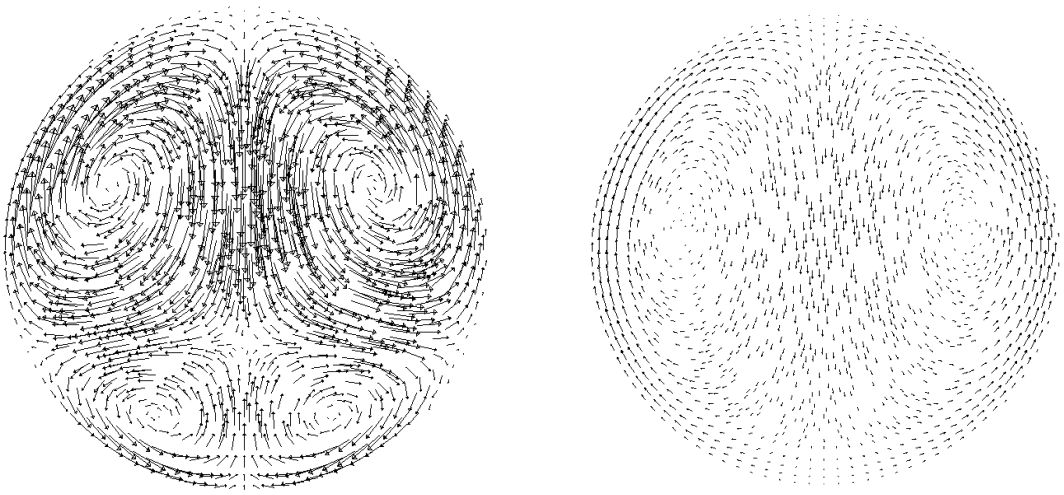

(a) (b)

Figure 5.13 Maps of the velocity vectors in a (r, θ) plane located at $z/L = 0.95$ for $\Phi_m = 0.25$ and two inlet velocity conditions: (a) $U_m = 0.5\ m.s^{-1}$ and (b) $U_m = 2\ m.s^{-1}$.

Another way to investigate the influence of the inlet parameters onto the secondary flow is to look at the distribution of the axial vorticity component ω_z. Figure 5.14 displays maps in a (r, θ) of the normalized axial vorticity component at different axial locations $1/9 \leq z/L \leq 4/9$. At $z/L = 1/9$, a four cell structure is obtained for $U_m = 0.5\ m.s^{-1}$ and $\Phi_m = 0.1$ with a symmetry according to the vertical pipe axis. On the right part for example, the two vortical structures are counter-rotating with a $\omega_z > 0$ cell in the upper right region and a $\omega_z < 0$ cell in the lower right part of the pipe. These vortices are relatively confined close to the wall. When moving towards the pipe outlet, a four cell structure remains visible but as it slightly extends towards the pipe axis ($r/R = 0$), the intensity of the vortices diminishes. Keeping the inlet velocity constant but increasing the inlet ice concentration to $\Phi_m = 0.25$ leads also to a four cell structure. In that case, two main recirculations on the top of the pipe are obtained with two smaller ones at the bottom. For increasing z/L, the recirculations are less intense and the size of the smaller cells slightly increases.

For higher inlet axial velocity $U_m = 2\ m.s^{-1}$, there is no clear evidence of either a two or

four cell structure for $\Phi_m = 0.1$. The axial vorticity component remains rather weak. One can recall that for this set of parameters, a heterogeneous flow was observed (Fig. 5.7d), close to homogeneous though. The absence of axial vorticity may be possibly a good indicator to the transition to a homogeneous flow regime. For $\Phi_m = 0.25$, only two counter-rotating cells appear at $z/L = 1/9$, extending each along the wall over the whole height of the pipe. They progressively get less intense, being more extended towards the centre of the pipe.

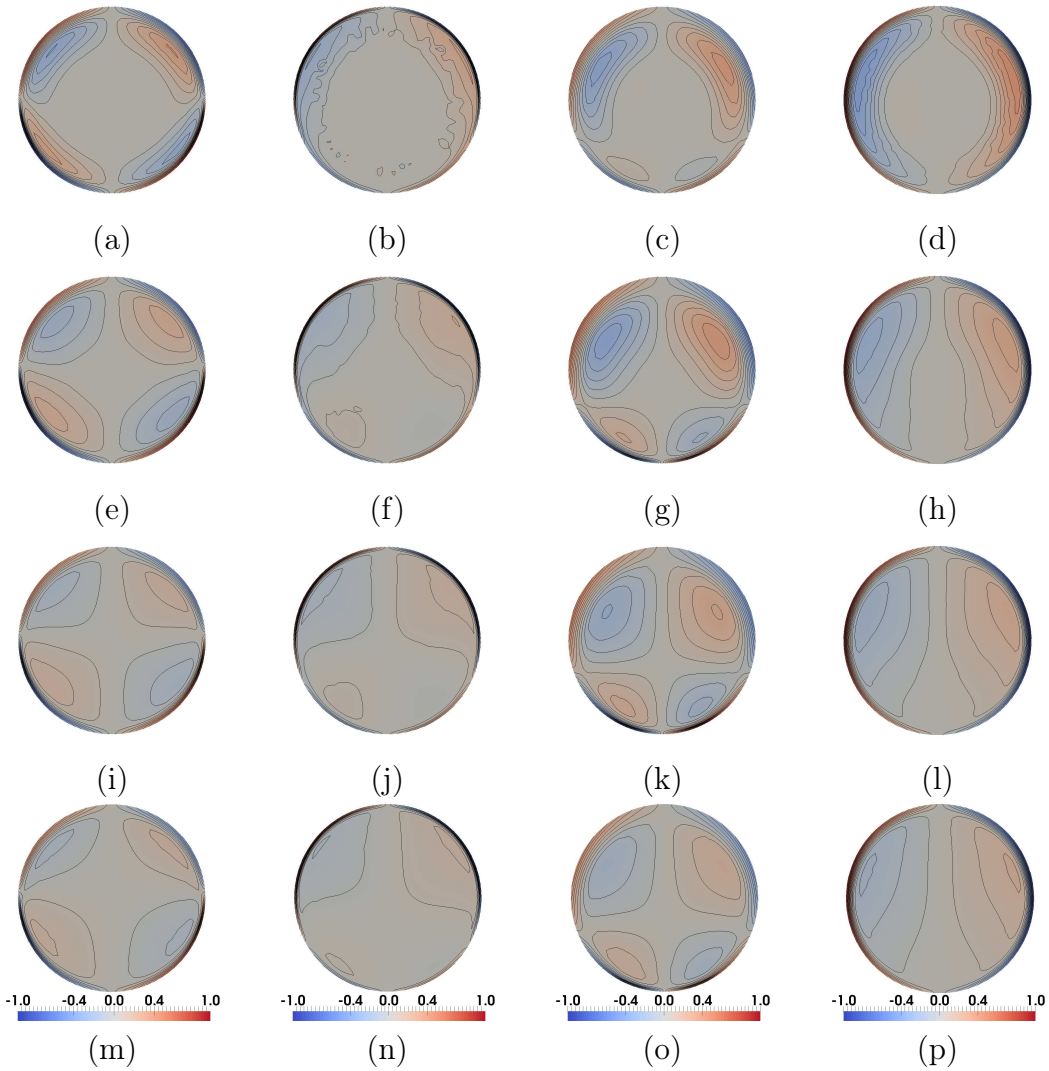

Figure 5.14 Maps of the normalized axial vorticity component $\omega_z^* = \omega_z/\omega_{z,max}$ at different z-coordinate locations (a-d: $z/L = 1/9$, e-h: $z/L = 2/9$, i-l: $z/L = 1/3$ and m-p: $z/L = 4/9$) and for four different inlet conditions (U_m and Φ_m): (a,e,i,m) $\Phi_m = 0.1$, $U_m = 0.5\ m.s^{-1}$ ($\omega_{z,max} = 5.5\ 1/s$), (b,f,j,n) $\Phi_m = 0.1$, $U_m = 2\ m.s^{-1}$ ($\omega_{z,max} = 0.8\ 1/s$), (c,g,k,o) $\Phi_m = 0.25$, $U_m = 0.5\ m.s^{-1}$ ($\omega_{z,max} = 2.9\ 1/s$), (d,h,l,p) $\Phi_m = 0.25$, $U_m = 2\ m.s^{-1}$ ($\omega_{z,max} = 1.2\ 1/s$).

Concerning the turbulent flow field, Figure 5.15 displays maps of the turbulence kinetic energy k ($m^2.s^{-2}$) at different z-coordinate locations for four inlet operating conditions. Note that the distribution of k does not evolve for $z/L \geq 4/9$. The turbulence kinetic energy does not seem to be very sensitive to the inlet ice concentration. For $U_m = 0.5m.s^{-1}$ and $\Phi_m = 0.1$, the flow is laminar close to the pipe inlet ($z/L = 1/9$). Turbulence progressively appears when moving towards the pipe outlet. The maximum values for k are observed around $r/R \simeq 0.65$ at $z/L = 2/9$ and by diffusion, turbulence kinetic energy increases around the pipe axis. At $z/L = 4/9$, a small region close to the axis remains laminar. The boundary layer, which is thinner at the bottom of the pipe, remains laminar. A similar behaviour is observed by increasing Φ_m to 0.25, while keeping the same value of $U_m = 0.5m.s^{-1}$. Nevertheless, the asymmetry is more pronounced, the local maximum for k at $z/L = 2/9$ is shifted to $r/R \simeq 0.55$ and the laminar boundary layer is thicker.

For $U_m = 2\ m.s^{-1}$, the distribution of the turbulence kinetic energy is more axis-symmetric. The boundary layer thickness is thinner compared to the previous cases. As already mentioned, it increases with the ice concentration. Though the inlet velocity is 4 times higher, a small flow region remains laminar around the axis at $z/L = 4/9$ whatever Φ_m. As expected, the maximum value of k is increased by increasing U_m from $k_{max} = 4 \times 10^{-3}$ $m^2.s^{-2}$ for $U_m = 0.5\ m.s^{-1}$ to around $k_{max} = 5 \times 10^{-2}\ m^2.s^{-2}$ for $U_m = 2\ m.s^{-1}$ but is not sensitive to the inlet ice concentration. This is rather strange since ice concentration augmentation would also increase mixture viscosity μ_{is} and would then limit turbulence.

Still on Figure 5.15, one can see an area of less turbulence kinetic energy close to the cross-section centre. This area gets lower with velocity decrease (see subfigures (p) and (o) or (n) and (m) for instance) which, as expected, corresponds to the region where the velocity maximum is reached (known to be a region of very weak shear rate $\dot{\gamma}$). The lowering of this region is particularly remarkable on Figure 5.12d. The very interesting point here lies in the fact that, in the experimental part, similar phenomenon was observed: a non-sheared ice particle layer appears around pipe mid-height and tends to lower with decreasing velocity. Thus, with an appropriate rheological model accounting for the viscoplastic character of ice slurries, one could have reproduced the emergence of the non-sheared rigid layer, lowering with the velocity decrease.

5.3.3 Pressure drop and friction coefficient

For engineering applications and the design of future heat exchangers using ice slurries, it may be interesting to consider the influence of the inlet parameters on the regular pressure drop ΔP or on the friction coefficient Cf. [Reghem, 2002] proposed a semi-

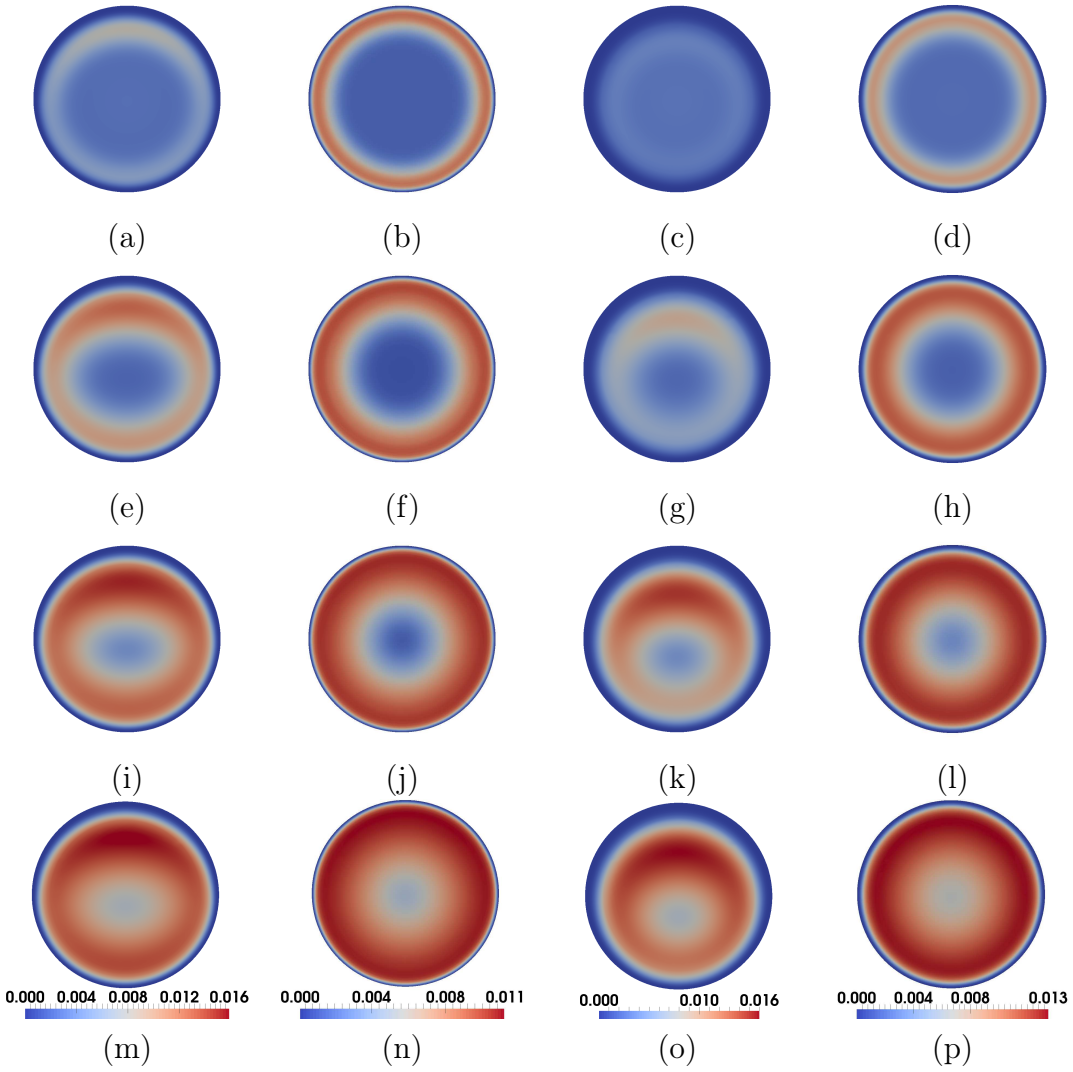

Figure 5.15 Maps of the normalized turbulence kinetic energy k/U_m^2 at different z-coordinate locations (a-d: $z/L = 1/9$, e-h: $z/L = 2/9$, i-l: $z/L = 1/3$ and m-p: $z/L = 4/9$) and for four different inlet conditions (U_m and Φ_m): (a,e,i,m) $\Phi_m = 0.1$, $U_m = 0.5\ m.s^{-1}$, (b,f,j,n) $\Phi_m = 0.1$, $U_m = 2\ m.s^{-1}$, (c,g,k,o) $\Phi_m = 0.25$, $U_m = 0.5\ m.s^{-1}$, (d,h,l,p) $\Phi_m = 0.25$, $U_m = 2\ m.s^{-1}$.

empirical relation to predict the friction coefficient Cf of ice slurry flows in tubes (same as Equation 3.5):

$$Cf = Cf_l + 9330\phi^{2.07}Cf_l^{1.963}Fr^{-0.627} \tag{5.9}$$

with Cf_l the friction coefficient for pure liquid under the same conditions deduced from classical Blasius relations and Fr the Froude number, already defined in Equation 3.4.

Equation 5.9 was obtained for $D = 25$ mm or 50 mm, $d = 0.1$ mm, $0.1 \leq \Phi_m \leq 0.3$ and $U_m \leq 4\ m.s^{-1}$ with an uncertainty of 11%. The pressure drop per unit length $\Delta P/L$ is

then evaluated from:

$$\frac{\Delta P}{L} = Cf \frac{\rho_m U_m^2}{2D} \tag{5.10}$$

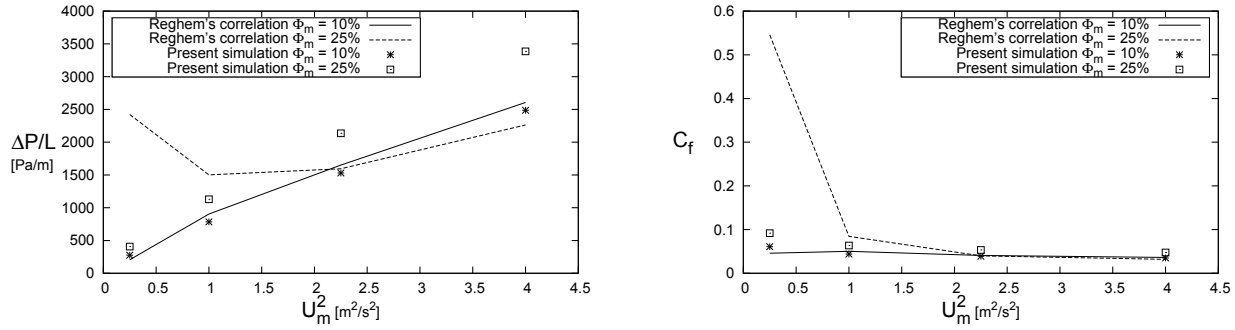

(a) (b)

Figure 5.16 Pressure drop per unit of length $\Delta P/L$ and friction coefficient Cf for the different inlet velocities U_m and two inlet ice concentrations $\Phi_m = 10\%$ and $\Phi_m = 25\%$. Comparisons between the present simulations and Reghem's formula (Eq.5.9 and 5.10). The pipe diameter is $D = 27.2$ mm.

Figures 5.16a and 5.16b present the variations with U_m^2 of the pressure drop per unit length $\Delta P/L$ and the friction coefficient Cf respectively. The present simulations obtained for two inlet ice concentrations $\Phi_m = 10\%$ and $\Phi_m = 25\%$ are compared to Reghem's formula, Equations 5.10 and 5.9. The pressure drop evaluated from the present simulations increases almost linearly with U_m^2 (Fig.5.16a). Regarding Equation 5.10, it means that Cf does not vary so much with U_m^2, which is confirmed by Figure 5.16b. As expected, the pressure drop also increases with the ice concentration because of the increased values of the dynamic viscosity of the mixture with Φ_m, in conformity with all former studies [Kauffeld *et al.*, 2005]. A good compliance with the semi-empirical correlation is observed for $\Phi_m = 10\%$. On the contrary, large differences are visible for $\Phi_m = 25\%$ at low inlet velocities $U_m \leq 1\ m.s^{-1}$. It may be firstly attributed to the difficulty to identify the transition from the laminar to the turbulent flow regimes and from heterogeneous to homogeneous flows and then to select the appropriate Blasius correlation for Cf_l. Secondly, some rheological characteristics of ice slurries (shear-thinning or shear-thickening behaviour, time-dependent properties), not taken into account in the present model, are more pronounced at low inlet axial velocities [Kauffeld *et al.*, 2005]. Contrary to what is expected from the safety diagram of [Snoek, 1993] (Figure 5.1a), there is no critical pressure drops observed in the present numerical results, which could suggest not to use ice slurries for these inlet conditions.

5.4 Brief summary

The numerical model has been here extended confidently to model ice slurry flows for eight different operating conditions. A numerical benchmark of four turbulence closures showed first the superiority of all models based on the specific dissipation rate ω. The RNG k-ε predicted a more homogeneous concentration profile due to high turbulence kinetic energy k levels, which enhance the turbulent dispersion through all the pipe section. It was found that such behaviour is mainly due to an over-dissipation of k in the viscous sublayer. To enrich the discussions, the results were then compared to the analytical model of [Kitanovski and Poredoš, 2002] for eight sets of parameters. Though the latter model does not account for the pipe geometry, 3D flow effects nor the diffusion due to direct particle-particle interactions, it provided similar concentration profiles in the bulk region. The present 3D simulations revealed flow recirculations over the pipe cross-section and non-negligible near-wall effects. Some classical flow regimes seemed to appear and certain characteristics observed through the experimental part could be found again numerically. The friction factor appeared rather constant for this range of operating conditions, while the pressure drop increases quadratically with U_m and slightly with Φ_m.

CHAPTER 6

ENGLISH CONCLUSION

This research project proposed to fulfil several objectives with the common goal of providing a better insight into ice slurry flow dynamics under isothermal conditions. These objectives were comprised into two principal parts: experimental and numerical. The first objective was to experimentally observe the ice slurry flow patterns in a horizontal straight pipe in order to establish direct correlations between these patterns and some quantitative flow data (flow velocity, ice concentration and pressure drops). The second objective was to develop and validate an original numerical model to represent ice particle transport across two-phase flows. Based on this model, ice slurry flows in a horizontal straight pipe were studied in details so that several important hydrodynamic features could be bring out. The third objective was the term by term decomposition of the particle transport equation, so as to thoroughly take a look at how the model works and reacts with the variation of relevant flow parameters (flow velocity, particle concentration and diameter) and eventually to determine the physical mechanisms governing the particle distribution.

6.1 Main discoveries and progresses

From the experimental work, a new classification for ice slurry flow patterns was established from flow visualisations, with original features concerning the ice slurry structures and their evolution. Three principal patterns were revealed: homogeneous, stratified and annular (or column) flows, for which some declinations have been highlighted. Presently, stratified flow implies a flow made of several distinct layers (or strata), occurring with or without a phase separation. In this flow regime, a compact ice layer generally appears, flows near the pipe central axis and tends to be lowered as the flow velocity decreases. In some cases, the existence of certain flow patterns only relates on the mean ice volume fraction within the flow: annular for $\Phi_m > 12\%$, stratified #2 and #3 for $\Phi_m < 10\%$. Also, despite the fact that the regime transitions mainly depend on a velocity variation, the use of transition criteria based on the critical deposition velocity or the Froude number Fr remains highly uncertain.

Pressure drops were measured simultaneously with the flow visualisations in order to link the flow regimes to the pressure drop variations. Interestingly, the flow pattern changes do not have any clear impact on the pressure drops most of the time. Albeit, two distinct

behaviours in terms of ice volume fraction level seemed to emerge around $\Phi_m \simeq 10-12\%$, as it was already shown with the flow patterns. To name one of the various differences, at $\Phi_m > 12\%$, a slight gap in terms of pressure drop was measured while transiting from annular to stratified flows. It was not observed at $\Phi_m < 10\%$. From the friction coefficient evolution, the laminarization phenomenon was confirmed and, while it usually occurs in homogeneous flows, such a phenomenon may also occur through stratified flows. Thus, the existence of a stratified flow does not necessarily imply a laminar character − one region of the flow could remain turbulent indeed. Reversely, several flows showing many recirculations by direct visualisations do not seem to present a turbulent character quantitatively speaking (i.e. friction factor evolution).
The pressure drops of the flowing ice slurries through 90°-bends and T-junctions were found to be similar in their evolution to those measured in the straight pipe for ice volume fractions up to $\Phi_m = 12.2\%$. For $\Phi_m = 18\%$, significantly higher pressure drops were measured, leading to high pumping powers, as well as a very different pressure drop evolution. At this high ice fraction, the compact ice structures probably need much more energy to flow through various obstacles (compared to the straight pipe case). Paradoxically, many consecutive bends along a refrigeration loop can create a certain flow agitation when the flow rate increases, preventing ice particles from coalescing − for $\Phi_m = 12.2\%$ possibly.

In the numerical work, an original modelling was implemented in order to model isothermal solid suspension flows and, by extension, ice slurry flows. The constitutive equation of [Phillips *et al.*, 1992] was used as a basis to model the transport of solid particles within the flowing mixture. The main features added to [Phillips *et al.*, 1992]'s model account for the sedimentation and turbulent dispersion of the particles.

Primarily, the numerical model was validated against the experimental data obtained from two different solid suspension flows, and against the velocity measurements of an ice slurry flow. A very good conformity was obtained in all cases. The model together with a low-Reynolds number SST $k-\omega$ turbulence closure improved the simulations of [Wang *et al.*, 2013a] who used a two-phase Euler-Euler model coupled to a standard $k-\varepsilon$ closure. This highlights the preponderant importance of the turbulence model compared to the single- or two-phase modelling method. In addition, the present model also requires less computational efforts than that of [Wang *et al.*, 2013a] since the conservations of mass and momentum are only solved for the mixture. In fact, the relative simplicity of the present modelling as well as the fact that it only accounts for the relevant mechanisms acting on particle motion makes it both accurate and efficient.

Then, a detailed insight into the various phenomenon acting on the particle motion across slurry flows (i.e. solid suspension flows) was provided. This was done through the budget analysis of the original modelling previously developed, which attempts to account for the different mechanisms governing the particle transport. For the considered flows, the role played by D_μ and D_c − the transport mechanisms due to the viscosity variation for the former and to the particle collision frequency variation for the latter − was principally perceptible near the pipe walls. This location is often subject to high shear rates and high shear rate gradients, which explains that these two terms (shear-induced particle migration) have a strong effect there. Moreover, D_c appeared to be the origin of the particle repelling phenomenon, which seems to be rebalanced by D_μ mostly. This last phenomenon is essential as it creates a near wall layer of lesser particle concentration which influences the entire flow dynamics. The role played by the turbulent agitation on the particle dispersion (term D_t) allows to counter the particle sedimentation (term F_b) and thus yields to the particle resuspension in more agitated flows (i.e. at higher Reynolds numbers). It was confirmed that a correct turbulence modelling is *a priori* essential to obtain the right particle concentration profile (on which directly depends the flow dynamics). Otherwise, when F_b becomes weaker, relatively to D_t, the latter seems rebalanced by F_c (the particle transport due to the fluid motion). In this case, the flow is often homogeneous. The particle transport terms seem to form couples, that is to say, two terms that compensate each other according to their respective effects (particle filling or emptying). Moreover, the terms of one couple would rather act at similar scales (for instance, the couple formed by D_c and D_μ only acts at the particle scale).

Secondly, the numerical model has been confidently extended to predict ice slurry flows under various operating conditions. A numerical benchmark of four turbulence closures showed the superiority of the models based on the specific dissipation rate ω for the considered flows. The RNG $k-\varepsilon$ predicted a more homogeneous concentration profile due to higher turbulence kinetic energy levels, which enhanced the turbulent dispersion over the whole pipe cross-section. The results were then compared to the analytical model of [Kitanovski and Poredoš, 2002] for eight sets of parameters. Although the latter model does not account for the pipe geometry, nor 3D flow effects, nor the diffusion due to direct particle interactions, it provided close ice concentration profiles in the bulk region. The present 3D simulations revealed flow recirculations over the pipe cross-section and significant near wall effects (the particle repelling phenomenon could be observed again). Furthermore, some flow regimes were modelled. This was very clear for homogeneous and heterogeneous flows, but doubts remained concerning moving bed flows (that would theoretically require the use of non-Newtonian models).

6.2 Future investigations and applications

Three research axes are proposed here for future investigations. These seem necessary in order to reach a good knowledge of ice slurry flows or to succeed in their modelling.

- The next step would be that experimental studies using advanced techniques provide local velocity and ice fraction profiles in order to precisely characterize the flow regimes that were depicted here. For this purpose, ultrasonic Doppler velocimetry (see [Vuarnoz *et al.*, 2002] notably) appears to be an appropriate method to capture the mean flow field, the turbulent flow field or the ice concentration field over the entire pipe cross-section area. It would also be advisable to carry out further research over more complex ice slurry piping systems (where flowing issues are likely to emerge). These local measurements are absolutely necessary to further validate advanced numerical models dedicated to ice slurry flows.

- Future numerical simulations will have to take into consideration the rheological behaviour of ice slurry. This is of prime importance in order to reproduce the different flow patterns observed throughout the experiments. Although little applied in the present context, the Cross model may reveal to be efficient to describe the rheological behaviour of ice slurry flows at lower shear stresses, whereas the Herschel-Bulkley model as proposed by [Trabelsi *et al.*, 2017] cannot render a finite apparent viscosity. So, additional experimental data will be needed for the determination of the rheological parameters. In fact, a major issue with ice slurries concerns the various additives used to lower the fusion point of water, as these also influence the flow rheology a lot.

- $k-\omega$ turbulence models have demonstrated their efficiency for circular pipe flows. What will be observed with other piping geometries, such as rectangular, squared or elliptical shapes? Turbulence benchmarks have to be done for other types of cross-section geometries.

  Lastly, one important aspect of turbulence was neither addressed nor modelled in this work: the turbulence modulation (see [Balachandar and Eaton, 2010] notably). According to the particle size and the particle concentration, the turbulence intensity and the eddy scales may completely change. This strongly impacts both the particle distribution and the whole flow dynamics.

  In any solid suspension flows involving phase change, and in ice slurry flows in particular, there is not a single particle size. To account for a realistic particle size distributions, the present model could be coupled to a Population Balance Model (PBM) as done recently by [Xu *et al.*, 2018].

Eventually, large eddy simulations could also be considered to highlight the possible appearance of 3D coherent structures, that were clearly recognisable through the flow visualisations.

Besides, studies are now conducted to assess the applicability of ice slurries to mine cooling. First, the two-phase mixture production could be natural and renewable with using the negative temperatures of the air (in cold countries during the winter, such as Canada, Russia...). Second, the advantages are that (i) the ice slurry can be transported on long underground distances and (ii) the latent heat of fusion enables to extract very large amounts of heat in confined locations.

The model developed in the present research project intended to be specifically applied to ice slurry flows. However, the way it was built allows for further usage with all kind of solid suspension flows (according to some conditions of applicability: particle size and shape, flow regime, adiabatic flow). It may reliably be extended to other phase change materials [Zhang and Ma, 2012].

CHAPTER 7

CONCLUSION FRANÇAISE

Le principal objectif de ce travail était l'approfondissement des connaissances concernant l'hydrodynamique des coulis de glace dans des conditions isothermes. Une étude combinant expériences et modélisations numériques a donc été entreprise. Le premier objectif spécifique était l'observation expérimentale des régimes d'écoulement des coulis de glace en conduite droite et horizontale afin d'établir des corrélations directes entre ces régimes et les principaux paramètres d'opération (vitesse d'écoulement et concentration de glace moyennes, ou pertes de charge). Le deuxième objectif spécifique était de développer et valider un modèle numérique original pour représenter le transport des particules de glace au sein du mélange. À partir de cette modélisation, plusieurs cas d'écoulements de suspensions particulaires dont les coulis de glace ont été modélisés pour une conduite circulaire horizontale. Une décomposition terme par terme de l'équation de transport des particules a été faite afin d'établir précisément comment le modèle réagit en fonction de la variation de paramètres tels que le débit, la concentration et le diamètre des particules et enfin de déterminer les mécanismes physiques à l'œuvre dans la répartition des particules.

7.1 Principales avancées

À partir des travaux expérimentaux, une classification nouvelle des régimes d'écoulements de coulis de glace fut établie. Notamment, la visualisation directe de l'écoulement a permis de mettre en avant de nouvelles structures d'écoulement de coulis de glace ainsi que leur évolution. Trois régimes principaux ont été identifiés : écoulement homogène, stratifié et annulaire (ou en colonne), pour lesquels des déclinaisons apparaissent. Dans sa dénomination actuelle, stratifié signifie simplement que l'écoulement est constitué de plusieurs couches (ou strates) − cela n'impliquant pas forcément une séparation des phases. Généralement, l'écoulement stratifié d'un coulis de glace présente une couche compacte, à mi-hauteur environ, qui tend à s'abaisser avec une réduction du débit. Dans certains cas, l'existence de régimes d'écoulement semble dépendre seulement de la concentration moyenne en glace: le régime annulaire n'est observé que pour $\Phi_m > 12\%$, tandis que les régimes stratifiés #2 et #3 ne le sont que pour $\Phi_m < 10\%$. Bien que le passage d'un régime à un autre s'effectue principalement suite à une variation du débit, aucun critère

objectif (vitesse critique de déposition particulaire ou nombre de Froude Fr) pour marquer la transition d'un régime à un autre n'existe encore à ce jour.

Parallèlement à la visualisation des régimes d'écoulement, les pertes de charge ont été mesurées afin de les relier aux régimes d'écoulement. Étonnament, les changements de régime n'ont souvent pas de répercussions claires sur la perte de charge. Toutefois, deux comportements distincts semblent apparaître pour des concentrations moyennes de glace situées au-dessus et en dessous de $\Phi_m \simeq 10 - 12\%$. Le même constat avait été fait avec l'observation des régimes d'écoulement. Par exemple, au-dessus de 12% de glace, les pertes de charge marquent un seuil qui correspond au passage de l'écoulement d'annulaire à stratifié; cela n'est cependant pas observé en dessous de 10% de glace. Avec l'évolution du coefficient de frottement, le phénomène de re-laminarisation a été confirmé et, bien que celui-ci se produise habituellement au sein d'écoulements homogènes, un tel phénomène peut aussi s'observer pour un écoulement stratifié. L'existence d'un écoulement stratifié n'implique pas automatiquement une nature laminaire de l'écoulement. De même, certains écoulements présentant visiblement de nombreuses recirculations semblent quantitativement se comporter de manière laminaire.
Les pertes de charge d'un coulis de glace s'écoulant au travers de coudes droits et de jonctions en T évoluent de manière similaire aux pertes de charge dans une conduite droite et horizontale pour des fractions de glace allant jusqu'à $\Phi_m = 12.2\%$, et non plus $\simeq 10\%$. Pour $\Phi_m = 18\%$, des pertes de charge beaucoup plus importantes ont été mesurées, induisant des puissances de pompage très élevées. À ce niveau de concentration de glace, les structures compactes de glace demandent probablement bien plus d'énergie (relativement à une conduite droite) pour traverser les différents singularités géométriques. Paradoxalement, de nombreuses singularités le long d'un circuit de réfrigération peuvent créer une certaine agitation de l'écoulement (advection chaotique) empêchant les particules de glace de former des bouchons − comme il pourrait s'avérer être le cas à $\Phi_m = 12.2\%$.

Dans la partie numérique, un ensemble original d'équations a été implémenté pour modéliser les écoulements de suspensions particulaires et, plus particulièrement les coulis de glace, en conduite circulaire pour des conditions isothermes. L'équation constitutive de [Phillips *et al.*, 1992] a été choisie comme base du modèle pour le transport des particules solides au sein du mélange. Les principaux éléments qui y ont été ajoutés tiennent compte de la sédimentation et de la dispersion turbulente des particules. En premier lieu, le modèle numérique a été validé à partir de données expérimentales, provenant de deux cas d'écoulements de suspensions particulaires et de deux cas d'écoulements de coulis de

glace. Une très bonne concordance fut obtenue pour chacun, que ce soit sur des profils de vitesse ou de concentration particulaire. La modélisation actuelle, associée au modèle de fermeture $k-\omega$ SST à bas nombre de Reynolds dans le cadre d'écoulements turbulents, améliore sensiblement les simulations de [Wang *et al.*, 2013a] qui utilisaient un modèle diphasique Euler-Euler couplé au modèle $k-\varepsilon$ standard. Ceci montre l'importance première du choix du modèle de turbulence, lequel semble même prévaloir sur la prise en compte ou non du caractère diphasique du coulis. De plus, le coût de calcul est présentement amoindri par rapport à [Wang *et al.*, 2013a], les conservations de la masse et du moment étant résolues seulement pour le mélange. Autrement, les divers phénomènes agissant sur le déplacement des particules au travers même des écoulements de coulis ont été analysés en détails via une analyse terme à terme du modèle original précédemment développé pour rendre compte des mécanismes régissant le transport particulaire. Pour les écoulements considérés, le rôle joué par D_μ et D_c − transports particulaires dus respectivement à la variation de viscosité et à la variation de fréquence de chocs inter-particulaires − était principalement perceptible en proche paroi. Cette zone est le plus souvent soumise à un fort cisaillement et à une importante variation spatiale du cisaillement, ce qui explique que ces deux termes (∼migration particulaire induite par un cisaillement) y aient des effets très marqués. De plus, D_c se révèle être à l'origine du phénomène de répulsion particulaire, lequel semble surtout rééquilibré par D_μ. Ce phénomène est essentiel car il permet de créer une couche moindrement concentrée en proche paroi qui influe sur toute la dynamique de l'écoulement. Le rôle joué par l'agitation turbulente sur la dispersion particulaire (terme D_t) s'oppose à la sédimentation (terme F_b) et ainsi aboutit à la re-suspension des particules au sein d'écoulements plus agités (c'est-à-dire avec Re plus élevé). Il a été établi qu'une modélisation précise de la turbulence est *a priori* essentielle pour l'obtention du profil exact de concentration particulaire duquel dépend directement la dynamique de l'écoulement. Autrement, quand F_b devient plus faible, relativement à D_t, ce dernier semble dès lors rééquilibré par F_c, le transport particulaire entraîné par l'écoulement moyen. Dans ce cas-ci, l'écoulement est souvent homogène. Les termes de l'équation de transport des particules tendent à former des paires, c'est-à-dire deux termes qui se compensent mutuellement selon leurs effets respectifs (remplissage ou vidage de particules) et qui agissent à la même échelle spatiale. Par exemple, le couple formé D_c et D_μ agit à l'échelle d'une particule.

En second lieu, le modèle numérique a été appliqué avec confiance à la prédiction d'écoulements de coulis de glace pour différents régimes d'écoulements. Un benchmark numérique de différents modèles de turbulence a démontré la supériorité des équations fondées sur le taux de dissipation spécifique ω pour des écoulements en conduite circulaire. Le modèle $k-\varepsilon$

RNG prédit quant à lui un profil de concentration plus homogène, dû à des niveaux élevés d'énergie cinétique turbulente k qui renforcent la dispersion turbulente des particules. Les résultats issus du modèle $k-\omega$ SST ont été ensuite comparés au modèle analytique de [Kitanovski and Poredoš, 2002] pour huit jeux de paramètres d'entrée (U_m,Φ_m). Bien que ce dernier modèle ne tienne compte ni de la géométrie de la conduite, ni de la diffusion des particules, il prédit des profils de concentration en glace proches de ceux obtenus avec le présent modèle dans le coeur de l'écoulement. Les simulations 3D actuelles ont révélé également des écoulements secondaires au sein de la conduite et des effets en proche paroi non-négligeables.

7.2 Recherches futures

Trois axes sont présentés. Ils semblent déterminants pour l'obtention d'une très bonne connaissance des écoulements de coulis de glace ou pour parvenir à les modéliser de manière plus précise.

- Des études expérimentales incorporant des techniques de mesures avancées sont désormais nécessaires pour déterminer les profils locaux de vitesse et de concentration de glace afin de caractériser très précisément les régimes d'écoulement qui ont été décrits et afin d'acquérir des données fiables pour une exacte validation des modèles numériques. Dans cette optique, la vélocimétrie Doppler par ultrasons (voir [Vuarnoz *et al.*, 2002] notamment) apparaît comme une méthode attrayante quant à la mesure des champs de vitesse moyen et turbulent et de la concentration en glace. Les travaux de recherche doivent également être poursuivis sur les écoulements de coulis de glace au travers de géométries complexes et plus représentatives des installations de climatisation existantes notamment.

- Les prochaines simulations numériques devront prendre en compte le comportement rhéologique des coulis de glace. Ceci est nécessaire à la reproduction des différents régimes d'écoulement observés à partir des expériences. Le modèle de Cross semble être le modèle le plus approprié pour décrire le comportement rhéologique des coulis de glace à faibles contraintes de cisaillement τ alors que le modèle de Herschel-Bulkley, largement utilisé pour les coulis, ne peut reproduire une viscosité apparente finie μ_0. Néanmoins, de nombreuses données expérimentales seront de nouveau requises pour déterminer les 4 paramètres du modèle de Cross.

– Les modèles de turbulence de type $k-\omega$ se sont montrés les plus aptes à décrire les écoulements de coulis de glace en conduite à section circulaire, mais qu'en est-il pour des sections rectangulaire, carrée ou elliptique... Des essais de modèles de turbulence doivent être conduits avec ces autres types de section. Par ailleurs, un aspect important de la turbulence n'a jamais été considéré dans le cas des coulis de glace : la modulation de la turbulence (voir [Balachandar and Eaton, 2010] notamment). Selon la taille et la concentration des particules, l'intensité de la turbulence et les échelles tourbillonnaires peuvent énormément changer. Ceci impacte fortement aussi bien la répartition des particules et l'ensemble de la dynamique d'écoulement. Les coulis de glace sont formés de particules de différentes tailles. Afin d'améliorer les prédictions des modèles, ajouter un modèle de balance de population (PBM) comme cela a été fait par [Xu *et al.*, 2018] permettrait de simuler des distributions de tailles réalistes, ce qui est primordial plus particulièrement lorsque des transferts thermiques sont en jeu. Finalement, des simulations aux grandes échelles pourraient également être considérées pour mettre en lumière l'émergence de structures 3D instationnaires.

Par ailleurs, des études sont en cours pour évaluer la possibilité d'appliquer les coulis de glace au refroidissement des mines. Premièrement, la production du mélange diphasique se ferait de manière naturelle en utilisant les températures négatives de l'air ambiant (en hiver dans les pays froids, tels que le Canada ou la Russie). Deuxièmement, les avantages sont (i) que le coulis de glace peut être transporté sur de longues distances souterraines et (ii) que la chaleur latente de fusion permet d'extraire de grandes quantités de chaleur dans des zones confinées.

Le modèle développé a été principalement appliqué au cas des coulis de glace. Toutefois, la manière dont il a été construit lui permet une utilisation plus étendue, c'est-à-dire sur tout écoulement de suspension particulaire (en respectant certaines conditions : taille et forme des particules, régime d'écoulement, isothermie). On pourrait ainsi l'étendre à la modélisation d'écoulements incluant d'autres matériaux à changement de phase [Zhang and Ma, 2012].

APPENDIX A
LIST OF PUBLICATIONS

Bordet A., Poncet S., Poirier M. and Galanis N., Flow visualizations and pressure drop measurements of isothermal ice slurry pipe flows, Experimental Thermal Fluid Science, 2018. *(corrected proofs)*

Bordet A., Poncet S., Poirier M. and Galanis N., Advanced numerical modeling of turbulent ice slurry flows in a straight pipe, Int. J. Thermal Sciences, 127, p.294-311, 2018.

Bordet A., Poncet S., Poirier M. and Galanis N., New flow regimes for propylene-glycol-based ice slurry in pipes, 12^{th} IIR Conference on Phase-Change Materials and Slurries for Refrigeration and Air Conditioning (PCM 2018), Orford (Québec), Canada, May 21-23, 2018.

Bordet, A., Poncet, S., Poirier, M. and Galanis, N. (2017). Validation d'un modèle original pour l'hydrodynamique des coulis de glace à partir d'écoulements de suspensions particulaires. In proceedings of XIIIème Colloque Interuniversitaire Franco-Québécois sur la Thermique des Systèmes, Saint-Lô, France.

Bordet, A., Poncet, S., Poirier, M. and Galanis, N. (2016). Numerical simulations of solid suspension flows in a horizontal pipe. In Proceedings of the XXIV ICTAM, Montreal, Canada.

Bordet, A., Poncet, S., Poirier, M. and Galanis, N. (2016). Numerical simulation of isothermal ice slurry flows through horizontal pipes. In Proceedings of the CSME International Congress, Kelowna, Canada.

LIST OF REFERENCES

Ashrae, Refrigerating American Society of Heating and Air-Conditioning Engineers (2013). *2013 ASHRAE Handbook: Fundamentals*. ASHRAE.

Ayel, V., Lottin, O. and Peerhossaini, H. (2003). Rheology, flow behaviour and heat transfer of ice slurries: a review of the state of the art. *International Journal of Refrigeration*, volume 26, number 1, p. 95–107.

Balachandar, S. and Eaton, J. K. (2010). Turbulent Dispersed Multiphase Flow. *Annual Review of Fluid Mechanics*, volume 42, number 1, p. 111–133.

Barnes, H. A., Hutton, J. F. and Walters, K. (1989a). *An introduction to rheology*. Elsevier, Amsterdam.

Barnes, H. A., Hutton, J. F. and Walters, K. (1989b). Chapter 7 - Rheology of Suspensions. In *An Introduction to Rheology*, Rheology Series, volume 3. Elsevier, p. 115–139.

Bellas, I. and Tassou, S. A. (2005). Present and future applications of ice slurries. *International Journal of Refrigeration*, volume 28, p. 115–121.

Blazejewski, R. (2012). Apparent viscosity and settling velocity of suspensions of rigid monosized spheres in Stokes flow. *International Journal of Multiphase Flow*, volume 39, p. 179–185.

Bordet, A., Poncet, S., Poirier, M. and Galanis, N. (2016a). Numerical simulation of isothermal ice slurry flows through horizontal pipes. In *Proceedings of the CSME International Congress, Kelowna, Canada*.

Bordet, A., Poncet, S., Poirier, M. and Galanis, N. (2016b). Numerical simulations of solid suspension flows in a horizontal pipe. In *Proceedings of the XXIV ICTAM, Montreal, Canada*.

Brennen, C. E. (2005). *Fundamentals of Multiphase Flow*. Cambridge University Press.

Brouwers, H. (2010). Viscosity of a concentrated suspension of rigid monosized particles. *Physical Review E*, volume 81, number 5, p. 1–11.

Bui, A. and Rudman, M. (2003). Modeling of viscous resuspension using a one-field description of multiphase flows. In *Proceedings of the International Conference on CFD in Minerals and Process Industries, Melbourne, Australia*.

Chhabra, R. P. and Richardson, J. F. (2008). Chapter 1 - Non-Newtonian Fluid Behaviour. In Richardson, R. and Chhabra, J., *Non-Newtonian Flow and Applied Rheology*, 2nd edition. Butterworth-Heinemann, Oxford, p. 1–55.

Christensen, K. G. and Kauffeld, M. (1997). *Heat transfer measurements with ice slurry* (Technical report). IIR, Heat Transfer Issues in Natural Refrigerants, 1–15 pp.

Danish, M., Kumar, S. and Kumar, S. (2011). Approximate explicit analytical expressions of friction factor for flow of Bingham fluids in smooth pipes using Adomian decomposition method. *Communications in Nonlinear Science and Numerical Simulation*, volume 16, number 1, p. 239–251.

Darbouret, M. (2005). *Étude rhéologique d'une suspension d'hydrates en tant que fluide frigoporteur diphasique. Résultats expérimentaux et modélisation.* Ph.D. thesis, École Nationale Supérieure des Mines de Saint-Étienne.

Darby, R. (1986). Hydrodynamics of slurries and suspensions. In *Encyclopedia of Fluid Mechanics*, volume 5. p. 49–91.

Davies, T. W. (2005). Slurry ice as a heat transfer fluid with a large number of application domains. *International Journal of Refrigeration*, volume 28, p. 108–114.

Doetsch, C. (2001). Pressure drop and flow pattern of ice slurries. In *Proceedings of the 3rd IIR Workshop on Ice Slurries, Luzern, Switzerland.* p. 53–56.

Doetsch, C. (2002). Pressure drop calculation of ice slurries using the Casson model. In *Proceedings of the 5th IIR Workshop on Ice Slurries, Stockholm, Sweden.*

Doron, P. and Barnea, D. (1993). A three-layer model for solid-liquid flow in horizontal pipes. *International Journal of Multiphase Flow*, volume 19, number 6, p. 1029–1043.

Doron, P. and Barnea, D. (1995). Experiments on the flow of solid-liquid mixtures in pipes. In *Proceedings of the 2nd International Conference on Multiphase Flow, Kyoto, Japan*, volume 2. p. 1–8.

Doron, P. and Barnea, D. (1996). Flow pattern maps for solid-liquid flow in pipes. *International Journal of Multiphase Flow*, volume 22, number 2, p. 273–283.

Doron, P., Granica, D. and Barnea, D. (1987). Slurry flow in horizontal pipes—experimental and modeling. *International Journal of Multiphase Flow*, volume 13, number 4, p. 535–547.

Egolf, P. W. and Kauffeld, M. (2005). From physical properties of ice slurries to industrial ice slurry applications. *International Journal of Refrigeration*, volume 28, number 1, p. 4–12.

Egolf, P. W., Kitanovski, A., Ata-Caesar, D., Stamatiou, E., Kawaji, M., Bedécarrats, J. P. and Strub, F. (2005). Thermodynamics and heat transfer of ice slurries. *International Journal of Refrigeration*, volume 28, number 1, p. 51–59.

Fang, Z. and Phan-Thien, N. (1995). Numerical simulation of particle migration in concentrated suspensions by a finite volume method. *Journal of Non-Newtonian Fluid Mechanics*, volume 58, number 1, p. 67–81.

Garside, J. and R. Al-Dibouni, M. (1977). Velocity-Voidage Relationships for Fluidization in Solid-Liquid Systems. *Industrial & Engineering Chemistry Process Design and Development*, volume 16, p. 206–214.

Gidaspow, D. (1994). *Multiphase Flow and Fluidization: Continuum and Kinetic Theory Descriptions*. Academic Press, London.

Gillies, R. G., Shook, C. A. and Xu, J. (2004). Modelling Heterogeneous Slurry Flows at High Velocities. *The Canadian Journal of Chemical Engineering*, volume 82, number 5, p. 1060–1065.

Grozdek, M., Khodabandeh, R. and Lundqvist, P. (2009). Experimental investigation of ice slurry flow pressure drop in horizontal tubes. *Experimental Thermal and Fluid Science*, volume 33, number 2, p. 357–370.

Guilpart, J., Fournaison, L., Lakhdar, M. A., Flick, D. and Lallemand, A. (1990). Experimental study and calculation method of transport characteristics of ice slurries. In *Proceedings of the First IIR Workshop on Ice Slurries, Yverdon-les-Bains, Switzerland*.

Hansen, T. M. and Kauffeld, M. (2000). Viscosity of ice-slurry. In *Proceedings of the 2nd IIR Workshop on Ice-Slurries, Paris, France*.

Hirochi, T., Maeda, Y., Yamada, S., Shirakashi, M., Hattori, M. and Saito, A. (2004). Flow Patterns of Ice/Water Slurry in Horizontal Pipes. *Journal of Fluids Engineering*, volume 126, p. 436–441.

Jensen, E. N., Christensen, K. G., Hansen, T. M., Schneider, P. and Kauffeld, M. (2001). Pressure drop and heat transfer with ice slurry. *Science et technique du froid*, p. 572–580.

Kapoor, B. and Acrivos, A. (1995). Sedimentation and sediment flow in settling tanks with inclined walls. *Journal of Fluid Mechanics*, volume 290, p. 39–66.

Kauffeld, M., Kawaji, M. and Egolf, P. W. (2005). *Handbook on Ice Slurries: Fundamentals and Engineering*. IIR Guides, International Institute of Refrigeration.

Kauffeld, M., Wang, M. J., Goldstein, V. and Kasza, K. E. (2010). Ice slurry applications. *International Journal of Refrigeration*, volume 33, p. 1491–1505.

Kaushal, D. R., Sato, K., Toyota, T., Funatsu, K. and Tomita, Y. (2005). Effect of particle size distribution on pressure drop and concentration profile in pipeline flow of highly concentrated slurry. *International Journal of Multiphase Flow*, volume 31, number 7, p. 809–823.

Kawada, Y., Shirakasi, M. and Takizawa, S. (1996). Characteristics of ice/water mixture flow in a branching pipe and development of an ice fraction control technique. *Journal of the Japanese Society of Snow and Ice*, volume 58, number 5, p. 405–415.

Kawaji, M. (2012). Macroscopic and Microscale Phenomena in Multiphase Energy Storage and Transport Systems. *Journal of Heat Transfer*, volume 134, number 031010.

Kitanovski, A. and Poredoš, A. (2002). Concentration distribution and viscosity of ice-slurry in heterogeneous flow. *International Journal of Refrigeration*, volume 25, number 6, p. 827–835.

Kitanovski, A., Poredoš, A., Reghem, P., Stutz, B., Dumas, J. P., Vuarnoz, D., Sari, O., Egolf, P. W. and Hansen, T. M. (2002). Flow patterns of ice-slurry flows. In Melinder, A., *Proceedings of the 5th IIR Workshop on Ice Slurries, Stockholm, Sweden*. p. 36–46.

Kitanovski, A., Vuarnoz, D., Ata-Caesar, D., Egolf, P. W., Hansen, T. M. and Doetsch, C. (2005). The fluid dynamics of ice slurry. *International Journal of Refrigeration*, volume 28, number 1, p. 37–50.

Krieger, I. M. and Dougherty, T. J. (1959). A Mechanism for Non-Newtonian Flow in Suspensions of Rigid Spheres. *Journal of Rheology*, volume 3, p. 137–152.

Kumano, H., Hirata, T., Shirakawa, M., Shouji, R. and Hagiwara, Y. (2010). Flow characteristics of ice slurry in narrow tubes. *International Journal of Refrigeration*, volume 33, number 8, p. 1513–1522.

Kumano, H., Tamura, F., Sawada, S. and Asaoka, T. (2013). Study on flow and heat transfer characteristics of ice slurry in the transition region. *International Journal of Refrigeration*, volume 36, number 3, p. 801–808.

Lee, D. W., Yoon, C. I., Yoon, E. S. and Joo, M. C. (2002). Experimental study of flow and pressure drop of ice slurry for various pipes. In *Proceedings of the 5th IIR Workshop on Ice Slurries, Stockholm, Sweden*. p. 22–29.

Lin, C. X. and Ebadian, M. A. (2008). A numerical study of developing slurry flow in the entrance region of a horizontal pipe. *Computers & Fluids*, volume 37, number 8, p. 965–974.

Lun, C. K. K., Savage, S. B., Jeffrey, D. J. and Chepurniy, N. (1984). Kinetic theories for granular flow: inelastic particles in Couette flow and slightly inelastic particles in a general flow field. *Journal of Fluid Mechanics*, volume 140, p. 223–256.

Manninen, M., Taivassalo, V. and Kallio, S. (1996). *On the mixture model for multiphase flow* (Technical report). Technical Research Center of Finland.

Matousek, V. (2002). Pressure drops and flow patterns in sand-mixture pipes. *Experimental Thermal and Fluid Science*, volume 26, number 6, p. 693–702.

Mellari, S. (2016). Experimental investigations of ice slurry flows in horizontal pipe based on monopropylene glycol. *International Journal of Refrigeration*, volume 65, p. 27–41.

Mellari, S., Boumaza, M. and Egolf, P. W. (2012). Physical modeling, numerical simulations and experimental investigations of Non-Newtonian ice slurry flows. *International Journal of Refrigeration*, volume 35, p. 1284–1291.

Menter, F. R. (1994). Two-Equation Eddy-Viscosity Turbulence Models for Engineering Applications. *AIAA Journal,*, volume 32, number 8, p. 1598–1605.

Metzner, A. B. and Reed, J. C. (1955). Flow of non-Newtonian fluids—correlation of the laminar, transition, and turbulent-flow regions. *AIChE Journal*, volume 1, number 4, p. 434–440.

Mika, L. (2012). Rheological behaviour of low fraction ice slurry in pipes and pressure loss in pipe sudden contractions and expansions. *International Journal of Refrigeration*, volume 35, number 6, p. 1697–1708.

Mika, L. (2013). Pressure loss coefficients of ice slurry in horizontally installed flow dividers. *Experimental Thermal and Fluid Science*, volume 45, p. 249–258.

Monteiro, A. C. S. and Bansal, P. K. (2010). Pressure drop characteristics and rheological modeling of ice slurry flow in pipes. *International Journal of Refrigeration*, volume 33, number 8, p. 1523–1532.

Morris, J. F. and Brady, J. F. (1998). Pressure-driven flow of a suspension: Buoyancy effects. *International Journal of Multiphase Flow*, volume 24, number 1, p. 105–130.

Niezgoda-Želasko, B. (2006). Heat transfer of ice slurry flows in tubes. *International Journal of Refrigeration*, volume 29, p. 437–450.

Niezgoda-Želasko, B. and Zalewski, W. (2006a). Momentum transfer of ice slurry flows in tubes, experimental investigations. *International Journal of Refrigeration*, volume 29, number 3, p. 418–428.

Niezgoda-Želasko, B. and Zalewski, W. (2006b). Momentum transfer of ice slurry flows in tubes, modeling. *International Journal of Refrigeration*, volume 29, number 3, p. 429–436.

Niezgoda-Želasko, B. and Želasko, J. (2014). Flow resistance of ice slurry in bends and elbow pipes. In *Journal of Physics: Conference Series*, volume 530. p. 012054.

Nott, P. R. and Brady, J. F. (1994). Pressure-driven flow of suspensions: Simulation and theory. *Journal of Fluid Mechanics*, volume 275, p. 157–199.

Nørgaard, E., Sørensen, T. A., Hansen, T. M. and Kauffeld, M. (2005). Performance of components of ice slurry systems: pumps, plate heat exchangers, and fittings. *International Journal of Refrigeration*, volume 28, number 1, p. 83–91.

Onokoko, C. L. and Galanis, N. (2013). Stratification in Isothermal Ice-Slurry Pipe Flow. In *Proceedings of the ASME IMECE 2013, San Diego, USA*.

Onokoko, C. L., Poirier, M., Galanis, N. and Poncet, S. (2017). Rheology of a propylene-glycol ice slurry. In *Proceedings of the 26th CANCAM, Victoria, Canada.*

Onokoko, C. L., Poirier, M., Galanis, N. and Poncet, S. (2018). Experimental and numerical investigation of isothermal ice slurry flow. *International Journal of Thermal Sciences*, volume 126, p. 82–95.

Phillips, R. J., Armstrong, R. C., Brown, R. A., Graham, A. L. and Abbott, J. R. (1992). A constitutive equation for concentrated suspensions that accounts for shear-induced particle migration. *Physics of Fluids A*, volume 4, number 1, p. 30–40.

Pope, S. B. (1994). Lagrangian PDF Methods for Turbulent Flows. *Annual Review of Fluid Mechanics*, volume 26, number 1, p. 23–63.

Pope, S. B. (2000). *Turbulent Flows*. Cambridge University Press.

Rabinowitsch, B. (1929). Über die Viskosität und Elastizität von Solen. *Zeitschrift für Physikalische Chemie*, volume 145A, p. 1–26.

Rached, W., Sicard, F., Lafargue, A. and Thorel, D. (2007). Ice slurry: Pressure drop and deposition velocity. *International Journal of Refrigeration*, volume 30, number 8, p. 1393–1400.

Reghem, P. (2002). *Étude hydrodynamique de fluides diphasiques solide-liquide en conduite circulaire : application au coulis de glace*. Ph.D. thesis, Université de Pau et des Pays de l'Adour, Pau, France.

Renaud-Boivin, S., Poirier, M. and Galanis, N. (2012). Experimental study of hydraulic and thermal behavior of an ice slurry in a shell and tube heat exchanger. *Experimental Thermal and Fluid Science*, volume 37, p. 130–141.

Revay, J. M. and Higdon, J. J. L. (1992). Numerical simulation of polydisperse sedimentation: equal-size spheres. *Journal of Fluid Mechanics*, volume 243, p. 15–32.

Richardson, J. F. and Zaki, W. N. (1954). Sedimentation and fluidization: Part 1. *Transactions of the Institute of Chemical Engineers*, volume 32, p. 35–53.

Schiller, L. and Nauman, Z. (1935). A Drag Coefficient Correlation. *VDI Zeitung*, volume 77, p. 318–320.

Shauly, A., Wachs, A. and Nir, A. (2000). Shear-induced particle resuspension in settling polydisperse concentrated suspension. *International Journal of Multiphase Flow*, volume 26, number 1, p. 1–15.

Snoek, C. W. (1993). *The design and operation of ice-slurry based district cooling systems* (Technical report). International Energy Agency, IEA District Heating.

Stamatiou, E. and Kawaji, M. (2005). Thermal and flow behavior of ice slurries in a vertical rectangular channel. Part I: Local distribution measurements in adiabatic flow. *International Journal of Heat and Mass Transfer*, volume 48, number 17, pp. 3527 – 3543.

Stokes, J. R., Telford, J. H. and Williamson, A.-M. (2005). The flowability of ice suspensions. *Journal of Rheology*, volume 49, number 1, p. 139–148.

Stutz, B. and Reghem, P. (2001). Friction losses of two-phase flow liquid-solid. In Boyman, T., Frei, B. and Egolf, P. W., *Proceedings of the 3rd IIR Workshop on Ice Slurries, Luzern, Switzerland*. p. 45–52.

Stutz, B., Reghem, P. and Martinez, O. (2001). Flow of slurries of particles with density close to that of water. In *Proceedings of the ICMF Congress, New Orleans, USA*. p. 1–12.

Swamee, P. K. and Aggarwal, N. (2011). Explicit equations for laminar flow of Bingham plastic fluids. *Journal of Petroleum Science and Engineering*, volume 76, number 3, p. 178–184.

Syamlal, M. and O'Brien, T. (1989). Computer simulation of bubbles in a fluidized bed. In *AIChE Symposium Series*, volume 85. p. 22–31.

Takahashi, H., Masuyama, T. and Kawashima, T. (1991). Flow properties for slurries of particles with density close to that of water. In *Proceedings of the ASME Fluids Engineering Division, Portland, USA*, volume 118.

Thomas, D. G. (1965). Transport characteristics of suspension: VIII. A note on the viscosity of Newtonian suspensions of uniform spherical particles. *Journal of Colloid Science*, volume 20, number 3, p. 267–277.

Tian, Q., He, G., Wang, H. and Cai, D. (2014). Simulation on transportation safety of ice slurry in ice cooling system of buildings. *Energy and Buildings*, volume 72, p. 262–270.

Trabelsi, S., Hafid, M., Poncet, S., Poirier, M. and Lacroix, M. (2017). Rheology of Ethylene- and Propylene-Glycol Ice Slurries: experiments and ANN model. *International Journal of Refrigeration*, volume 82, p. 447–460.

Turian, R. M., Hsu, F.-L. and Ma, T.-W. (1987). Estimation of the critical velocity in pipeline flow of slurries. *Powder Technology*, volume 51, number 1, p. 35–47.

Turian, R. M. and Yuan, T.-F. (1977). Flow of slurries in pipelines. *AIChE Journal*, volume 23, number 3, p. 232–243.

Turian, R. M., Yuan, T.-F. and Mauri, G. (1971). Pressure drop correlation for pipeline flow of solid-liquid suspensions. *AIChE Journal*, volume 17, number 4, p. 809–817.

Vuarnoz, D., Sari, O., Egolf, P. W. and Liardon, H. (2002). Ultrasonic velocity profiler UVP-XW for ice-slurry flow characterisation. In *Proceedings of the 3rd International Symposium on Ultrasonic Doppler Methods for Fluid Mechanics and Fluid Engineering, Lausanne, Switzerland.*

Wang, J., Wang, S., Zhang, T. and Battaglia, F. (2017). Mathematical and experimental investigation on pressure drop of heterogeneous ice slurry flow in horizontal pipes. *International Journal of Heat and Mass Transfer*, volume 108, p. 2381–2392.

Wang, J., Wang, S., Zhang, T. and Liang, Y. (2013a). Numerical investigation of ice slurry isothermal flow in various pipes. *International Journal of Refrigeration*, volume 36, number 1, p. 70–80.

Wang, J., Zhang, T. and Wang, S. (2013b). Heterogeneous ice slurry flow and concentration distribution in horizontal pipes. *International Journal of Heat and Fluid Flow*, volume 44, p. 425–434.

Wasp, E., Kenny, J. and Gandhi, R. (1977). Solid–liquid flow: slurry pipeline transportation. [pumps, valves, mechanical equipment, economics]. *Ser. Bulk Mater. Handl.; (United States)*, volume 1:4.

Xu, D., Liu, Z., Cai, L., Tang, Y., Yu, Y. and Xu, A. (2018). A CFD-PBM approach for modeling ice slurry flow in horizontal pipes. *Chemical Engineering Science*, volume 176, p. 546–559.

Zagarola, M. V. and Smits, A. J. (1998). A new mean velocity scaling for turbulent boundary layers. In *Proceedings of FEDSM98 ASME Fluids Engineering Division Summer Meeting, Washington DC, USA*.

Zhang, K. and Acrivos, A. (1994). Viscous resuspension in fully developed laminar pipe flows. *International Journal of Multiphase Flow*, volume 20, number 3, p. 579–591.

Zhang, P. and Ma, Z. W. (2012). An overview of fundamental studies and applications of phase change material slurries to secondary loop refrigeration and air conditioning systems. *Renewable and Sustainable Energy Reviews*, volume 16, number 7, pp. 5021 – 5058.

Zhang, P. and Shi, X. J. (2015). Thermo-fluidic characteristics of ice slurry in horizontal circular pipes. *International Journal of Heat and Mass Transfer*, volume 89, p. 950–963.

Zhiyao, S., Tingting, W., Fumin, X. and Ruijie, L. (2008). A simple formula for predicting settling velocity of sediment particles. *Water Science and Engineering*, volume 1, number 1, p. 37–43.